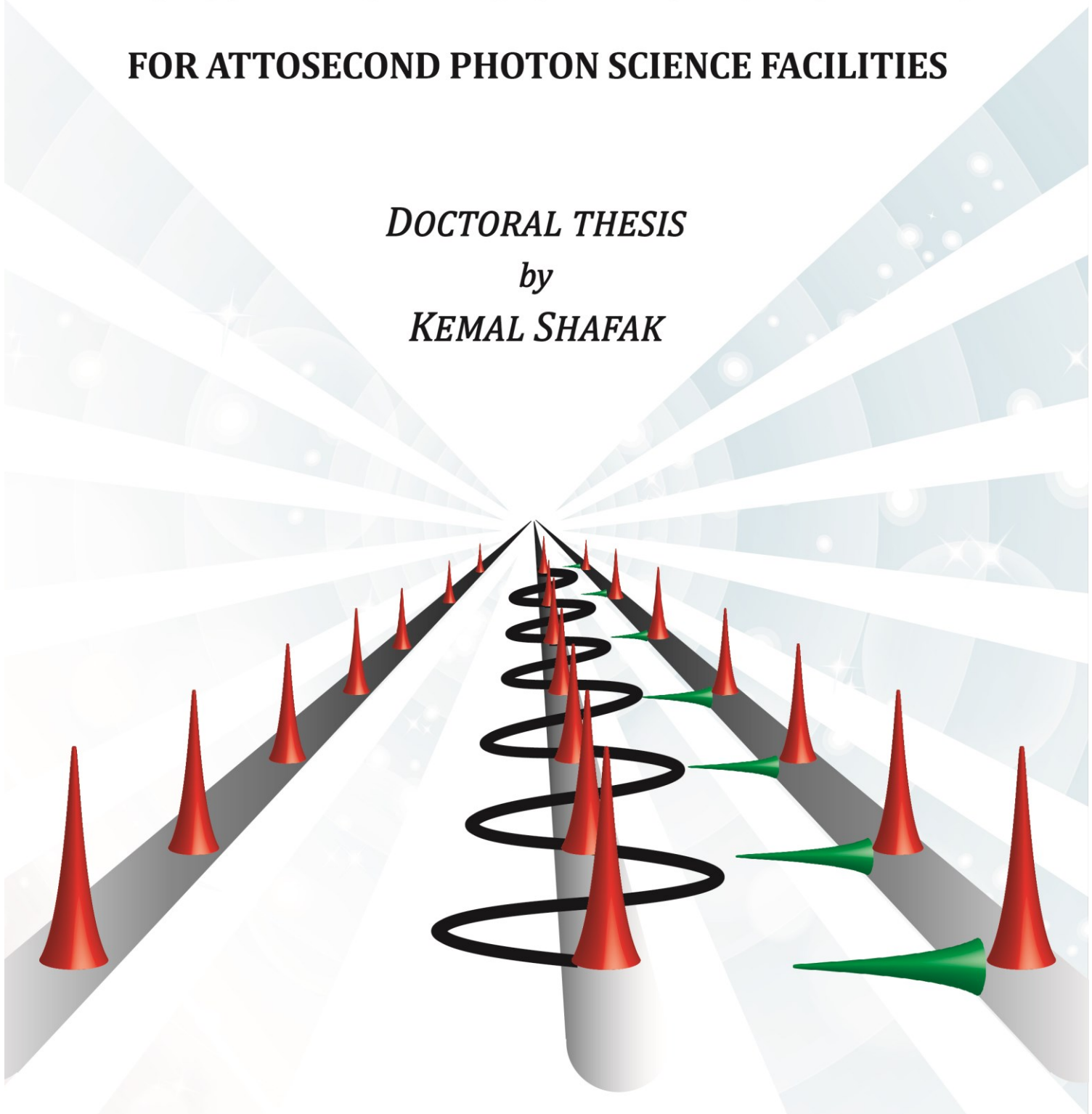


# LARGE-SCALE LASER-MICROWAVE SYNCHRONIZATION FOR ATTOSECOND PHOTON SCIENCE FACILITIES

*DOCTORAL THESIS*  
by  
*KEMAL SHAFAK*



**Hamburg, 2017**



---

---

**LARGE-SCALE LASER-MICROWAVE SYNCHRONIZATION**

**FOR ATTOSECOND PHOTON SCIENCE FACILITIES**

---

---

***DISSERTATION***

*zur Erlangung des Doktorgrades*

*an der Fakultät für Mathematik, Informatik und Naturwissenschaften*

*Fachbereich Physik*

*der Universität Hamburg*

vorgelegt von

***KEMAL SHAFAK***

*B.S. in Physics, Middle East Technical University, 2009*

*M.S. in Photonics, Friedrich-Schiller-Universität Jena, 2012*

Hamburg, March 2017

Gutachter der Dissertation	Prof. Dr. Franz Kärtner Dr. Holger Schlarb
Mitglieder der Prüfungskommission	Prof. Dr. Franz Kärtner Dr. Holger Schlarb Prof. Dr. Henry Chapman Prof. Dr. Ludwig Mathey Dr. Guoqing Chang
Vorsitzender des Promotionsausschusses	Prof. Dr. Ludwig Mathey
Datum der Disputation	22.03.2017

## **STATEMENT OF ORIGINAL AUTHORSHIP**

*I hereby declare that this dissertation has been written solely by myself except where due reference is made. Any help that I have received in my research work and the preparation of the thesis itself has been acknowledged.*

Kemal Shafak  
Hamburg, March 2017



# ABSTRACT

Low-noise transfer of time and frequency standards over large distances provides high temporal resolution for ambitious scientific explorations such as sensitive imaging of astronomical objects using multi-telescope arrays, comparison of distant optical clocks or gravitational-wave detection using large laser interferometers. In particular, rapidly expanding photon science facilities such as X-ray free-electron lasers (FELs) and attoscience centers have the most challenging synchronization requirements of sub-fs timing precision to generate ultrashort X-ray pulses for the benefit of creating super-microscopes with sub-atomic spatiotemporal resolution. The critical task in these facilities is to synchronize various pulsed lasers and microwave sources across multi-kilometer distances as required for seeded FELs and attosecond pump-probe experiments. So far, there has been no timing distribution system meeting this strict requirement. Therefore, insufficient temporal precision provided by the current synchronization systems hinders the development of attosecond hard X-ray photon science facilities.

The aim of this thesis is to devise a timing distribution system satisfying the most challenging synchronization requirements in science mandated by the next-generation photon science facilities. Using the pulsed-optical timing distribution approach, attosecond timing precision is realized by thoroughly investigating and eliminating the remaining noise sources in the synchronization system. First, optical and microwave timing detection schemes are further developed to support long-term stable, attosecond-precision measurements. Second, the feasibility of the master laser to support a kilometer-scale timing network with attosecond precision is examined by experimentally characterizing its free-running timing jitter and improving its long-term frequency stability with a sophisticated environmental insulation. Third, nonlinear pulse propagation inside optical fibers is studied both experimentally and numerically. The outcomes of the experimental and numerical analysis provide fundamental guidelines to minimize high- and low-frequency noise sources in the system. With these key developments in the link stabilization, a 4.7-km fiber link network is realized with a total timing jitter of 580 as RMS measured from 1  $\mu$ s to 52 h. Efficient synchronization of slave mode-locked lasers and slave microwave oscillators to the fiber link network is realized and further optimized with the help of a comprehensive feedback loop analysis. Ultimately, a complete laser-microwave network incorporating two mode-locked lasers and one microwave source is demonstrated with total 950-as timing jitter integrated from 1  $\mu$ s to 18 h. This work paves the way to unfold the full potential of next-generation attosecond photon science facilities, thereby to revolutionize many research fields from structural biology to material science and from chemistry to fundamental physics.

## ZUSAMMENFASSUNG

Die rauscharme Übertragung von Zeit- und Frequenzstandards über große Distanzen hinweg ermöglicht eine hohe zeitliche Auflösung für anspruchsvolle wissenschaftliche Untersuchungen. Zu diesen zählen beispielsweise die empfindliche Bildgebung von astronomischen Objekten mit Multi-Teleskop-Arrays, der Vergleich von entfernten optischen Uhren oder die Detektion von Gravitationswellen mit Hilfe von großen Laser-Interferometern. Insbesondere die sich technologisch schnell entwickelnden Photon-Forschungseinrichtungen, wie Röntgen-Freie-Elektronen-Laser und Forschungszentren für die Attosekundenwissenschaft, haben herausfordernde Synchronisationsanforderungen. Eine zeitliche Präzision unterhalb einer Femtosekunde wird benötigt, um Super-Mikroskope von ultrakurzen Röntgenpulsen mit subatomarer Raum-Zeit-Auflösung zu realisieren. Die kritische Aufgabe ist die Synchronisierung von verschiedenen gepulsten Lasern und Mikrowellenquellen über Kilometer entfernte Distanzen, wie dies für seeded FELs und Attosekunden-Pump-Probe-Experimente erforderlich ist. Bisher gibt es kein Zeitverteilungssystem, das diese strengen Anforderungen erfüllen kann. Die derzeit ungenügende zeitliche Präzision der Synchronisationssysteme stellt ein großes Hindernis für die Forschung mit kohärenten Attosekunden-Pulsen im harten Röntgen-Spektralbereich dar.

Das Ziel dieser Arbeit ist die Entwicklung eines Zeitverteilungssystems, das die anspruchsvollsten Synchronisationsanforderungen in der Wissenschaft für die nächste Generation der Photon-Forschungseinrichtungen erfüllen kann. Mit einer Zeitverteilungsmethode, die auf Lichtpulsen beruht, wird eine Attosekunden-Zeitgenauigkeit realisiert. Dies wird durch die gründliche Untersuchung der Rauschquellen im System und der gezielten Rauschunterdrückung ermöglicht. Zuerst werden optische und Mikrowellen-Zeiterfassungstechniken weiterentwickelt, um eine langfristige Attosekundenpräzision zu ermöglichen. Weiterhin wird der Master-Laseroszillator hinsichtlich seiner Eignung für ein kilometerlanges Zeitverteilungsnetzwerk mit Attosekundenpräzision durch Charakterisierung seines inhärenten Jitter untersucht. Seine langfristige Frequenzstabilität wird mit einer elaborierten Isolierung gegenüber Umgebungseinflüssen verbessert und getestet. Dann wird die nichtlineare Pulsausbreitung in den Glasfasern sowohl experimentell als auch numerisch untersucht. Die Ergebnisse der experimentellen und numerischen Analyse liefern grundlegende Erkenntnisse zur Minimierung der Hoch- und Niederfrequenz-Rauschquellen im System. Basierend auf diesen wichtigen Entwicklungen in der Glasfaser-Link-Stabilisierung wird ein 4,7-km langes Faser-Link-Netzwerk realisiert, bei dem über einen Zeitraum von 1  $\mu$ s bis 52 h ein gesamter Jitter von 580 as RMS gemessen wird. Die effiziente Synchronisation der gepulsten Slave-Laser und Slave-Mikrowellen-Oszillatoren auf ein Glasfaser-Netzwerk wird zuerst realisiert und dann mit Hilfe einer umfassenden Analyse der Feedback-Schleife weiter optimiert. Letztlich wird ein komplettes Laser-Mikrowellen-Netzwerk demonstriert, das zwei modengekoppelte Laser und eine Mikrowellenquelle enthält. Insgesamt wird für dieses Netzwerk nur 950-as Jitter von 1  $\mu$ s bis 18 h gemessen. Diese Arbeit eröffnet damit die Möglichkeit, das volle Potenzial der nächsten Generation der Attosekunden-Photon-Forschungseinrichtungen auszuschöpfen und somit zahlreiche Forschungsgebiete von der Strukturbiologie bis zu den Materialwissenschaften und von der Chemie bis zur Grundlagenphysik zu revolutionieren.

## ACKNOWLEDGMENTS

It was a fortunate day for me when I saw the PhD position posted by Prof. Kärtner by chance on the IMPRS website. After the first interview with him, I already felt that I was going to work in a cutting-edge scientific project with an inspiring and caring supervisor. Now, four years of PhD experience have proven my initial feelings completely correct and I can honestly say that I have never met anyone who can provide so good accessibility and constant support within such a busy schedule. Therefore, I would like to sincerely thank Prof. Kärtner for the opportunity to be a member of his team and to develop my thesis under his supervision.

I wish to express my gratitude to Dr. Ming Xin for his committed first-hand supervision and guidance of this work. It has been a privilege for me to have such an esteemed mentor and colleague, who has a keen eye for detail, a curious mind for knowledge and unlimited patience for experimentation. I have felt the perfect synergy while working with him and always enjoyed our countless days spent in the lab and our long discussions about science, football and history. Therefore, I wholeheartedly thank him for his contributions to every single section of this thesis.

I would also like to thank my co-advisor Dr. Holger Schlarb for sharing his wisdom and resources in the field, overseeing the development of my thesis and strengthening the collaboration between our research groups.

Over the duration of my thesis, I had the pleasure to work with many research collaborators from all around the world. Together with Michael Y. Peng and Patrick T. Callahan from MIT, we have spent a very fruitful and joyful summer in 2013, where we laid down the foundations of our timing system. Thank you very much guys. In addition, I would like to acknowledge the contributions of the former and current members of the timing team in CFEL: Wenting Wang, Dr. Oliver D. Mücke, Aram Kalaydzhyan, Dr. Qing Zhang, Dr. Shih-Hsuan Chia and Stefano Valente. Without them, the timing project would not have been so successful. I also wish to thank the rest of the CFEL crew for providing a great working environment. Especially our group secretary Christine Berber and my dear colleague and friend Dr. Hüseyin Çankaya have eased my adaptation to Hamburg and always provided their help in numerous matters.

Financial support is essential for successful research. I am grateful to the Federal Government of Germany for their generous initiatives to attract international students which allowed me to pursue my graduate studies in Germany. Furthermore, I would like to acknowledge the research funding provided by Deutsches Elektronen-Synchrotron and the Hamburg Centre for Ultrafast Imaging of Deutsche Forschungsgemeinschaft which made this work possible.

I also owe a big thank you to the IMPRS-UFAST graduate school, its coordinators and fellow graduate students for the excellent selection of interesting training opportunities and invaluable exchange of knowledge and experience.

I am thankful to all my friends that I have made in my life in many different countries for being there for me. Especially thank you Rossa, Beko, Lisa, Alex, Mikheil, Emmi, Halil (x2), and Hayri for making my life very colorful, for your protection and support. I would also like to thank my parents, my grandparents and my sister for always believing in me and giving me the support to explore the weird and interesting world of physics. Finally, the last gratitude goes to my beautiful wife Polina. You are the very source of my courage and strength to take new challenges in life. I would not have made this far without your inspiration and unconditional support. Çok teşekkür ederim! Большое спасибо!

# PUBLICATION LIST

## PUBLICATIONS IN REFEREED JOURNALS

1. **K. Şafak**, M. Xin, M. Y. Peng and F. X. Kärtner, "Synchronous mode-locked laser network with 20<sup>th</sup> decimal timing precision," manuscript in preparation.
2. M. Xin, **K. Şafak**, M. Y. Peng, A. Kalaydzhyan, W. Wang, O. D. Mücke and F. X. Kärtner, "Attosecond precision multi-kilometer laser-microwave network," *Nature: Light Science Applications*, vol. 6, no. e16187, 2017.
3. M. Xin, **K. Şafak**, M. Y. Peng, A. Kalaydzhyan, P. T. Callahan, W. Wang, O. D. Mücke and F. X. Kärtner, "Breaking the femtosecond barrier in multi-kilometer timing synchronization systems," *IEEE Journal of Selected Topics in Quantum Electronics*, vol. 23, no. 3, 2017.
4. **K. Şafak**, M. Xin, Q. Zhang, S.-H. Chia, O. D. Mücke and F. X. Kärtner, "Jitter analysis of timing-distribution and remote-laser synchronization systems," *Optics Express*, vol. 24, no. 19, pp 21752-21765, 2016.
5. **K. Şafak**, M. Xin, P. T. Callahan, M. Y. Peng, and F. X. Kärtner, "All fiber-coupled, long-term stable timing distribution for free-electron lasers with few-femtosecond jitter," *Structural Dynamics*, vol. 2, no.4, 041715, 2015.
6. M. Xin, **K. Şafak**, M. Y. Peng, P. T. Callahan and F. X. Kärtner, "One-femtosecond, long-term stable remote laser synchronization over a 3.5-km fiber link," *Optics Express*, vol. 22, no. 12, pp. 14904-14912, 2014.
7. P. T. Callahan, **K. Şafak**, P. Battle, T. D. Roberts and F. X. Kärtner, "Fiber-coupled balanced optical cross-correlator using PPKTP waveguides," *Optics Express*, vol. 22, no. 8, pp. 9749-9758, 2014.

## PROCEEDINGS OF REFEREED CONFERENCES

1. **K. Şafak**, M. Xin, M. Y. Peng, A. Kalaydzhyan, W. Wang, O. D. Mücke and F. X. Kärtner, "Synchronous laser-microwave network for attosecond-resolution photon science," *Proceedings of IBIC 2016*, paper TUBL03, 2016.
2. A. Kalaydzhyan, M. Y. Peng, M. Xin, **K. Şafak**, W. Wang, F. X. Kärtner, "Ultrahigh precision synchronization of optical and microwave frequency sources," *J. Phys. Conf. Ser.*, vol. 741, no. 1, 2016.
3. M. Xin, **K. Şafak**, M. Y. Peng, A. Kalaydzhyan, W. Wang, O. D. Mücke and F. X. Kärtner, "Attosecond precision multi-km laser-microwave network," *Technical Digest of CLEO 2016*, paper JTh4C.6, 2016.
4. **K. Şafak**, M. Xin, M. Y. Peng, and F. X. Kärtner, "Synchronous mode-locked laser network with sub-fs jitter and multi-km distance," *Technical Digest of CLEO 2016*, paper SM4H.2, 2016.
5. W. Wang, A. Kalaydzhyan, **K. Şafak**, M. Xin, M. Y. Peng, K. Jung, J. Kim and F. X. Kärtner, "High precision synchronization of a large-scale microwave network over stabilized fiber links," *Technical Digest of CLEO 2016*, paper SM4H.5, 2016.

6. S.-H. Chia, L.-J. Chen, **K. Şafak**, O. D. Mücke, and F. X. Kärtner "Transient spatiotemporal optimization of octave-spanning Ti:sapphire oscillators," *Technical Digest of CLEO 2016*, paper SM1I.7, 2016.
7. **K. Şafak**, M. Xin, M. Y. Peng, and F. X. Kärtner, "Synchronous mode-locked laser network with sub-fs drift and multi-km distance," *Proceedings EFTF 2016*, 2016.
8. A. Kalaydzhyan, M. Y. Peng, M. Xin, **K. Şafak**, W. Wang and F. X. Kärtner, "Optical to microwave synchronization with sub-femtosecond daily drift," *Proceedings EFTF2016*, 2016.
9. M. Xin, **K. Şafak**, P. T. Callahan, M. Y. Peng, and F. X. Kärtner, "All-fiber approach to long-term stable timing distribution system," *Proceedings of FEL2015*, 2015.
10. **K. Şafak**, M. Xin, M. Y. Peng, and F. X. Kärtner, "Ultra-low jitter timing transfer over a multi-km fiber network with  $10^{-21}$  relative stability," *Technical Digest of CLEO 2015*, paper STh3N.1, 2015.
11. M. Xin, **K. Şafak**, M. Y. Peng, P. T. Callahan, and F. X. Kärtner, "Long-term stable remote laser synchronization over a 3.5-km fiber link with one-femtosecond residual timing jitter," *Proceedings of URSI GASS 2014*, 2014.
12. M. Xin, **K. Şafak**, M. Y. Peng, P. T. Callahan, and F. X. Kärtner, "One-femtosecond, long-term stable remote laser synchronization over a 3.5-km fiber link," *Technical Digest of CLEO 2014*, paper SW30-4, 2014.
13. **K. Şafak**, M. Xin, M. Y. Peng, P. T. Callahan, and F. X. Kärtner, "Laser-to-laser remote transfer and synchronization with sub-fs precision over a 3.5 km fiber link," *Proceedings IFCS 2014*, 2014.
14. M. Y. Peng, P. T. Callahan, A. H. Nejadmalayeri, S. Valente, **K. Ahmed**, M. Xin, E. Monberg, M. Yan, L. Grüner-Nielsen, J. M. Fini, T. D. Roberts, P. Battle, and F. X. Kärtner, "Long-term stable, large-scale, optical timing distribution systems with sub-femtosecond timing stability," *Proceedings FEL 2013*, 2013.
15. M. Y. Peng, P. T. Callahan, A. H. Nejadmalayeri, S. Valente, **K. Ahmed**, M. Xin, E. Monberg, M. Yan, L. Grüner-Nielsen, J. M. Fini, T. D. Roberts, P. Battle, and F. X. Kärtner, "Towards a large-scale, optical timing distribution system with sub-femtosecond residual timing jitter," *Proceedings of EFTF-IFCS 2013*, 2013.
16. M. Xin, **K. Ahmed**, and F. X. Kärtner, "Ultralow jitter mode-locked lasers at 1.5 micron for a subfemtosecond long-term stable timing distribution system," *Technical Digest of CLEO Europe 2014*, paper CFIE\_5\_3, 2013.

## AWARDS

1. **Best Student Paper Competition Winner** in European Time and Frequency Forum 2016, received for the conference paper and presentation "Synchronous mode-locked laser network with sub-fs drift and multi-km distance".
2. **Student Paper Competition Award** in IEEE International Frequency Control Symposium 2014, received for the conference paper and presentation "Laser-to-laser remote transfer and synchronization with sub-fs precision over a 3.5 km fiber link".

# CONTENTS

<b>Abstract</b> .....	<b>i</b>
<b>Zusammenfassung</b> .....	<b>ii</b>
<b>Acknowledgments</b> .....	<b>iii</b>
<b>Publication list</b> .....	<b>iv</b>
<b>Contents</b> .....	<b>vi</b>
<b>List of figures</b> .....	<b>1</b>
<b>List of tables</b> .....	<b>4</b>
<b>List of abbreviations</b> .....	<b>5</b>
<b>Foreword</b> .....	<b>7</b>
<b>1 Introduction</b> .....	<b>9</b>
1.1 Background .....	9
1.2 X-ray FELs .....	12
1.3 Laser-based attoscience centers .....	15
1.4 Scope of the dissertation .....	16
<b>2 Timing detectors</b> .....	<b>19</b>
2.1 Microwave phase detector .....	19
2.2 Balanced optical cross-correlator .....	21
2.2.1 <i>Type-II second-harmonic BOC</i> .....	23
2.2.2 <i>Fiber-coupled BOC using PPKTP waveguides</i> .....	25
2.2.3 <i>BOC timing sensitivity characterization</i> .....	28
2.3 Balanced optical-microwave phase detector .....	29
2.3.1 <i>Free-space-coupled BOMPD</i> .....	32
2.3.2 <i>BOMPD phase sensitivity characterization</i> .....	34
<b>3 Master laser</b> .....	<b>35</b>
3.1 Timing jitter characterization .....	35
3.2 Long-term frequency and environmental stability .....	40
<b>4 Noise-free fiber link transmission</b> .....	<b>45</b>
4.1 General fiber link stabilization scheme .....	45

4.2	Experimental results: traditional feedback .....	46
4.2.1	<i>Fiber link stabilization with free-space BOCs.....</i>	46
4.2.2	<i>Fiber link stabilization with fiber-coupled BOCs .....</i>	51
4.2.3	<i>Timing transfer over a multi-km fiber link network.....</i>	55
4.3	Fiber link induced timing errors .....	58
4.3.1	<i>BOC response to temporal pulse profile distortions .....</i>	58
4.3.2	<i>Temporal COG shifts during nonlinear pulse propagation .....</i>	61
4.3.3	<i>Simulation results.....</i>	63
4.3.4	<i>Feedback loop analysis of timing link stabilization.....</i>	65
4.4	Attosecond precision fiber link network .....	68
4.4.1	<i>Key improvements in the fiber link stabilization .....</i>	68
4.4.2	<i>Experimental results: improved feedback.....</i>	70
<b>5</b>	<b>Laser and microwave synchronization .....</b>	<b>73</b>
5.1	Frequency synchronization of two oscillators .....	73
5.2	Remote laser synchronization.....	75
5.3	Jitter analysis of the timing distribution system .....	78
5.3.1	<i>Timing jitter characterization of the slave laser .....</i>	78
5.3.2	<i>Synchronization of the slave laser on a timing link network.....</i>	82
5.4	Synchronous mode-locked laser network.....	90
5.4.1	<i>Timing drift.....</i>	91
5.4.2	<i>Timing jitter spectral density.....</i>	93
5.5	Attosecond precision laser-microwave network .....	100
5.5.1	<i>Local laser-microwave synchronization .....</i>	100
5.5.2	<i>Synchronous laser-microwave network.....</i>	102
<b>6</b>	<b>Conclusion and outlook.....</b>	<b>107</b>
<b>A</b>	<b>Appendix .....</b>	<b>112</b>
A.1	Total transfer function and electronic noise jitter .....	112
A.2	Experimental parameters used in the calculations .....	114
	<b>Bibliography .....</b>	<b>117</b>

## LIST OF FIGURES

Figure 1.1: Typical optical spectrum of a mode-locked laser.....	9
Figure 1.2: Schematic of an externally seeded and optically synchronized X-ray FEL.....	12
Figure 1.3: Layout of major laser sources of ELI-ALPS facility in Hungary.....	15
Figure 1.4: Layout of a laser-microwave network with sub-fs daily jitter.....	16
Figure 2.1: Traditional approach to timing jitter measurement of optical pulse trains.....	19
Figure 2.2: Principle of timing detection using a BOC.....	21
Figure 2.3: BOC simulation results with an amplitude modulated input pulse.....	22
Figure 2.4: Sensitivity comparison between a BOC and a microwave phase detector.....	23
Figure 2.5: Type-II second-harmonic BOC for input pulses at 1550 nm.....	24
Figure 2.6: Improving polarization extinction ratio of type-II SH-BOC.....	25
Figure 2.7: Fiber-coupled BOC using PPKTP waveguides.....	26
Figure 2.8: Second-harmonic generation efficiency of the fiber-coupled BOC.....	26
Figure 2.9: Characterizing cross-correlation performance of the integrated BOCs.....	27
Figure 2.10: FC-BOC sensitivity as function of (a) temperature and (b) input power.....	28
Figure 2.11: Optical-to-microwave phase detection with balanced intensity detector.....	29
Figure 2.12: Operation principles of BOMPD and Sagnac-interferometer.....	31
Figure 2.13: Schematic of free-space-coupled BOMPD.....	32
Figure 3.1: Experimental setup for timing jitter characterization of the master laser.....	36
Figure 3.2: Feedback model for BOC-based laser synchronization.....	37
Figure 3.3: Feedback simulations for the SH-BOC timing jitter measurement.....	38
Figure 3.4: Experimental results of the SH-BOC timing jitter measurement.....	39
Figure 3.5: Phase noise comparison of the master laser with a microwave source.....	40
Figure 3.6: A setup for measuring the precision of a timing distribution system.....	41
Figure 3.7: Environmental insulation of the master laser and reference beam paths.....	43
Figure 3.8: Long-term repetition rate stability of the master laser.....	44
Figure 4.1: Operation principle of fiber link stabilization using BOCs.....	45
Figure 4.2: Schematic of the 3.5-km fiber link.....	47
Figure 4.3: Experimental setup for fiber link stabilization with free-space BOCs.....	48
Figure 4.4: Experimental results of the fiber link stabilization with free-space BOCs.....	50
Figure 4.5: Experimental setup for all-fiber-coupled timing link stabilization.....	52
Figure 4.6: Experimental results of all-fiber-coupled timing link stabilization.....	53
Figure 4.7: Experimental setup for fiber-link network stabilization.....	55

Figure 4.8: Experimental results of the fiber-link network stabilization.....	56
Figure 4.9: Setup elements causing the link power fluctuations.....	57
Figure 4.10: BOC response to temporal profile distortions of the input pulses.....	60
Figure 4.11: Timing drift introduced by link power fluctuations.....	64
Figure 4.12: Timing jitter induced by the fiber nonlinearities.....	64
Figure 4.13: Feedback model of timing link stabilization.....	66
Figure 4.14: Simulation results of the timing link feedback model.....	67
Figure 4.15: Improved experimental setup for fiber-link network stabilization.....	69
Figure 4.16: Long-term measurement results of the improved link-network.....	71
Figure 4.17: Timing jitter and relative timing instability of the link network.....	72
Figure 5.1: Operating principle of frequency synchronization using BOCs and BOMPDs.....	73
Figure 5.2: Effect of repetition rate mismatch between two pulse trains.....	74
Figure 5.3: Experimental setup for remote laser synchronization.....	76
Figure 5.4: Experimental results of the remote laser synchronization.....	77
Figure 5.5: Slave Ti:sa laser and its jitter characterization setup.....	79
Figure 5.6: Timing jitter characterization results of the Ti:sa laser.....	80
Figure 5.7: Simulation results of the Ti:sa laser jitter characterization.....	82
Figure 5.8: Setup for the synchronization of the Ti:sa laser on a timing link network.....	83
Figure 5.9: Experimental results of the remote Ti:sa laser synchronization.....	84
Figure 5.10: Feedback model for the remote Ti:sa laser synchronization.....	85
Figure 5.11: Calculated transfer coefficients for varied SF-BOC1 feedback gain.....	87
Figure 5.12: Measured environmental noise imposed on the fiber links.....	88
Figure 5.13: Noise sources of the remote Ti:sa laser synchronization.....	89
Figure 5.14: Experimental setup for the synchronous mode-locked laser network.....	90
Figure 5.15: Long-term stability measurements with traditional link stabilization.....	92
Figure 5.16: Improved long-term stability with the suppression of link nonlinearities.....	93
Figure 5.17: Short-term stability measurements of the laser network.....	94
Figure 5.18: Feedback model of the laser network.....	95
Figure 5.19: Estimated free-running timing jitter of the slave laser 2.....	97
Figure 5.20: Calculated jitter transfer coefficients of the laser network.....	97
Figure 5.21: Noise sources of the observed out-of-loop network jitter.....	99
Figure 5.22: Timing jitter spectrum of the laser network.....	99
Figure 5.23: Experimental setup for local laser-microwave synchronization.....	101
Figure 5.24: Experimental results of the local laser-microwave synchronization.....	101

Figure 5.25: Experimental setup for the synchronous laser-microwave network.....	102
Figure 5.26: Timing sensitivities and noise floors of the detectors. ....	104
Figure 5.27: Experimental results of the synchronous laser-microwave network. ....	105
Figure 6.1: Timing jitter within the locking bandwidth.....	110
Figure 6.2: Timing jitter above 1 kHz. ....	111
Figure A.1: Noise model of a PI controller.....	113

## LIST OF TABLES

Table A.1: Experimental parameters used for the feedback model in Figure 3.2. ....	114
Table A.2: Experimental parameters used for the feedback model in Figure 4.13. ....	114
Table A.3: Experimental parameters used for the calculations in Figure 5.7. ....	114
Table A.4: Experimental parameters used for the feedback model in Figure 5.10. ....	115
Table A.5: Experimental parameters used for the feedback model in Figure 5.18. ....	116

## LIST OF ABBREVIATIONS

ADEV	Allan deviation
ALPS	Attosecond light pulse source
AM-PM	Amplitude modulation to phase modulation
ASE	Amplified spontaneous emission
BAM	Beam arrival-time monitor
BBO	Beta barium borate
BOC	Balanced optical cross-correlator
BOMPD	Balanced optical-microwave phase detector
BPD	Balanced photodetector
COG	Center-of-gravity
cw	Continuous-wave
DAQ	Data acquisition card
DCM	Double-chirped mirror
ELI	Extreme light infrastructure
EDFA	Erbium-doped fiber amplifier
FC-BOC	Fiber-coupled balanced optical cross-correlator
FEL	Free-electron laser
FSC-BOMPD	Free-space-coupled balanced optical-microwave phase detector
FWHM	Full width at half maximum
HHG	High-harmonic generation
Linac	Linear accelerator
OPA	Optical parametric amplifier
PBS	Polarization beam splitter
PI	Proportional-integral
PLL	Phase-locked-loop
PM	Polarization-maintaining
PM-DCF	Polarization-maintaining dispersion compensating fiber
PNS-BOC	Polarization-noise-suppressed balanced optical cross-correlator
PPKTP	Periodically poled potassium titanyl phosphate
PZT	Piezoelectric transducer
RF	Radio frequency
RIN	Relative intensity noise

RMS	Root-mean-square
SASE	Self-amplified spontaneous emission
SF-BOC	Sum-frequency balanced optical cross-correlator
SGI	Sagnac-interferometer
SH-BOC	Second-harmonic balanced optical cross-correlator
SM	Single mode
SNR	Signal-to-noise ratio
SOD	Second-order dispersion
SPM	Self-phase modulation
Ti:sa	Titanium-sapphire
TD	Timing detector
TOD	Third-order dispersion
VCO	Voltage-controlled oscillator
WDM	Wavelength-division multiplexer
XFEL	X-ray free-electron laser

## FOREWORD

“Where did we come from?” and “what is the origin of the species that we see around us?” are two questions which have driven human curiosity immensely since thousands of years. Only a century ago, we have come up with a profound answer to these questions: *Evolution*, which is simply stating that the heritable traits of biological populations change over successive generations [1]. Evolution is now a scientifically proven fact and explains with great precision why the animals look the way they do, why we have five fingers instead of six, and even why we are so deeply curious in nature [2]. I have developed a recent curiosity about whether we can make use of evolutionary theories in non-biological species like computer algorithms, technological developments, science etc. Then I have listened to a TED talk given by global strategist Parag Khanna. He likes to think of our planet like a human body, which evolves faster than any biological species living in itself. When compared to its premature state in the Middle Ages with no geographical connectivity, now our planet has developed a skeleton made of the transportation system including roads, railways, airports and harbors that enable our mobility across the continents [3]. The pipelines and electricity grids constitute its vascular system powering the body, whereas the satellites, internet cables and cellular networks are the nervous system allowing us to communicate and share information instantly [3]. This revolution of global connectivity has enabled such a drastic increase in the mobility of people, goods, resources and knowledge that the structure of our world has evolved “*from the vertically integrated empires of the 19<sup>th</sup> century, through the horizontally interdependent nations of the 20<sup>th</sup> century, into a global network civilization in the 21<sup>st</sup> century*” [3].

As one of the primary driving forces behind our global network of civilization, science becomes increasingly collaborative and international. Scientists and researchers have the most geography-independent profession in the world. They have a clear and unbiased way of communicating with each other and they can achieve even greater scientific developments “*by standing on the shoulders of giants*”<sup>1</sup>. The very best examples of the global and collaborative science are the super-national research organizations such as CERN, the International Linear Collider Collaboration, the European X-ray Free Electron Laser, and the Extreme Light Infrastructure. All these organizations aim to solve the most difficult problems that we encounter on our way to understand the universe by combining all the necessary resources without knowing any political borders: scientists, engineers, knowledge, capital, infrastructure, etc. which would be otherwise impossible for one country to afford alone. As a graduate student working in such a global scientific environment, I feel proud of the humanity that it developed such a pristine and systematic way of building and organizing knowledge. Even though

---

<sup>1</sup>Bernard of Chartres, 12<sup>th</sup> century; in meaning: “*discovering truth by building on previous discoveries*”

my doctoral project of “large-scale laser-microwave synchronization for attosecond photon science facilities” is quite specific and only one of the countless problems that we face in science, I would be very content if it can make even a small contribution to the European X-ray Free-Electron Laser or any other similar facilities to achieve higher time resolution. I am sure that regardless the amount of knowledge that I created, it will remain and be open to other scientists to learn from it. From a broader point of view, I believe that by contributing to global and collaborative science, I also contribute to the connectivity of the nations, cultures and societies which would in turn enable our world to evolve as a more sustainable and peaceful planet.

# 1 INTRODUCTION

## 1.1 BACKGROUND

“Never measure anything but frequency!” was the advice of the laser pioneer Arthur Schawlow to his students and fellow colleagues [4]. Indeed, when you think about it a little bit, measuring frequency is merely counting the number of events happening during a certain time interval. If you can do it with an accurate measurement apparatus, the complete procedure is digital and immune to many noise sources. In fact, frequency is the physical quantity that can be measured with by far the greatest accuracy. Thanks to the matured electronics technology, the definition of time is based on the microwave frequency measurement of a cesium atomic clock since 1967 which defines one second as 9 192 631 770 periods of the microwave radiation emitted by a Cs-133 atom transitioning between two nuclear spin states [5]. Measurement of optical frequencies, on the other hand, is not so straightforward because there are no electronic detectors fast enough to count optical frequencies which oscillate approximately 100 000 times faster than microwaves. Hence, the first versions of optical frequency counters were consisting of highly complex and expensive frequency chains occupying entire buildings to traverse the entire electromagnetic spectrum in discrete steps from the microwave signal of an atomic clock to the one desired optical frequency [6,7].

Even in the early days of mode-locked lasers, scientists were aware of the comb-like characteristics of their optical spectrum with discrete, regularly spaced sharp lines. As depicted in Figure 1.1, each optical frequency  $f_{opt}$  in the laser spectrum can simply be represented by the sum of the carrier-envelop-offset frequency  $f_0$  and an integer multiple of the pulse repetition rate  $f_R$ :

$$f_{opt} = m f_R + f_0 \quad (1.1)$$

Since  $f_0$  and  $f_R$  are in the microwave domain, by tracking their fluctuations and locking them to a microwave frequency standard (e.g., an atomic clock), it is possible to use mode-locked lasers for

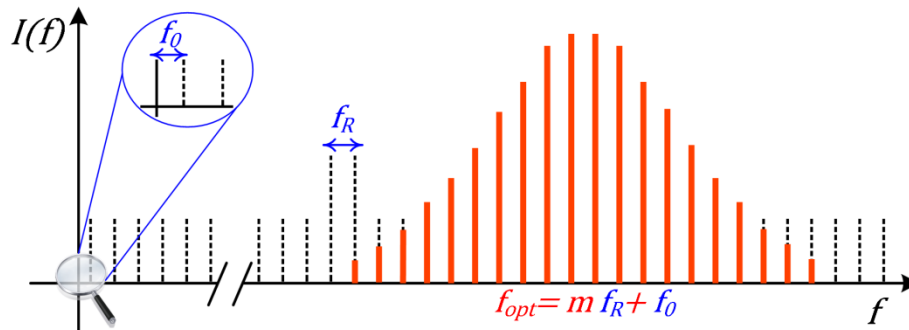


**Figure 1.1: Typical optical spectrum of a mode-locked laser.**

$f_{opt}$ : optical frequency;  $f_R$ : pulse repetition rate of the mode-locked laser;  $f_0$ : carrier-envelop-offset frequency;  $m$ : integer mode number;  $I(f)$ : optical power spectral density.

direct absolute measurements of optical frequencies. Detection and stabilization of the noise in  $f_R$  is relatively straightforward: photodetect the laser output, filter out one of the harmonics of the electronic spectrum and mix it with a microwave reference. Then the detected noise can be removed by controlling the laser cavity length through an intracavity mirror mounted on a piezoelectric transducer (PZT). The fluctuations in  $f_o$ , on the other hand, are harder to uncover, as they require high order nonlinear processes to compare the low frequency end of the spectrum with the high frequency end. The breakthrough in this field came with the ability to broaden the output optical spectrum of a mode-locked laser by preserving the phase coherence between the individual lines [8]. With a comb spanning more than an octave, one can frequency-double the red end of the spectrum ( $f_{opt,m} = m f_R + f_o$ ) with a nonlinear crystal so that the new lines will have twice the offset frequency ( $2f_{opt,m} = 2m f_R + 2f_o$ ). Then, the beat note of this signal with the blue end of the spectrum ( $f_{opt,2m} = 2m f_R + f_o$ ) will reveal  $f_o$  and its fluctuations (i.e., f-to-2f self-referencing [9,10]). Once this frequency is also measured and stabilized (e.g., by pump power modulation), a mode-locked laser can serve as a direct link between optical frequencies and radio frequencies (RF). This was the idea behind the optical frequency combs [11,12] which shrank bulky and complex frequency chains into a tabletop laser apparatus connecting the optical domain with the RF domain in a single step.

An optical frequency comb can be used as a bi-directional frequency-ruler. Besides measuring unknown optical frequencies with respect to microwave frequency standards, one can provide a microwave clock output from an ultrastable optical frequency. In this way, new atomic clocks referenced to hyperfine optical transitions [13] have been invented which have pushed the frequency measurement instabilities down to the 18<sup>th</sup> decimal place [14]. Today, researchers are able to compare independent optical clocks located in different countries with a statistical uncertainty of  $1 \times 10^{-15}/(\tau/s)^{1/2}$  ( $\tau$ : integration time) [15]. The capability of international optical clock comparison leads the way for a redefinition of the standard unit of time and opens doors to new horizons in fundamental science such as testing of Einstein's equivalence principle [16], chronometric geodesy [17], quantum networks [18] etc. Furthermore, alternative optical frequency standards based on cavity stabilized continuous-wave (cw) lasers also have an extraordinary performance demonstrating fractional frequency instabilities as low as  $1 \times 10^{-16}$  at 1 s [19]. An optical frequency comb can transfer this stability to the RF domain and extract extremely low noise microwaves due to its high optical-to-microwave division without the need for cryogenic temperatures and atomic frequency standards [20].

In the applications mentioned above, the mode-locked laser derives its long-term stability (>0.1 ms) from external sources, whereas the short-term stability originates from the internal dynamics of the laser itself and hence it requires a careful investigation. Fortunately, time domain

measurements of the pulse trains generated by various types of mode-locked lasers show extremely low timing jitter below 0.1 fs root-mean-square (RMS) integrated up to the Nyquist frequency of the pulse repetition rate [21,22,23]. This is a direct evidence proving that a well-defined optical frequency comb with ultra-sharp lines owes its existence to the perfect temporal periodicity and amplitude stability of the pulse train generated by the mode-locked laser. Therefore, there is a growing interest in exploiting low-noise properties of mode-locked lasers in frequency and time transfer applications.

Besides the comparison of distant optical clocks, drift-free and long-distance transfer of time and frequency standards provides high-temporal resolution for large-scale, ambitious scientific explorations. To name a few: sensitive imaging of low temperature black bodies in the universe using radio telescope arrays [24], gravitational deflection measurements of radio waves using very-long-baseline interferometry [25] and gravitational-wave detection using large laser interferometers [26,27]. Among these, the radio telescope array “Atacama Large Millimeter Array” in Chile demands the tightest timing distribution with 40-fs precision [28], whereas current long-base line interferometers and gravitational-wave detectors require a timing uncertainty of 1 ps [25] and 1  $\mu$ s [29], respectively. Since conventional time and frequency transfer techniques [30,31,32,33,34] can deliver facility-wide timing resolution up to 10 fs, the above-mentioned facilities are greatly satisfied with the provided precision and extra-ordinary scientific discoveries have been made such as the first experimental observation of the gravitational-waves at the Laser Interferometer Gravitational-wave Observatory, LIGO [35].

Another long-standing scientific endeavor concerns the development of a super-resolution camera which can capture ultrafast dynamics of atoms, molecules and electrons. Due to the first observation of intramolecular charge transfer [36] and the recent discovery of ultrafast Auger processes altering the chemistry of the matter in attosecond timescale [37], achieving this goal requires a coherent, high intensity electro-magnetic radiation with attosecond pulse duration and sub-nanometer wavelength. Therefore, next-generation photon science facilities such as X-ray free-electron lasers (FELs) [38,39,40,41,42] and laser-based attoscience centers [43] are emerging worldwide with the goal of generating isolated attosecond X-ray pulses with unprecedented brightness. To achieve this, it is necessary to develop an attosecond-precision timing distribution system synchronizing various microwave and optical sub-sources across the km-scale facilities to deliver the timing stability required for seeded FEL operation and attosecond pump-probe measurements. Otherwise, 30-fs level timing jitter present in the current FELs (best precision measured in [44]) would smear out the dynamics of intramolecular charge transfer and cascaded Auger decays occurring on attosecond time scales. So far, there has been no timing distribution

system meeting this strict requirement. Although research in attosecond X-ray pulse generation in FELs has progressed rapidly in the past few years [45,46], sub-atomic-level measurements cannot be performed due to the lack of high-precision timing control. Hence, low temporal precision provided by the current timing distribution systems remains to be a major obstacle from realizing attosecond hard X-ray photon science facilities. The aim of this thesis is to devise a novel timing distribution system satisfying the most challenging synchronization requirements in science posed by the next-generation photon science facilities. The following two sections provide brief background information about X-ray FELs and attoscience centers together with their synchronization requirements.

## 1.2 X-RAY FELS

At present, FELs are the only facilities that can generate bright, coherent hard X-ray pulses with temporal durations below 100 fs and up to  $10^{13}$  photon per pulse [40,47,48]. Figure 1.2 shows the schematic of an externally seeded X-ray FEL together with the layout of its optical synchronization system. Radiation from an FEL has much in common with radiation from an optical laser. An optical laser, for example a laser diode, has three basic components: a gain medium (e.g., quantum well), an energy source (e.g., pump current) and an optical resonator (e.g., coated facets). In an FEL (follow Figure 1.2 from left to right), the gain medium is the “free” electrons, which are stripped in the form of a bunch from a cathode by a pulsed injector laser. Then the electron bunch is accelerated to relativistic energies by the linear accelerators (Linacs), which constitute the energy source. In between each acceleration section, the energy and momentum spread of the electron bunch due to space charge effects is minimized by the magnetic compressors which introduce different path lengths for different electron energies. Finally, the electron bunch reaches the undulator section: a long, periodic magnetic dipole array serving as the resonator cavity. While the bunch propagates through the undulator, the interaction with an electromagnetic field leads to the concentration of the electrons in slices shorter than the wavelength of the field (i.e., micro-bunching). The electrons

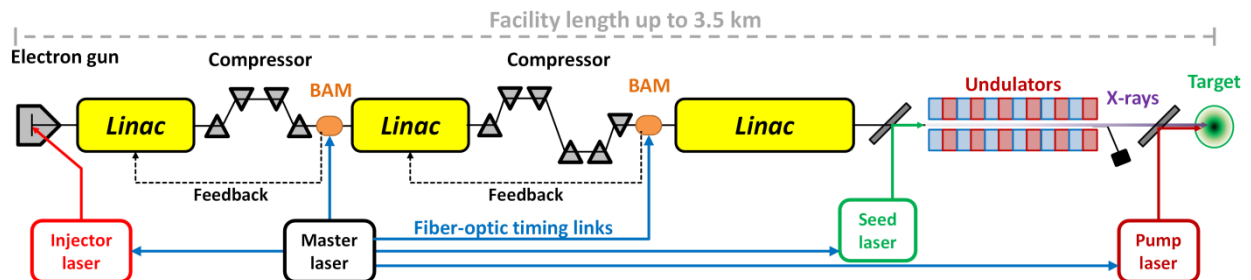


**Figure 1.2: Schematic of an externally seeded and optically synchronized X-ray FEL.**

Abbreviations: Linac: linear accelerator; BAM: beam arrival-time monitor.

in a micro-bunch radiate like a single particle of high charge (i.e., in phase) which enhances the micro-bunching even further and leads to an exponential growth of the radiation (i.e., lasing).

The initial radiation field triggering the micro-bunching can be either an internal field (i.e., the spontaneous emission of the undulator) or an external one (e.g., a seed laser). The first mode of FEL operation is called *self-amplified spontaneous emission* (SASE) [49,50], whereas the second one is called *seeding*. SASE FELs have the advantage that the resonance condition is automatically fulfilled as the radiation is created by the undulator (i.e., the resonator) itself and it is available at all wavelengths even in the hard X-ray regime. Since there are many longitudinal modes from an electron bunch can be amplified by the undulator, a major drawback of a SASE FEL is that the radiation undergoes strong pulse-to-pulse spectrum and temporal profile fluctuations due to the noisy startup process [51]. Hence, the length of the electron bunch limits the temporal duration of the X-ray pulses produced by SASE FELs. In the *seeding* technique, a well-defined external light field fulfilling the undulator resonance condition overlaps with the electron bunch. In this way, the spectral and temporal properties of the FEL pulse can be tailored and tuned by the injected seed pulse [39]. While there are seed sources available at wavelengths down to the deep ultraviolet based on high-harmonic generation (HHG) using optical laser pulses [52]; external seeding is not possible at X-ray wavelengths since the FELs themselves are the only coherent light sources in this spectral regime. However, in this case self-seeding an X-ray FEL offers a solution by feeding back a fixed spectral slice of the X-ray radiation as the seed source [53].

One of the most popular time-resolved experiments performed in FELs is the pump-probe arrangement. In this scheme, the molecular system under test is excited by a pump pulse (e.g., from an ultrafast optical laser) to trigger a certain reaction, and the excited state is probed by the FEL pulse to determine the system's response. By varying the temporal offset between the pulses, the temporal evolution of the excited system can be resolved on ultrafast timescales.

High precision timing distribution systems are critical for FELs for three main reasons:

1. Temporal duration of the X-ray pulses is determined by the final compression of the electron bunch which is highly sensitive to the overall synchronization between the injector laser, the Linacs, and the bunch compressors.
2. In the case of seeded FELs, timing jitter between the seed laser pulse and the electron bunch must be minimized since the bunch possesses the noise accumulated during the acceleration process.
3. Relative timing jitter between the FEL output and the pump laser must be controlled with a precision better than the FEL pulse duration for pump-probe experiments aiming high temporal resolution.

Next generation FELs such as Linac Coherent Light Source II in Stanford [41] and the European X-ray FEL (XFEL) in Hamburg [38] are expected to deliver X-ray pulses even shorter than 1 fs. The research on generating even shorter X-ray pulses from these facilities has been intensifying over the past few years [45,46]. Therefore, unlocking the high temporal-resolution capabilities of these facilities will require extremely stable timing distribution systems delivering attosecond precision between optical and RF sources located over kilometer distances.

There are two basic FEL synchronization schemes reported so far. The first scheme uses microwave signal distribution via amplitude modulation of a cw laser and employs electronic phase-locking techniques to synchronize various microwave and pulsed laser sources [31]. However, this technique fails to provide less than  $\sim 100$ -fs RMS jitter across the facility [54] due to low phase discrimination of microwave mixers and high noise floor at photodetection. The second scheme [30,44,55], which is further developed in this thesis, uses ultralow-noise pulses generated by a mode-locked laser (i.e., master laser) as its timing signal. As depicted in Figure 1.2, the timing signal of the master laser is transferred through fiber-optic timing links from a central location to multiple end stations whose transmission delays are stabilized by balanced optical cross-correlators (BOC) [56,57]. At the end stations, the outputs of the timing links are used for three main applications. First, the arrival time of the electron bunches with respect to the master laser is measured using beam arrival-time monitors (BAMs in Figure 1.2) [58]. Then, the arrival time fluctuations are used as a feedback on the Linacs to decrease the temporal jitter of the electron bunches entering the undulator. Second, external pulsed-laser sources are locked to the master laser via timing link outputs. In this way, the injector-, the seed- and the pump-laser at different locations of the FEL facility are synchronized with each other. Thirdly, the pulsed outputs of the timing links are used to lock microwave sources such as the klystrons of the Linacs using balanced optical-microwave phase detectors (BOMPDS) [59,60].

Prior to this thesis, the pulsed scheme had breached the 100-fs barrier demonstrating a timing precision of  $\sim 10$  fs for several hundred meters of fiber links [30,57]. However, delivering sub-femtosecond precision requires further development of the metrological devices (i.e., BOCs and BOMPDS) and deep physical understanding of optical pulse shaping in fiber transmission as well as its impact on optical/microwave timing measurements. This advanced level of physical and technical comprehension is the topic of this thesis.

### 1.3 LASER-BASED ATTOSCIENCE CENTERS

Several years ago, a new type of laser facility has been conceived with the desire of producing the highest electromagnetic field and the shortest pulse duration. The Extreme Light Infrastructure (ELI) is designed to be the first exawatt-class ( $10^{18}$  W) laser in the world [43,61]. The only way of reaching this enormous level of power is to pack kilojoules of energy into a pulse of few femtoseconds temporal duration. Analysis of the laser development history reveals that there is an inverse linear dependence between the laser intensity and the pulse duration [62]. Since the light pulses in optical frequencies are already as short as one cycle or even less, the pulses generated by the future high power laser facilities like ELI will be necessarily in the X-ray and  $\gamma$ -ray regimes. In this way, scientists will open doors to new horizons in fundamental science such as time-dependent studies of nuclear properties and vacuum nonlinearities [62].

Figure 1.3 shows the major laser sources of the ELI Attosecond Light Pulse Source (ALPS) planned to be built in Szeged, Hungary. ELI-ALPS will have three primary laser sources delivering few-cycle optical pulses with extremely broad bandwidth and sub-cycle phase control at exceptionally high repetition rates [63]. Several secondary light sources including isolated attosecond X-ray pulses and high-intensity THz beams will be generated by passing the primary laser sources through the appropriate nonlinear media such as gas or solid targets for HHG [64,65], and lithium niobate for tilted-pulse-front THz generation [66]. The advantage of using primary laser pulses consisting of only few wave cycles in HHG is that few zero-crossings of the driving electric field causes the highest energy X-ray photons to be emitted in few bursts [67]. As a result, generated

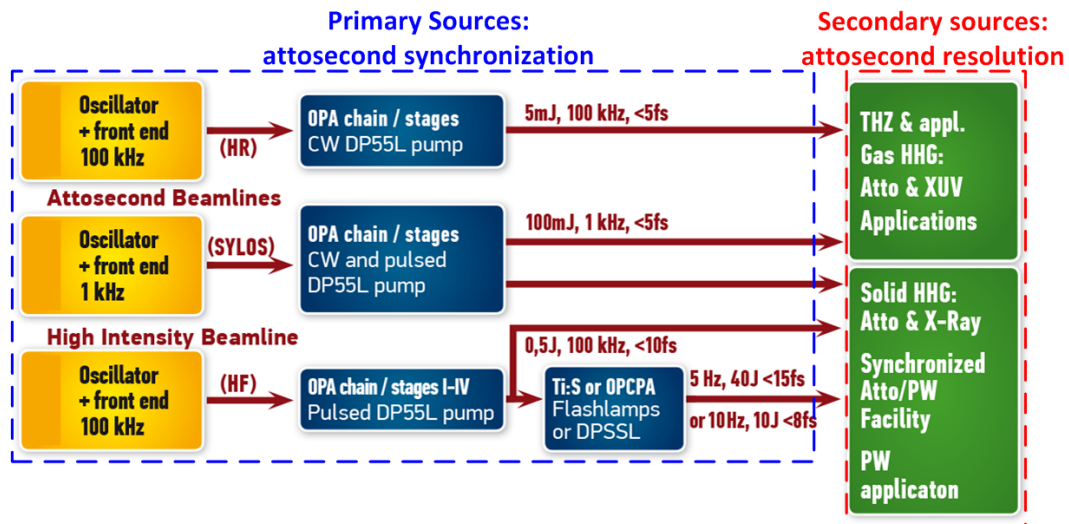


Figure 1.3: Layout of major laser sources of ELI-ALPS facility in Hungary.

Figure is reproduced from [63].

X-ray pulses acquire a continuous spectral distribution and hence attosecond pulse duration. The scientific mission of ELI-ALPS is to provide this broad range of ultrafast secondary light sources with attosecond relative synchronization to enable temporal investigations of electron dynamics in atoms, molecules, plasmas and solids on attosecond time scales [68]. To fulfill this ambitious scientific goal, one must ensure the internal stabilization of each primary laser source starting from the oscillator to the last optical parametric amplifier (OPA) as well as the relative synchronization of all primary sources with respect to each other with attosecond precision. Therefore, an attosecond precision timing distribution system will be an enabling technology also for the future high power laser facilities like ELI-ALPS.

## 1.4 SCOPE OF THE DISSERTATION

The objective of this thesis is to devise a timing distribution system which can breach the 1-fs precision barrier and enable attosecond timing of new generation photon science facilities. We can envision the required system as a synchronous laser-microwave network shown in Figure 1.4 where the timing signal of the master laser is transferred via a timing-stabilized fiber link network synchronizing various types of remote slave lasers and microwave sources with daily relative sub-fs timing jitter.

There are four basic elements to construct such a network which represent the thesis outline:

- Chapter 2: Timing detectors

Highly-precise timing detectors are the first elements to be realized since they determine the

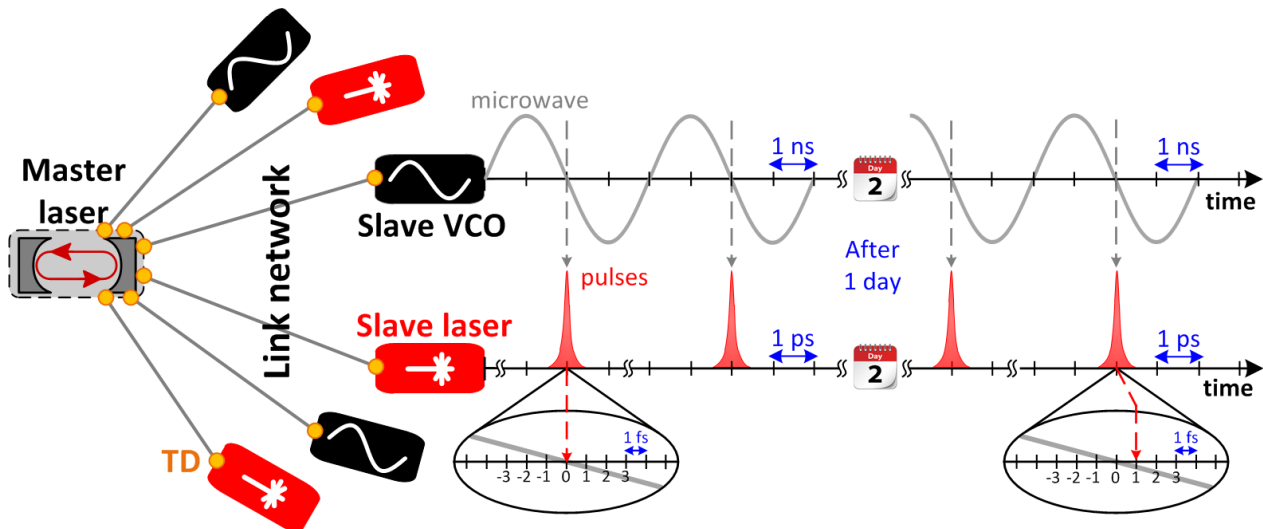


**Figure 1.4: Layout of a laser-microwave network with sub-fs daily jitter.**

The circled subgraphs under the time axis show the timing between the microwave signal (gray line, crossing at 0-fs) and the optical pulses (red dashed line). The filled orange circles represent timing detectors. VCO: voltage controlled oscillator; TD: timing detector.

ultimate precision of the complete system. BOCs and BOMPDs are our choice of timing detectors due to their attosecond timing resolution, long-term stability, amplitude invariance and robustness against environmental fluctuations. In Chapter 2, operation principles of BOCs and BOMPDs are described and compared with the conventional microwave phase detectors. Further developments achieved in the optical and microwave timing detection are outlined together with their analytical analysis to support long-term attosecond precision.

- Chapter 3: Master laser

Mode-locked lasers are our primary choice for the master oscillators since they can provide ultralow-noise optical and microwave signals simultaneously in the form of optical pulse trains. Chapter 3 examines the feasibility of our master laser to support a kilometer-scale timing network with attosecond precision together with the experimental results of the free-running timing jitter above 1-kHz and the achievements in the long-term frequency stability.

- Chapter 4: Noise-free fiber link transmission

Fiber-optic links are the preeminent choice to efficiently deliver optical signals to remote locations. However, in an unstabilized link, environmental fluctuations will induce errors in the arrival time of the delivered optical pulses. Chapter 4 starts with the traditional fiber link stabilization scheme where linear timing errors detected by the BOC is compensated by a PZT fiber stretcher and a motorized delay line. Experimental results achieved with this traditional scheme always possess a timing drift in the order of few femtoseconds that are highly correlated with the operational power fluctuations in the fiber links. Therefore, a comprehensive theoretical and numerical analysis is performed and presented in Section 4.3 to uncover the physical mechanism between the power fluctuations and the timing jitter of the pulses traveling inside the fiber links. The following effects are thoroughly investigated: BOC response to pulse temporal profile distortions, nonlinear pulse propagation in fibers, and feedback loop analysis of the fiber link stabilization. The outcomes of the numerical analysis provide fundamental guidelines to minimize long- and short-term noise sources in the fiber link transmission. In the light of these new findings, a genuinely noise-free fiber link network is presented in Section 4.4 showing a timing drift of only  $\sim 290$  as<sup>2</sup> within the locking bandwidth of the system [7  $\mu$ Hz - 1 kHz].

- Chapter 5: Laser and microwave synchronization

Timing precision of an operational timing distribution system is judged by the relative instability between the remote slave optical and microwave oscillators that are synchronized to the master laser by a fiber link network as depicted in Figure 1.4. Chapter 5 discusses the efficient synchronization of slave mode-locked lasers and microwave oscillators both locally and remotely

---

<sup>2</sup> The abbreviation 'as' of attosecond is used throughout the thesis after experimental results.

via timing stabilized fiber links. In Section 5.3, the high frequency noise sources of timing-distribution and remote-laser synchronization systems are investigated using a jitter analysis method based on feedback flow between setup elements. The feedback loop analysis yields an excellent agreement with the experimental results and identifies the noise sources in the system with their estimated timing jitter contributions. The presented analysis method can easily be adapted to different scenarios in order to optimize feedback control parameters and identify sources of noise within a complex synchronization network. With help of the feedback model, a synchronous mode-locked laser network is realized and its timing precision is improved from 9.3 fs RMS down to 0.67 fs RMS in the offset frequency range of 7  $\mu$ Hz - 1 kHz. Finally, Section 5.5 presents the first experimental demonstration of a large-scale attosecond-precision laser-microwave network that has the potential of enabling ultra-fast hard X-ray photon science facilities.

Please note that, in the context of this thesis we provide a general method to synchronize local and remote mode-locked lasers (i.e., oscillators in Figure 1.3) and microwave devices. Stabilization of laser amplifier chains such as front-end amplifiers and OPA stages is highly dependent on the chosen amplification scheme and geometry; therefore, it is outside of the scope of the thesis. However, interested readers can refer to the following papers for some more insight [69,70,71].

## 2 TIMING DETECTORS

### 2.1 MICROWAVE PHASE DETECTOR

The primary element to realize a high precision timing distribution system is the timing detector because it dictates the smallest timing error which can be detected by the system. The traditional method of measuring the timing jitter of ultrafast optical pulse trains is the direct photodetection with microwave electronics (i.e., microwave phase detection). The easiest way to comprehend the capabilities and limitations of this technique is to consider the following example shown in Figure 2.1(a). Output pulse trains from two mode-locked lasers with slightly different repetition rates are launched on two photodetectors which convert them to electronic pulses. Since the optical pulses generated by mode-locked lasers can be as short as few femtoseconds, the exact transformation into the electronic domain is far beyond the bandwidths of the current photodetectors. Consequently, the electronic pulses are relatively longer in time ( $> 10$  ps) whose exact shape and pulse duration is highly dependent on the optical pulse and the photodetector characteristics [72]. Therefore, direct comparison of the electronic pulse trains would not yield reliable timing information. However, one can extract a clean sinusoidal microwave signal that is in-phase with the optical pulse train by filtering a harmonic of the repetition rate from the electronic spectrum. Then, the timing error between the two optical pulse trains can be obtained by mixing the bandpass-filtered microwave signals using a double-balanced mixer. Alternatively, the filtered harmonic of one of the lasers can be mixed with a voltage-controlled oscillator (VCO, see Figure 2.1(a)) to determine the timing error between optical pulse trains and microwaves.

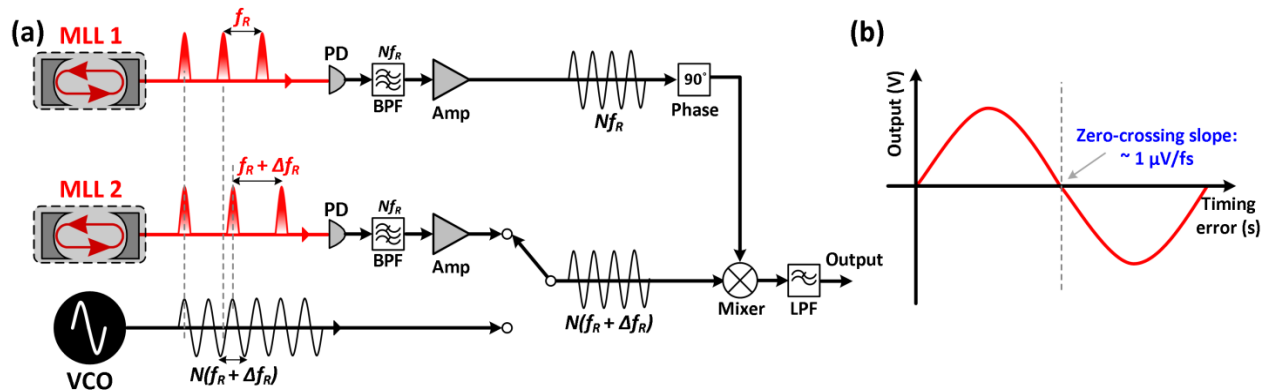


**Figure 2.1: Traditional approach to timing jitter measurement of optical pulse trains.**

(a) Block diagram of the microwave phase detector. (b) Typical voltage response of the microwave phase detector as a function of timing error. MLL: mode-locked laser; VCO: voltage-controlled oscillator; PD: photodetector; BPF: bandpass filter; LPF: low pass filter; Amp: low noise microwave amplifier; Phase:  $90^\circ$  phase shifter;  $f_R$ : repetition rate;  $\Delta f_R$ : frequency difference between the two inputs such that  $\Delta f_R \ll f_R$ .

As depicted in Figure 2.1(b), typical timing sensitivity values of microwave phase detectors are on the order of few microvolts per femtosecond. Even though this microwave approach is easy to implement and widely used in FEL timing distribution systems [31,73], it possesses several fundamental issues restraining its ultimate resolution to  $\sim 100$  fs [54]:

- Maximum signal-to-noise ratio that can be achieved by a certain phase noise measurement is limited by the fundamental noise sources such as thermal noise and shot noise. Assuming that we have a photodetector with  $1\text{ k}\Omega$  transimpedance amplifier and a photocurrent of  $0.1\text{ mA}$  at the filtered harmonic of the electronic spectrum, we get  $18\text{ }\mu\text{V}$  of shot-noise and  $13\text{ }\mu\text{V}$  of thermal noise at the output of a  $10\text{ MHz}$  low pass filter. Considering a timing sensitivity of  $1\text{ }\mu\text{V}/\text{fs}$ , the timing resolution of the microwave phase detector is only  $18\text{ fs}$  due to shot noise, which is unacceptable for attosecond timing applications.
- Relative intensity fluctuations of optical pulses lead to temporal shape deformations of the photodetected electronic pulses due to detector nonlinearities which in turn cause phase noise in the harmonics of the electronic spectrum (i.e., AM-PM conversion). One way to circumvent this issue is to find “zero AM-PM conversion points” of the photodiode by adjusting its bias voltage. However, this procedure is highly sensitive to the experimental parameters such as the diode, optical pulse duration, and temperature [72].
- The response of operational amplifiers and the transmission delay of coaxial cables are highly sensitive to the temperature. Hence, microwave phase detectors are prone to thermal drifts (e.g., a drift of  $350\text{ fs}/\text{K}$  measured in [74]) which degrade the long-term stability.

An alternative technique that is highly sensitive to timing of optical pulses is the sum-frequency generation in a nonlinear crystal. A pair of optical pulses is focused into a nonlinear medium where they create a third light pulse at their sum-frequency only if they overlap spatially and temporally (i.e., optical intensity cross-correlation). Therefore, the amount of light converted into the sum-frequency pulse is highly dependent on the pulse timing; whose integrated energy can easily be detected by a simple photodetector. In this way, one can detect timing fluctuations significantly smaller than the pulse duration itself. Since the timing detection is performed directly in the optical domain, this scheme is immune to temperature variations. One big disadvantage is that the generated sum-frequency pulse is also influenced by the amplitude fluctuations of the optical pulses. Therefore, a balanced optical-cross correlation scheme has been suggested by our former group members to perform pure timing measurements in the optical domain [56].

## 2.2 BALANCED OPTICAL CROSS-CORRELATOR

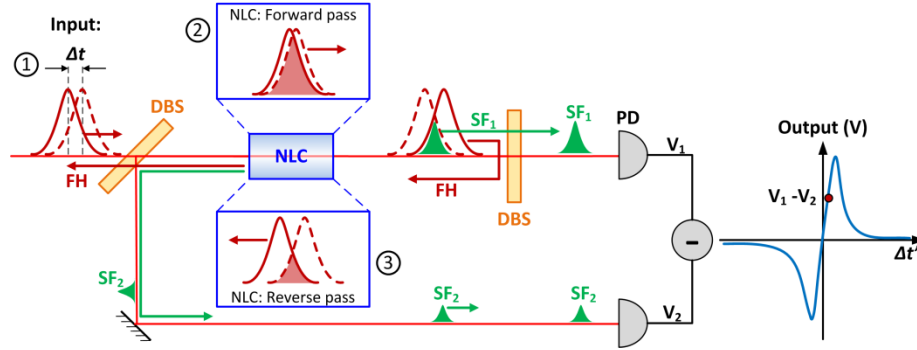


**Figure 2.2: Principle of timing detection using a BOC.**

FH: input pulses at fundamental harmonics; DBS: dichroic beam splitter; NLC: nonlinear crystal; PD: photodetector; SF<sub>1</sub> and SF<sub>2</sub>: generated sum-frequency pulses on the forward and reverse pass; V<sub>1</sub> and V<sub>2</sub>: photodetected voltages for SF<sub>1</sub> and SF<sub>2</sub>, respectively.

The main detector that we employ in our timing distribution system is the balanced optical cross-correlator (BOC) due to its attosecond timing resolution, long-term stability, amplitude invariance and robustness against environmental fluctuations. Timing detection principle of a BOC is shown in Figure 2.2. Two optical pulses (represented with red solid and dashed lines) whose relative timing is to be measured are launched into a nonlinear crystal in a double-pass configuration. As they propagate through the crystal, they walk through each other due to different group velocities and generate different amounts of sum-frequency light (represented as green pulses) depending on their temporal overlap in the forward and reverse pass. Generated sum-frequency pulses are separated from the fundamental harmonics by dichroic beam splitters after each pass and measured by two identical receivers of a balanced photodetector (BPD). The difference in the sum-frequency light cancels the optical intensity fluctuations and yields a voltage signal only proportional to the time separation of the input pulses.

Figure 2.3 shows the simulation results of a BOC using type-II second-harmonic generation in a periodically poled potassium titanyl phosphate (PPKTP) crystal with 4-mm length. The input pulses (Figure 2.3(a)) are identical with optical spectra centered at 1550 nm, FWHM pulse duration of 150 fs and repetition rate of 216 MHz, except that the energy of the first pulse is amplitude modulated for each calculation. Figure 2.3(b) illustrates the response of the BOC against the amplitude fluctuations with respect to different time delays between the pulses:  $\Delta t'$ .<sup>3</sup> As can be seen from the top graph, the forward and reverse pass create equal amount of sum-frequency light (V<sub>1</sub> and V<sub>2</sub>, respectively) at  $\Delta t' = 0$  which is invariant to the amplitude of the input pulses. In this way, balanced output of the BOC (see bottom graph in Figure 2.3(b) and its zoomed subplot) preserves its position

<sup>3</sup>The x-axes of the graphs are scaled as  $\Delta t' = \Delta t - \tau_0$  where  $\tau_0$  is the time delay the pulses experience before the second sum-frequency generation takes place, i.e., group delay introduced by the birefringence of the PPKTP.

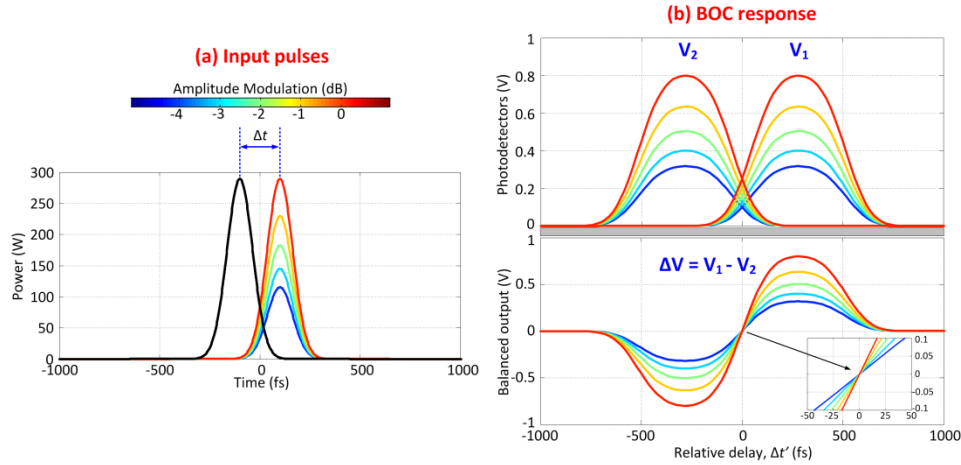


**Figure 2.3: BOC simulation results with an amplitude modulated input pulse.**

(a) Temporal profiles of the input pulses. The color map on top shows the amplitude modulation of the first pulse in dB scale and is common for all graphs. (b) Calculated BOC voltage response. Top graph shows the responses of the individual photodetectors of the BOC, whereas bottom graph shows their balanced (subtracted) output.

of zero voltage crossing, i.e.,  $\Delta t' = 0$  where it is immune to any first order amplitude fluctuations.

To compare the timing sensitivity of the BOC to the one of microwave phase detector, output pulse streams of two different mode-locked lasers with a small repetition rate mismatch ( $\Delta f_R \ll f_R$ ) are detected by both detectors simultaneously and their response is recorded with an oscilloscope. Figure 2.4 shows two snapshots of the oscilloscope readings taken in two different time scales. Both detectors yield periodic signals whose frequency is equal to the repetition rate difference of the mode-locked lasers. The time scale of the oscilloscope is calibrated by  $\Delta f_R / f_R$  to indicate the relative time scale of the detection (refer to Section 5.1 for a detailed discussion). As Figure 2.4(a) shows, the phase detector output (yellow trace) is a sinusoidal curve, whereas the BOC output (blue trace) is a train of sharp lines. In this time scale, one can deduce the timing sensitivity of the phase detector from the linear slope around the zero-crossing:  $\sim 1 \mu\text{V}/\text{fs}$ . In order to resolve the response of the BOC, one has to zoom in by three orders of magnitude in time from picosecond range to femtosecond range. In Figure 2.4(b), one can clearly see the difference in the timing sensitivities of both detectors. The BOC has a sharp linear slope around its zero voltage with  $\sim 2 \text{ mV}/\text{fs}$  timing sensitivity, whereas the response of the microwave phase detector is almost a flat line in this time scale. The green and purple traces illustrate the individual photodetector responses (i.e.,  $V_1$  and  $V_2$  as in Figure 2.3). Once the BOC output is used as a feedback signal to get rid of the repetition rate difference between the lasers, both photodetectors read 200 mV which corresponds to 40-as timing resolution due to shot noise in 10-MHz bandwidth.<sup>4</sup>

<sup>4</sup>The measured electronic noise is 11 as in 10-MHz bandwidth. Hence, this measurement is shot-noise limited.

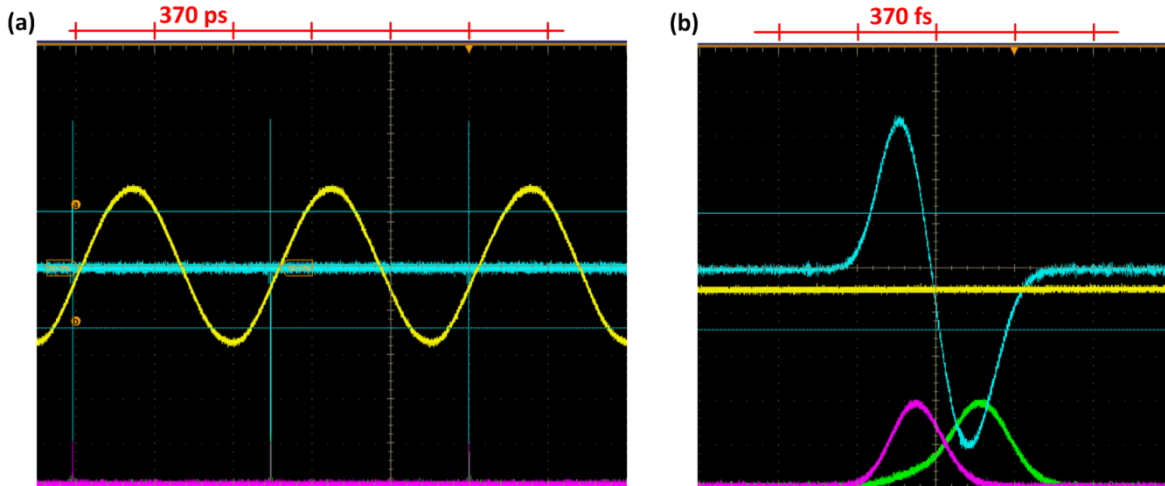


**Figure 2.4: Sensitivity comparison between a BOC and a microwave phase detector.** Oscilloscope traces taken in two different time scales (a) 370 ps and (b) 370 fs. Yellow trace: output of the microwave phase detector; blue trace: balanced output of the BOC; green and purple curves: individual photodetector response of the BPD (i.e.  $V_1$  and  $V_2$  as in Figure 2.3).

BOC is suitable for optical pulses either at different or at the same center wavelengths. For the former case, one can exploit all sum-frequency generation methods as long as one provides the necessary time delay between each cross-correlation paths. For pulses at the same center wavelength, one has to exploit second-harmonic generation using a nonlinear crystal with type-II phase matching and introduce group delays using the birefringence of the crystal. This is the most widely used BOC scheme in our timing distribution system as it is employed to stabilize the transmission delays of our fiber based timing links, where a laser pulse is cross-correlated with a link-delayed copy of itself (detailed in Chapter 4). Therefore, next section discusses the BOC scheme exploiting the type-II second-harmonic generation in PPKTP crystals and its improvements.

### 2.2.1 TYPE-II SECOND-HARMONIC BOC

Figure 2.5 shows the schematic of a type-II second-harmonic BOC using a PPKTP crystal. A polarization beam splitter spatially combines two orthogonally polarized pulse trains at 1550-nm center wavelength. The polarization of the pulses is fine-tuned by a half-wave plate in order to project them exactly on the ordinary and extra-ordinary optical axes of the PPKTP crystal. The input pulses travel in a double-pass configuration inside the crystal. The end facet of the crystal has a dichroic coating which is highly reflective for 1550-nm and anti-reflective for 775-nm wavelength. In this way, the second-harmonic pulse generated during the forward pass is separated from the fundamental harmonics. The dichroic beam splitter on the reverse pass is highly reflective for 775 nm at 45° incident and splits the other second-harmonic pulse from the fundamentals. Finally, a BPD converts the timing error between the input pulses into a voltage signal by detecting the power difference in the generated second-harmonics.

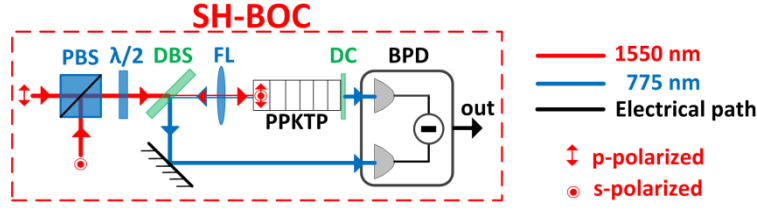


**Figure 2.5: Type-II second-harmonic BOC for input pulses at 1550 nm.**

PBS: polarization beam splitter;  $\lambda/2$ : half-wave plate; DBS: dichroic beam splitter; FL: focus lens; PPKTP: periodically poled potassium titanyl phosphate crystal; DC: dichroic coating; BPD: balanced photodetector.

Ideal second-harmonic generation for BOC is achieved when the polarization states of the input pulses are perfectly orthogonal to each other. However, the polarization extinction ratios of the optical elements used in the BOC do not completely satisfy this ideal case. For instance, we measure  $\sim 17$ -dB polarization extinction ratio between the two principal axes of a 3.5-km long polarization-maintaining (PM) dispersion-compensated fiber. Therefore, some portion of the optical power will always be projected along the undesired polarization axes of the nonlinear crystal. To investigate this effect, let's suppose the electric fields of the two input pulses are:

$$E_1(z, t) = A_1(z, t)e^{i(kz - \omega t)} \quad (2.1)$$

$$E_2(z, t) = A_2(z, t)e^{i(kz - \omega t - \varphi(t))} \quad (2.2)$$

where  $k$  is the wavenumber in the propagation direction  $z$ ,  $\omega$  is the temporal angular frequency and  $\varphi(t)$  is the phase difference between the fields. If the polarization directions of the two pulses are not perfectly aligned with the principle axes of the crystal as shown in Figure 2.6(a), the electric field of the generated second-harmonic pulse will be proportional to:

$$E_{SHG} \propto [A_1(z, t) \cos \theta_1 - A_2(z, t) \sin \theta_2 e^{-i\varphi(t)}][A_1(z, t) \sin \theta_1 + A_2(z, t) \cos \theta_2 e^{-i\varphi(t)}]e^{i(2kz - 2\omega t)} \quad (2.3)$$

where  $\theta_1$  and  $\theta_2$  are polarization mismatch angles of  $E_1$  and  $E_2$  with the respect to the principle axes of the PPKTP crystal ( $x$  and  $y$  axes). Then, the detected second-harmonic power is:

$$P_{SHG}(t) \propto \int_0^L |E_{SHG}|^2 dz \quad (2.4)$$

Using Equation (2.3):

$$P_{SHG}(t) \propto \int_0^L \left| [A_1(z, t) \cos \theta_1 - A_2(z, t) \sin \theta_2 e^{-i\varphi(t)}][A_1(z, t) \sin \theta_1 + A_2(z, t) \cos \theta_2 e^{-i\varphi(t)}] \right|^2 dz \quad (2.5)$$

where  $L$  is the crystal length. Therefore, the output power will be related to the polarization mismatch angles and fluctuate with the phase difference  $\varphi(t)$ . This will generate excess amplitude noise in the BOC which cannot be eliminated by the balanced detection.

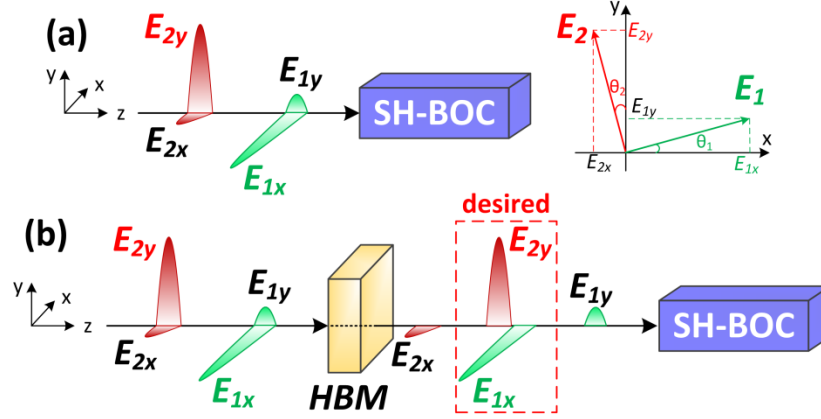


**Figure 2.6: Improving polarization extinction ratio of type-II SH-BOC.**

(a)  $E_1$  and  $E_2$  have finite polarization extinction ratios projecting  $E_{1y}$  and  $E_{2x}$  as noise sources on the opposite principle axes of the type-II crystal. (b) A highly birefringent material (HBM) can avoid this situation by spatially separating the undesired polarization components.

We are able to remove this noise from our detection using a highly birefringent material before the SH-BOC as described in Figure 2.6(b). The large birefringence spatially separates the undesired polarization components of the input pulses (i.e.,  $E_{1y}$  and  $E_{2x}$ ) so that only the desired ones (i.e.,  $E_{1x}$  and  $E_{2y}$ ) can generate second-harmonic light. Then, Equation (2.5) becomes:

$$\begin{aligned}
 P_{SHG}(t) &\propto \int_0^L |A_1(z, t) \cos \theta_1 A_2(z, t) \cos \theta_2|^2 |e^{-i\varphi(t)}|^2 dz \\
 &\propto \int_0^L |A_1(z, t) \cos \theta_1 A_2(z, t) \cos \theta_2|^2 dz
 \end{aligned} \tag{2.6}$$

Hence, there are no interference effects observed anymore in the second-harmonic generation due to the phase difference  $\varphi(t)$  between the input pulses. When employed in a timing distribution system, these polarization-noise suppressed BOCs will yield higher signal-to-noise ratio (SNR) and improve the long-term timing stability by removing the background intensity fluctuations of the undesired polarization components.

### 2.2.2 FIBER-COUPLED BOC USING PPKTP WAVEGUIDES

Current implementation of the optical timing distribution system makes use of type-II second-harmonic generation in bulk PPKTP crystals to stabilize the fiber links delivering the timing signal of the master laser to remote optical and microwave devices. However, operational FELs such as FLASH [75] and the European XFEL [38] aim to employ up to 25 fiber links to synchronize the complete facility, which requires tremendous attention to the alignment and stability of the free-space optics to minimize timing-drifts induced by beam pointing instabilities [76]. To provide more robustness and ease of implementation for such complex optical setups, we have developed fiber-coupled BOC (FC-BOC) using integrated PPKTP waveguides [77]. The use of fiber-coupled waveguides promises dramatic improvements in second-harmonic conversion efficiency which can

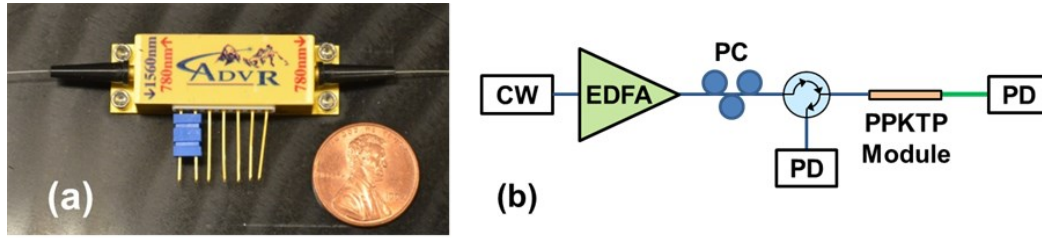


**Figure 2.7: Fiber-coupled BOC using PPKTP waveguides.**

(a) Photograph of a packaged fiber-coupled PPKTP based BOC module. (b) Schematic of the experimental setup for measuring the conversion efficiency. CW: continuous-wave laser; EDFA: erbium-doped fiber amplifier; PC: polarization controller; PD: photodetector. Figure is taken from our article [77].

decrease the power budget of the timing distribution systems and support more fiber links. Figure 2.7(a) shows a photograph of the fiber-coupled BOC which consists of a PPKTP waveguide module mounted on a temperature-controlled platform. The rear facet of the PPKTP chip has a dichroic coating that is anti-reflective at  $775 \pm 25$  nm and highly reflective at  $1550 \pm 50$  nm. The input port of the device is a standard PM fiber whose fast and slow axes are aligned with principles axes of the crystal. The second-harmonic light generated during the forward propagation is collected with a multimode fiber, whereas the reverse-generated second-harmonic is coupled back into the input fiber. Figure 2.7(b) is the schematic of the experimental setup built for measuring the conversion efficiency of the fiber-coupled waveguide. The output of a tunable cw laser is amplified by a fiber amplifier and coupled into the PPKTP waveguide through a fiber-polarizer and a fiber-circulator. The amount of light reflected at the fundamental harmonic is measured with the return port of the circulator to account for the coupling loss between the input fiber and the waveguide. The coupling loss is found to be  $\sim 3$  dB and the multimode fiber collects  $\sim 90\%$  of the forward-generated second-harmonic light. Figure 2.8(a) shows the second-harmonic light generated at the end of the waveguide as a function of the input power at the fundamental-harmonic.

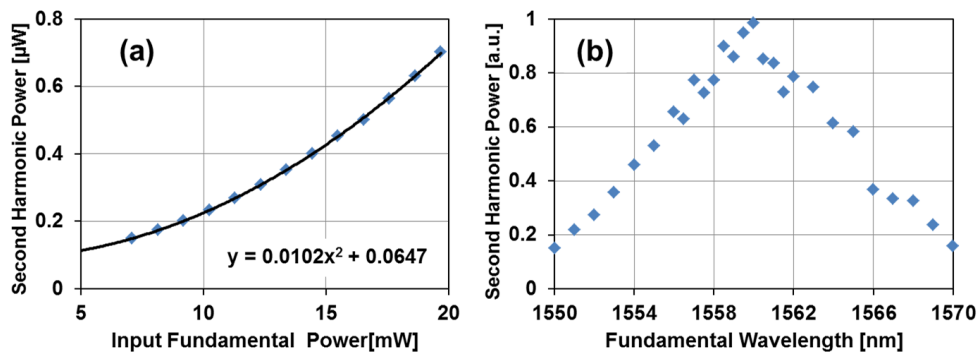


**Figure 2.8: Second-harmonic generation efficiency of the fiber-coupled BOC.**

(a) Second-harmonic power generated as a function of input power (after accounting for the coupling loss). Solid black curve: quadratic fit to the data. (b) Second-harmonic power as a function of input wavelength. Figure is taken from our article [77].

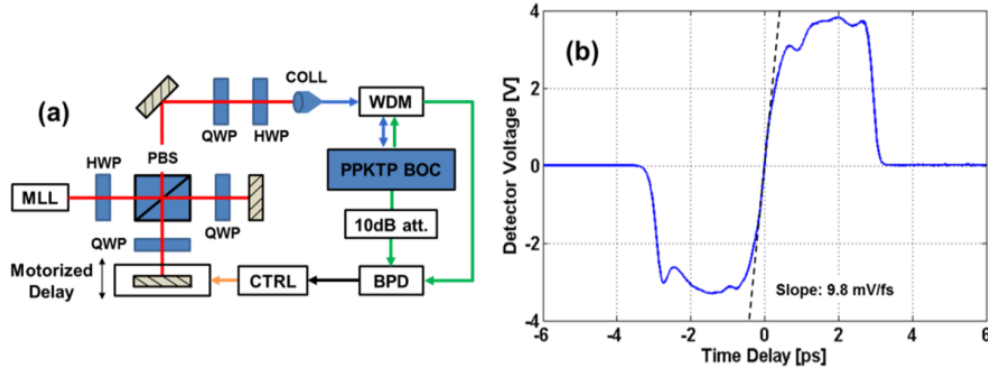


**Figure 2.9: Characterizing cross-correlation performance of the integrated BOCs.**

(a) Schematic of the experimental setup. (b) Recorded cross-correlation trace from the fiber coupled BOC as a function of the time delay between the two input pulse trains. MLL: mode-locked laser; HWP: half-wave plate; QWP: quarter-wave plate; PBS: polarization beam-splitter; COLL: collimator; WDM: wavelength-division multiplexer; BPD: balanced photo-detector; CTRL: controller. Figure is taken from our article [77].

We obtain a normalized conversion efficiency of  $1.02\% / [\text{W}\cdot\text{cm}^2]$  with a quadratic fit to the experimental data whose wavelength dependence is demonstrated in Figure 2.8(b). The highest conversion efficiency is achieved for 1560 nm which can be tuned to another wavelength of preference by adjusting the poling period of the PPKTP waveguide.

Next, we examine the performance of the fiber-coupled modules when operated as a BOC. Figure 2.9(a) illustrates the experimental setup for characterizing cross-correlation performance of the integrated BOCs. Output pulses from a mode-locked laser are split into orthogonal polarizations and delayed with respect to each other using a motorized delay stage. The pulses are coupled into fiber through a wavelength-division multiplexer (WDM) which serves as a fiber-coupled dichroic beam splitter and directs the input pulses into the waveguide for cross-correlation. The forward and backward second-harmonic signals are then fed to the ports of a BPD. Due to the spatial mode mismatch between the input PM fiber and the waveguide, the second-harmonic power collected on the forward path is approximately 10 dB higher than that of the reverse path. Therefore, a 10-dB attenuator is inserted in the forward path to symmetrize the cross-correlation curve. A recorded cross-correlation trace of the fiber coupled BOC is shown in Figure 2.9(b) as a function of the time delay between the two input pulse trains exhibiting a timing sensitivity of 9.8 mV/fs.

We examine the thermal dependence of the device by measuring the timing sensitivity at different operational temperatures as shown in Figure 2.10(a). FC-BOCs show very little deviations in timing sensitivity with respect to the applied temperature around the typical operating point of  $25^\circ\text{C}$  indicating a robust waveguide performance and fiber coupling efficiency against environmental fluctuations. As the temperature is further increased to  $40^\circ\text{C}$ , the timing sensitivities shift slightly which is most likely attributed to a slight change in the phase matching between the modes in the waveguide.

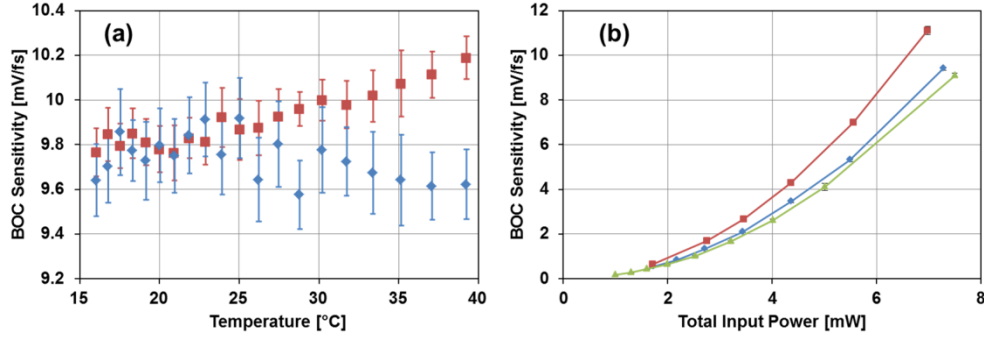


**Figure 2.10: FC-BOC sensitivity as function of (a) temperature and (b) input power.**

Red squares and blue diamonds represent the results achieved with two different FC-BOCs, whereas green triangles represent a typical bulk-optic BOC for comparison. Figure is taken from our article [77].

We compare the performance of the FC-BOCs against the free-space bulk optics BOCs by measuring their timing sensitivities as a function of average input power as can be seen in Figure 2.10(b). Even though the FC-BOCs are operated with a 10-dB attenuator due the second-harmonic coupling losses in the reverse pass, they exhibit performance quite comparable to the results achieved with bulk optics cross-correlators. Currently, a next generation FC-BOC with an integrated WDM is being designed to eliminate the coupling problem, which is expected to outperform the previous FC-BOC by at least one order of magnitude.

### 2.2.3 BOC TIMING SENSITIVITY CHARACTERIZATION

Timing sensitivity of a BOC is given by the linear slope around the zero-crossing of its response voltage. There are two experimental methods to characterize the timing sensitivity. The first case is when the two input pulse trains have the same repetition rate<sup>5</sup>. For instance, they may originate from a single source and one of them is time delayed with respect to the other (e.g., in fiber-link stabilization experiments presented in Chapter 4). In this case, the relative delay between the pulse trains is swept with a motorized delay stage, while the response voltage of the BOC is recorded with a data acquisition element. In the second case, the two input pulse trains have different repetition rates (e.g., synchronization of two mode-locked lasers as detailed in Chapter 5). When the pulse trains are combined in a BOC, the output voltage is a train of characteristic BOC traces whose frequency is equal to the repetition rate difference of the input pulses. One can simultaneously record a BOC trace on an oscilloscope and measure the instantaneous repetition rate difference with a phase detector. In this case, one has to ensure a small repetition rate mismatch (e.g., <50 Hz) so that the bandwidth of the BPD is sufficient to resolve the linear slope. The real time scale of the BOC trace is obtained by multiplying the time scale of the oscilloscope by the ratio of the repetition rate difference to the repetition rate of the master laser (refer to Section 5.1 for detailed derivation).

<sup>5</sup>Rigorously speaking: relative jitter between the pulse trains is much smaller than the pulse repetition period.

## 2.3 BALANCED OPTICAL-MICROWAVE PHASE DETECTOR

High brilliance coherent X-ray radiation can be extracted from electron bunches only if they simultaneously possess relativistic energies ( $>1$  GeV), ultra-short temporal duration ( $<50$  fs) and extremely low kinetic energy dispersion ( $<0.1$  %). While laser-plasma based electron accelerators are still struggling to meet these requirements, FELs can already achieve X-ray laser amplification thanks to the matured and efficient microwave electronics and Linacs. Since FELs employ many optical and microwave sources in a synchronous operation to generate their radiation, the ability to detect timing fluctuations between optical pulses and microwave signals with attosecond resolution will open a new regime of light and electron bunch control in next generation light sources. Therefore, a high precision timing distribution system must utilize an efficient optical-to-microwave timing detector. To overcome the disadvantages of microwave phase detection mentioned at the beginning of this chapter, an alternative method has been developed by our former group members which relies on timing detection between an optical pulse and a microwave signal in the optical domain before photodetection [78,79]. The basic idea of such an optoelectronic phase-locked loop (PLL) is presented in Figure 2.11. The optical pulse train is split into two parts with equal intensities and guided into two amplitude modulators which are driven by the microwave source with  $180^\circ$  phase difference in between. In this way, the phase error<sup>6</sup> between the optical pulse train and the microwave source is transferred into an intensity imbalance between the two split beams in the optical domain. The intensity difference is detected by a balanced detector which will read zero only when the optical pulses arrive to the amplitude modulators simultaneously with the zero-crossings of the microwave signal. Any phase shift from this position will create a non-zero error signal that

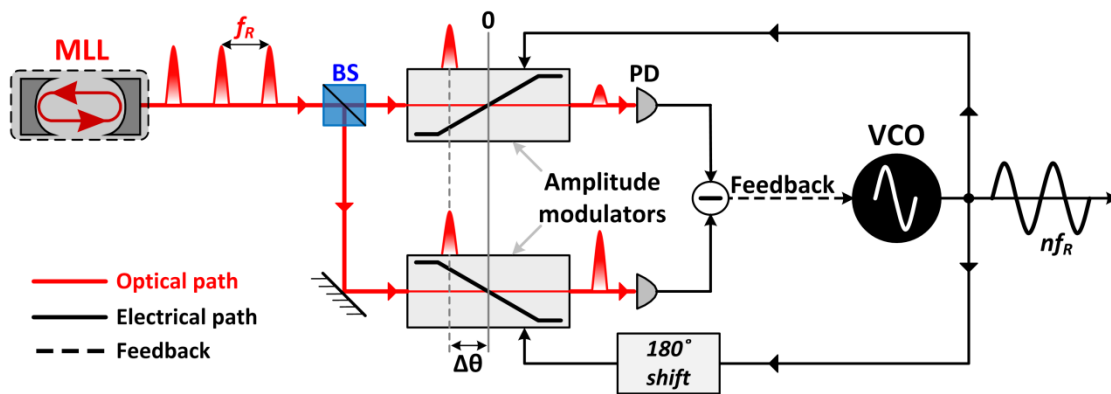


**Figure 2.11: Optical-to-microwave phase detection with balanced intensity detector.**

MLL: mode-locked laser; BS: beam splitter; PD: photodetector;  $f_R$ : optical pulse repetition rate; VCO: voltage controlled oscillator;  $\Delta\theta$ : phase error between the MLL and VCO.

<sup>6</sup>i.e., between the zero-crossing of the microwave and temporal center of gravity of the optical pulse. Analogously, it can also be expressed as a timing error.

can be fed back to the microwave source (e.g., a VCO) to correct for its phase error with respect to the optical pulse (or vice versa). In this way, the optoelectronic PLL is immune to the amplitude fluctuations of both optical and microwave sources and consequently not susceptible to excess AM-PM conversion in the photodetection (i.e., balanced intensity detector). Now the challenge is shifted to the optical side to realize  $180^\circ$  out-of-phase amplitude modulators with drift-free bias points. An ideal candidate for this task is a Sagnac-interferometer (SGI) with a unidirectional phase modulator where the two split optical pulses travel the same path in opposite directions and experience same environmental fluctuations. Upon balanced detection, these common mode noise factors will cancel each other and provide drift-free bias points. Such an interferometer can easily be constructed with robust fiber-optic components including a unidirectional electro-optic phase modulator and a 50:50 fiber coupler, whose ports on one side are connected to the modulator (see Figure 2.12(a)). In this way, the optical input is divided into two pulse trains with equal amplitudes propagating in the fiber loop in opposite directions. The fiber coupler is designed such a way that it ensures  $180^\circ$  phase shift between the pulses every time when they recombine at the output port. When the unidirectional phase modulator ( $\phi$  in Figure 2.12(a)) is appropriately fed with the target microwave signal, the output voltage  $\Delta V$  of the balanced optical-microwave phase detector (BOMPD) will represent the phase error  $\Delta\theta$  between the zero-crossing of the microwave and temporal center of gravity of the optical pulse [59,60].

Phase detection of the BOMPD is best understood by analyzing the SGI transmission function:

$$P_{out} = P_{in} \sin^2(\varphi/2) \quad (2.7)$$

for different biasing conditions via the unidirectional phase modulator where  $P_{in}$  and  $P_{out}$  are the average input and output power and  $\varphi$  is the phase difference between the counter-propagating pulses. Figure 2.12(b),(i) illustrates the simplest case when there is no modulation (i.e.,  $\varphi=0$ ) and the pulses interfere destructively resulting in zero SGI output. In case (ii), a bias signal is applied to drive the SGI output at its most phase sensitive point. The phase sensitivity can be calculated as:

$$\frac{\partial P_{out}}{\partial \varphi} = \frac{P_{in}}{2} \sin(\varphi) \quad (2.8)$$

In order to have maximum sensitivity (i.e., steepest slope), the phase difference must be  $\varphi = \mp\pi/2$  (i.e., alternating quadrature bias). Such a bias signal is best derived from the input optical pulse train filtered at an odd harmonic and frequency divided by a factor of two [60]:

$$\varphi(t) = V_b \sin[2\pi(m + 0.5)f_R t + \Delta\phi] \quad (2.9)$$

where  $V_b$  is the phase modulation amplitude and  $\Delta\phi$  is the fixed relative phase between the pulse train and the derived bias signal. The input of the SGI is non-zero only when  $t_n = n/f_R$  (i.e.  $P_{in}(t_n) \neq 0$  where  $n$  is an integer). In this case, the phase difference due to the bias signal is:

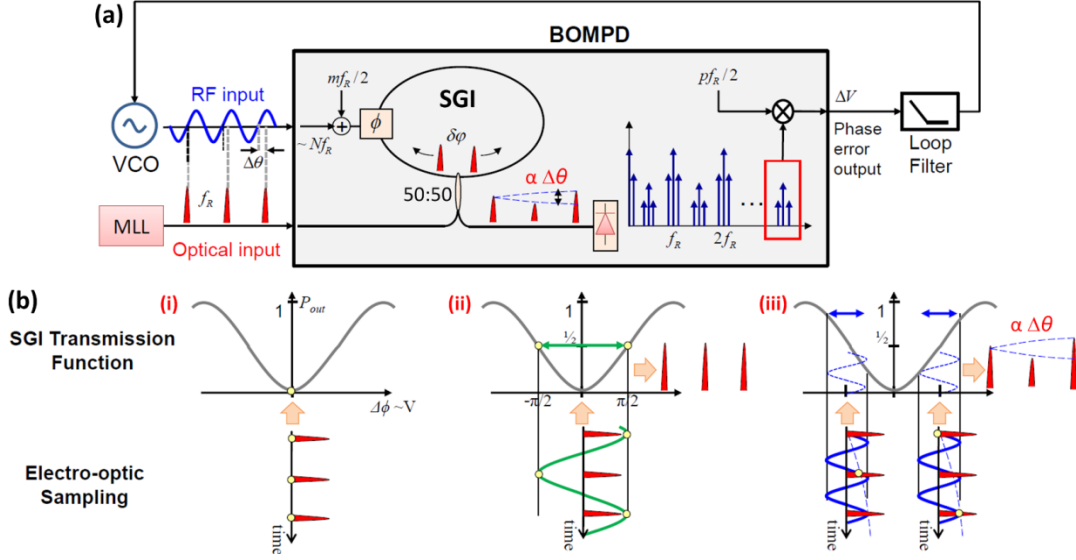


**Figure 2.12: Operation principles of BOMPD and Sagnac-interferometer.**

(a) General schematic to synchronize a VCO to a mode-locked laser. (b) Electro-optic sampling in Sagnac-interferometer for different biasing conditions of the phase modulator; (i) no modulation, (ii) modulation at alternating quadrature bias (i.e.,  $mf_R/2$ ), (iii) modulation with VCO signal in addition to the quadrature bias. MLL: mode-locked laser; SGI: Sagnac-interferometer; 50:50: fiber coupler; BOMPD: balanced optical-microwave phase detector. Figure is reproduced from [60].

$$\varphi(t) = (-1)^n V_b \sin(\Delta\phi) \quad (2.10)$$

Therefore, highest phase sensitivity is ensured only when:

$$V_b \sin(\Delta\phi) = \pi/2 \quad (2.11)$$

Under this phase modulation, SGI transmission function yields a constant value:

$$P_{out}(t) = P_{in} \sin^2(\varphi(t)/2) = P_{in}/2 \quad (2.12)$$

Therefore, the sub-pulses recombining at the SGI output will have no amplitude modulation. This biasing point will serve as a reference level for the subsequent phase error detection.

Finally, in the case (iii) of Figure 2.12(b), the target microwave signal with a frequency equal to a multiple of the repetition rate (i.e.,  $f_0 = Nf_R$  when locked) is added to the phase modulator in addition to the quadrature bias. In this way, the differential phase of the SGI is given by:

$$\varphi(t) = V_0 \sin[2\pi Nf_R t + \Delta\theta] + V_b \sin[2\pi(m + 0.5)f_R t + \Delta\phi] \quad (2.13)$$

where  $V_0$  is the phase modulation amplitude of the microwave signal and  $\Delta\theta$  is the phase error between the pulse train and the microwave signal. If  $\Delta\theta$  is small ( $\Delta\theta \ll 1$ ), then the phase difference for sub-pulses recombining with a period  $t_n = n/f_R$  at the quadrature bias is:

$$\varphi(t) \approx V_0 \Delta\theta + (-1)^n \pi/2 \quad (2.14)$$

By inserting Equation (2.14) into the SGI transmission function:

$$P_{out}(t_n) = \frac{P_{in}}{2} [1 + (-1)^n \sin(V_0 \Delta\theta)] \quad (2.15)$$

The second term in Equation (2.15) immediately reveals that there will be an amplitude modulation between the successive pulses recombining at the SGI output with a modulation depth<sup>7</sup>:

$$\Delta P_{out} = P_{out}(t_{n+1}) - P_{out}(t_n) \approx P_{in} V_0 \Delta\theta \quad (2.16)$$

which is proportional to the phase error  $\Delta\theta$  between the optical pulse train and the microwave signal. Upon detection, the amplitude modulated pulse train will contain error sidebands centered at the half repetition rate harmonics. Finally, one of the sidebands is bandpass filtered and down-converted with another reference signal in-phase to generate the desired phase error at baseband.

### 2.3.1 FREE-SPACE-COUPLED BOMPD

Former designs of the BOMPD have achieved promising local synchronization results with  $\sim 1$ -fs precision in short time scales (below 1 s) [60]. Nonetheless, they all suffer from long-term timing fluctuations and locking-volatilities stemming from their vulnerability against environmental changes. To improve the timing stability of BOMPD, we have developed free-space-coupled BOMPD (FSC-BOMPD) as shown in Figure 2.13. Key improvements in this BOMPD architecture are as follows. First, free-space optical components are used for the optical beam distribution to the SGI and the photodetectors of the bias and reference paths. Total fiber length of the SGI is spliced to be as short as possible. Compared with the fiber-coupled approach [59,60], free-space optics effectively reduce the long-term drifts caused by the environment. Second, high-frequency operation (multi GHz) at the quadrature bias arm ensures unidirectional modulation in the phase modulator. Since the counterclockwise pulses do not accumulate phase in the modulator anymore, the SGI becomes repetition rate independent and is more robust against unequal path lengths and environmental fluctuations. Third, down-mixing of the detected SGI output is performed at the lowest frequency

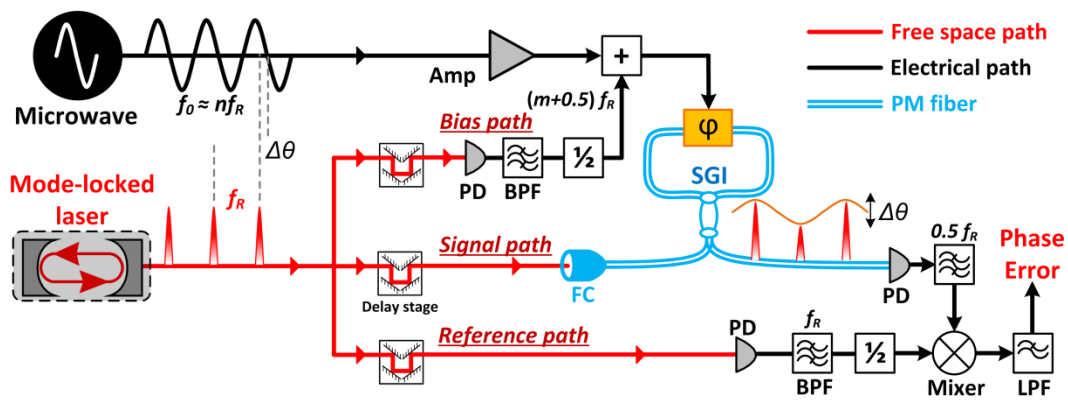


**Figure 2.13: Schematic of free-space-coupled BOMPD.**

$\Delta\theta$ : Phase error between the microwave and optical pulse train; PD: photodetector; BPF: bandpass filter;  $\frac{1}{2}$ : frequency divider; +: microwave diplexer; Amp: electronic amplifier; LPF: lowpass filter;  $\varphi$ : phase modulator; SGI: Sagnac-interferometer; FC: fiber collimator.

<sup>7</sup>Small angle approximation since ( $\Delta\theta \ll 1$ ),  $\sin(V_0 \Delta\theta) \approx V_0 \Delta\theta$

possible (i.e.,  $f_R/2$ ) to maximize SNR at photodetection and to minimize thermally induced phase changes in the reference path. Fourth, free-space delay stages are employed to adjust the relative time delay (or phase after photodetection) between the BOMPD paths which allow precise phase tuning without backlash, microwave reflection and excess loss when compared to electronic phase shifters. Lastly, an AM-PM suppression ratio of -50 dB is achieved by carefully optimizing AM- and PM-sensitive components in the reference and bias paths.

Next, we analytically derive the phase error output of FSC-BOMPD. Since the optical pulses have very short temporal durations ( $\sim 170$  fs), they can be approximated by a train of delta functions:

$$P_{in}(t) = P_{ave}T_R \sum_{n=-\infty}^{\infty} (1 + \Delta_{RIN}(t)) \delta(t - nT_R - \Delta_j(t)) \quad (2.17)$$

where  $P_{ave}$  is the average optical power,  $T_R=1/f_R$  is the period of the pulse train,  $\Delta_{RIN}(t)$  optical relative intensity noise (RIN) and  $\Delta_j(t)$  is the timing jitter of the pulse train. According to the BOMPD schematic in Figure 2.13, the driving signal of the phase modulator is:

$$\phi(t) = V_0 \sin[2\pi f_0(t + \Delta t_0)] + V_b \sin[2\pi(m + 0.5)f_R(t + \Delta t_b) + \Delta\phi] \quad (2.18)$$

where  $V_0, f_0$  and  $\Delta t_0$  are the amplitude, frequency and the timing jitter of the input microwave signal. This time, we also consider the relative timing jitter between the pulse train and the quadrature bias signal  $\Delta t_b$ , beside their fixed phase difference  $\Delta\phi$ . After circulating and recombining in the SGI, the output optical power can be expressed as:

$$P_{out}(t) = P_{ave}T_R \sum_{n=-\infty}^{\infty} \sin^2 \left[ \frac{1}{2} V_0 \sin(2\pi f_0 t + \Delta\theta) + \frac{1}{2} V_b \sin(2\pi(m + 0.5)f_R t + \Delta\beta + \Delta\phi) \right] (1 + \Delta_{RIN}) \delta(t - nT_R) \quad (2.19)$$

$\Delta\theta = 2\pi f_0(\Delta t_0 + \Delta_j)$  is the desired phase error between the pulse train and the microwave signal, whereas  $\Delta\beta = 2\pi f_R(m + 0.5)\Delta t_b$  is the phase fluctuation in the bias path. When the optical and microwave signal are locked to each other by the FSC-BOMPD,  $f_0 = n f_R$  where  $n$  is an integer. Since  $\delta(t - nT_R)$  is nonzero only if  $t = nT_R$  and we deal with small phase fluctuations, i.e.,  $\Delta\theta, \Delta\beta \ll 1$ , Equation (2.19) becomes:

$$P_{out}(t) \approx \frac{P_{ave}T_R}{2} \sum_{n=-\infty}^{\infty} [1 - \cos(V_0\Delta\theta + (-1)^n V_b \sin(\Delta\phi + \Delta\beta))] (1 + \Delta_{RIN}) \delta(t - nT_R) \quad (2.20)$$

Using the quadrature bias requirement in Equation (2.11), the SGI output yields:

$$P_{out} \approx \frac{P_{ave}T_R}{2} \sum_{n=-\infty}^{\infty} \left[ 1 + V_b \left( -\frac{\Delta\beta^2}{2} \sin(\Delta\phi) + \Delta\beta \cos(\Delta\phi) \right) \right] (1 + \Delta_{RIN}) \delta(n - T_R) + \frac{P_{ave}T_R}{2} \sum_{n=-\infty}^{\infty} V_0 \Delta\theta (1 + \Delta_{RIN}) \delta(t - nT_R) e^{i2\pi \frac{f_R}{2} t} \quad (2.21)$$

The first term on the right hand side of Equation (2.21) is related to the phase fluctuations in the bias path  $\Delta\beta$  and it appears in the frequency spectrum only at the harmonics of the pulse repetition rate, i.e.,  $nf_R$ . The second term, on the other hand, carries the desired phase error information  $\Delta\theta$  and represents itself only at the half frequencies of odd harmonics, i.e.,  $(m+0.5)f_R$ . In this way, the FSC-BOMPD is immune to bias path fluctuations contaminating the phase error detection. The reference signal for the down-conversion is also derived from the optical pulse train as shown in Figure 2.13:

$$V_r(t) = V_r \sin(2\pi \frac{f_R}{2} t + \Delta\Phi) \quad (2.22)$$

where  $V_r$  is the amplitude of the reference signal and  $\Delta\Phi$  is the relative phase fluctuations between the reference path and optical pulse train. After the down-conversion, we obtain the phase error:

$$V_e = \left[ \frac{C}{2} (1 + \Delta_{RIN}) P_{ave} T_R V_r V_0 \cos(\pi f_R \Delta\Phi) \right] \Delta\theta \quad (2.23)$$

where  $C$  is a coefficient related to the electronics in the down-conversion. Since the RIN of current mode-locked lasers is extremely low ( $<0.1\%$ ), the contribution from  $\Delta_{RIN}$  is negligible. Furthermore, down-conversion at a low frequency ( $f_R/2$ ) is advantageous in terms of avoiding the thermally induced phase drifts in the reference path. For example, at 216 MHz, 3-mm length fluctuation can only introduce  $2 \times 10^{-5}$  relative change. Therefore, the output error signal of FSC-BOMPD is mainly affected by the relative phase noise between the optical pulse train and the microwave signal  $\Delta\theta$ .

### 2.3.2 BOMPD PHASE SENSITIVITY CHARACTERIZATION

Timing sensitivity of a BOMPD is given by the linear slope around the zero-crossing of its response voltage in units of V/rad. When the outputs of a free running microwave oscillator and a mode-locked laser are combined in a BOMPD, their effective frequency difference is  $f_{beat} = f_0 \bmod f_R$  where  $f_0$  is the frequency of the microwave signal and  $f_R$  is the repetition rate of the mode-locked laser. The voltage response of the detector will be a train of characteristic BOMPD traces with a frequency equal to  $f_{beat}$ . One can record the frequency difference and a BOMPD trace simultaneously on an oscilloscope. The time scale of the oscilloscope is calibrated by multiplying it with the frequency difference  $2\pi f_{beat}$  to represent the phase error between the optical and microwave signal with respect to the microwave frequency. Analogously, the timing sensitivity in units of V/s can be obtained by further multiplying the phase sensitivity with the microwave frequency  $2\pi f_0$ .

### 3 MASTER LASER

Choosing the most appropriate master oscillator holds a great importance for a timing distribution system since it provides the necessary timing information to synchronize the entire facility. In this thesis, we develop a pulsed, optical timing distribution system relying on timing signals generated by a mode-locked laser. A mode-locked laser can simultaneously provide ultralow-noise optical and microwave signals in the form of optical pulse trains. Therefore, it has the inherent advantage to enable high-precision timing networks that can tightly synchronize multiple microwave and optical sources. Choosing a mode-locked laser as the master oscillator has many advantages when compared to cw techniques used in FEL synchronization [31,54,73] and frequency metrology [15,32,80]. First, a mode-locked laser eliminates the need for additional optical frequency combs at each end station since it provides ultrashort optical pulses as time markers for precision timing measurements. Second, mode-locked lasers exhibit orders-of-magnitude higher timing stability in comparison to best microwave oscillators [20,21]. Finally, any harmonic of the repetition rate can be extracted to phase-lock microwave oscillators and the optical pulse train can directly be used to synchronize remote pulsed lasers and to seed optical amplifiers. However, timing transfer by means of pulsed-laser oscillators requires kilometer-long, polarization-maintaining and dispersion-compensated fiber links which may influence the cost effectiveness of the system. Nonetheless, this is a trivial problem rather than a fundamental limitation which may become obsolete in the near future with the development of fiber technology [81].

Being the heart of our timing distribution scheme, low-noise performance of the master laser is of tremendous importance, especially for frequencies higher than the locking bandwidth of the feedback loops employed. In the next sections, we describe short- and long-term reliability and the low-noise operation of our master laser.

#### 3.1 TIMING JITTER CHARACTERIZATION

Recently, there has been a remarkable progress in lowering the timing jitter of mode-locked lasers. Numerous designs of solid-state and fiber lasers have been demonstrated with inherent timing jitters below 100 as [21,22,23]. Even though these state-of-the-art lasers already satisfy the precision requirements of sub-fs timing distribution systems, they require constant realignment and maintenance to keep long-term stable operation. However, the reliability of the master laser in long-term performance is of tremendous importance, since a failure of the synchronization system may completely interrupt the machine operation. Therefore, the most appropriate choice of mode-locked

laser would be a robust, commercially available, turnkey system to realize a high precision timing distribution system.

The timing signal is encoded in the precise repetition rate of the master laser. Temporal duration fluctuations between consecutive laser-pulses are termed as timing jitter and cause variations in the pulse repetition rate. Hence, timing jitter characterization of the master laser is a crucial step in constructing a precise timing distribution system, in order to choose the laser with lowest possible noise. Our master laser is a commercially available mode-locked laser (Origami-15 from OneFive GmbH) operating at 216.67-MHz repetition rate with 1554-nm center wavelength and 172-fs pulse duration. As discussed in the previous chapter, timing jitter characterization of mode-locked lasers has been performed traditionally with photodetectors (see Figure 2.1) [82]. In this technique, a harmonic of the photodetected electronic spectrum is filtered out with a bandpass filter and the phase noise of the obtained microwave is converted to amplitude change by mixing with a lower noise local-oscillator (see Figure 2.1(a)) [83]. Even though this scheme has been widely adapted by the current state-of-the-art signal source analyzers, it suffers from excess AM-PM noise conversion [72,84] and large noise floors. Here, we use an optical timing jitter characterization method based on BOCs [85] which can provide attosecond resolution and is intrinsically immune to AM-PM noise conversion (for details please refer to Section 2.2).

Figure 3.1 shows the experimental setup for timing jitter characterization of the master laser using a BOC. The cross-correlation scheme used here is a type-II SH-BOC using a PPKTP crystal as presented in Section 2.2.1 and requires two identical mode-locked lasers (two Origami-15s) whose repetition rates are synchronized in a master-slave configuration. The output pulse trains of the lasers are combined on polarization beam splitter and launched into the SH-BOC. The error signal is processed by a proportional-integral (PI) servo controller and fed back to slave laser's PZT to lock its repetition rate to that of the master laser. Electronic power spectral density of the BOC output

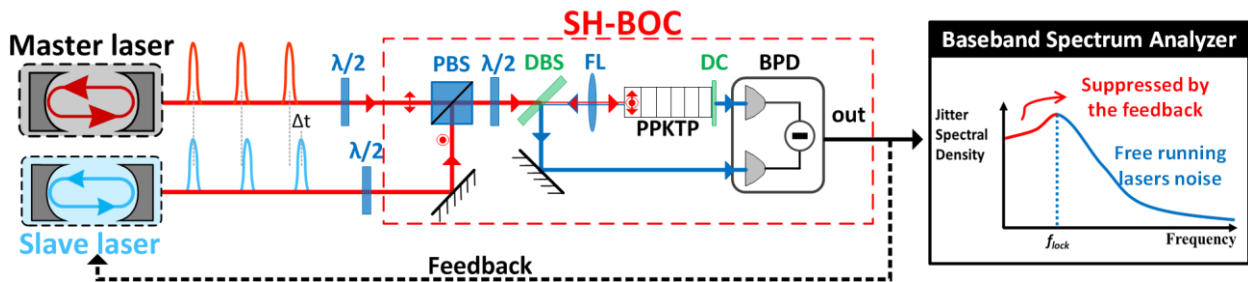


**Figure 3.1: Experimental setup for timing jitter characterization of the master laser.**  $\lambda/2$ : half-wave plate; PBS: polarization beam splitter;  $\Delta t$ : timing jitter between two pulse trains; DBS: dichroic beam splitter; PPKTP: periodically poled potassium titanyl phosphate crystal; DC: dichroic coating; and BPD: balanced photodetector.

when observed with a baseband spectrum analyzer is converted to timing jitter spectral density by using the timing sensitivity.<sup>8</sup> Once locked, the lasers' inherent jitter can be observed directly for frequencies beyond the locking bandwidth.

Influence of the BOC-lock on the measured timing jitter is best understood with a feedback loop analysis as described in Figure 3.2. According to this model, timing jitter between the master and the slave laser is converted to a voltage signal by the BOC transfer function  $H_{BOC}$ , and amplified by the BPD transimpedance gain  $H_{BPD}$  together with the detector noise  $E_{BOC}$ . Then, the voltage signal is fed to the PI controller with a transfer function  $H_{PI}$  in a negative feedback configuration. Finally, the PI output and its electronic noise  $E_{PI}$  are amplified and converted back to a time delay by the slave laser's PZT with a transfer function  $H_{PZT}$ . As a result of this feedback loop, relative timing jitter between the two lasers at the BOC input is given by:

$$J_O = J_M + J_S + [-(J_O H_{BOC} + E_{BOC})H_{BPD}H_{PI} + E_{PI}]H_{PZT} \quad (3.1)$$

where  $J_M$  and  $J_S$  are the free-running jitter of the master and the slave laser. By defining the electronic noise jitter term  $J_N$  and the total transfer function  $H$  (for details refer to Appendix A.1):

$$J_N = -\frac{E_{BOC}}{H_{BOC}} + \frac{E_{PI}}{H_{BOC}H_{BPD}H_{PI}} \quad (3.2)$$

$$H = H_{BOC}H_{BPD}H_{PI}H_{PZT} \quad (3.3)$$

Equation (3.1) becomes:

$$J_O = \left(\frac{1}{1+H}\right)(J_M + J_S) + \left(\frac{H}{1+H}\right)J_N \quad (3.4)$$

Since  $J_M$ ,  $J_S$  and  $J_N$  are uncorrelated noise sources with respect to each other, the mean values of their cross products is zero. Therefore, the average timing jitter spectral density detected by the BOC is:

$$\overline{J_O^2} = \left|\frac{1}{1+H}\right|^2 (\overline{J_M^2} + \overline{J_S^2}) + \left|\frac{H}{1+H}\right|^2 \overline{J_N^2} \quad (3.5)$$

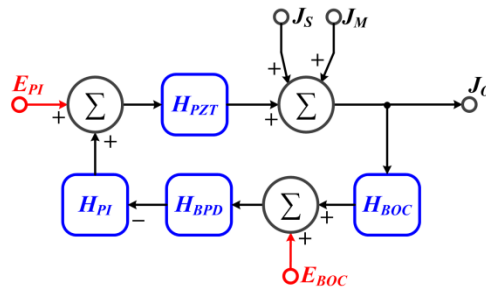


**Figure 3.2: Feedback model for BOC-based laser synchronization.**

$J_M$  and  $J_S$ : free-running jitter of the master and the slave laser;  $J_O$ : relative jitter between the two lasers at the BOC input;  $H_{BOC}$ ,  $H_{BPD}$ ,  $H_{PI}$  and  $H_{PZT}$ : transfer functions of the BOC, BPD, PI controller and slave laser's PZT, respectively;  $E_{BOC}$  and  $E_{PI}$ : electronic noise of the BOC and the PI controller, respectively.

<sup>8</sup> 0.36 mV/fs measured with a BPD of  $2 \times 10^3$  V/A transimpedance gain and 1-MHz bandwidth.

Equation (3.5) indicates that there are three main contributions to the output jitter of the SH-BOC: free running timing jitters of the master and the slave lasers, and the electronic noise of the system. Since the master and the slave lasers are identical in our experiment:

$$\overline{J_O^2} = 2C_M\overline{J_M^2} + C_N\overline{J_N^2} \quad (3.6)$$

where  $C_M=|1/(1+H)|^2$  and  $C_N=|H/(1+H)|^2$ . Equation (3.6) implies that the measured timing jitter by the SH-BOC reads solely the timing jitter of the master laser if we let  $H \approx 0$ . Then  $C_M \approx 1$ ,  $C_N \approx 0$  and the upper limit to  $J_M$  is given by the half of the measured timing jitter at the BOC output:

$$\overline{J_M^2} \approx \frac{1}{2}\overline{J_O^2} - \frac{1}{2}C_N\overline{J_N^2} \leq \frac{1}{2}\overline{J_O^2} \quad (3.7)$$

Using the transfer functions of the setup elements in Appendix A.1 and the experimental parameters given in Table A.1, the effect of the BOC feedback loop on measured timing jitter is simulated for varying feedback gain values as shown in Figure 3.3. A practical way to make  $H \approx 0$  is to decrease the PI feedback gain parameter as much as possible. In this way, the locking bandwidth is decreased and the free-running timing jitter of the master laser (i.e., when  $C_M \approx 1$ ) is revealed also for smaller offset frequencies. This can be seen clearly from the simulated  $C_M$  coefficient in Figure 3.3(a), which gives 1 for all frequencies above 1 kHz when the feedback gain is decreased to -20 dB.

A fundamental noise contribution due to amplified spontaneous emission (ASE) inside the gain medium is always present in the output noise of mode-locked lasers even in the absence of technical noise sources such as acoustic vibrations, environment, and pump power fluctuations. A simple and intuitive way to understand the timing jitter related with ASE is to think of it as a white noise added to the instantaneous repetition rate [86]. In this case, phase noise spectral density is given by:

$$S_\varphi(f) = S_{f_R}(f)/f^2 \quad (3.8)$$

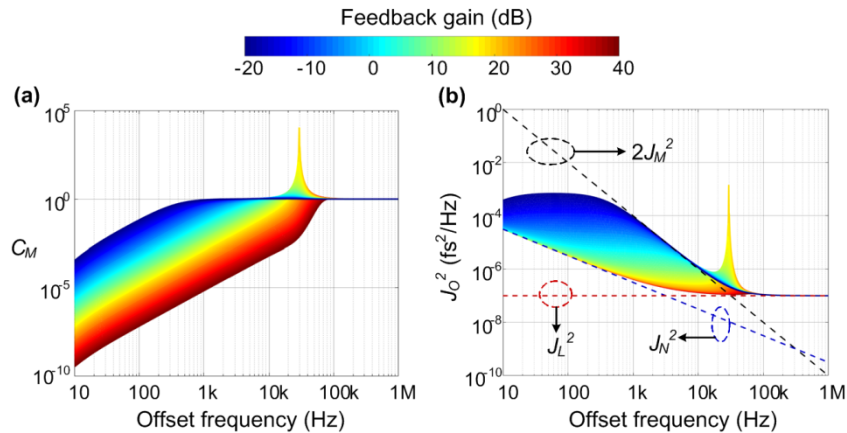


**Figure 3.3: Feedback simulations for the SH-BOC timing jitter measurement.** (a) Transfer coefficient  $C_M$  and (b) simulated SH-BOC output timing jitter spectral density at different feedback values. The peaks around 30 kHz originate from the PZT resonance of the slave laser. Figure is reproduced from our article [87].

where  $S_{f_R}$  is repetition rate power density and  $f$  is the offset frequency from the carrier. Equation (3.8) expresses that white noise in the repetition rate (e.g., ASE) has a characteristics of  $1/f^2$  in the phase noise (or in the timing jitter). In other words, noise sources with smaller frequencies will lead to larger accumulated timing jitter. Figure 3.3(b) shows the simulation results of the timing jitter spectral density  $J_o$  at different feedback values. In order to analyze how each noise source affects  $J_o$ , we assume that the free-running timing jitter of the master laser  $J_M$  exhibits a  $1/f^2$  slope regarding Equation (3.8), whereas the electronic noise  $J_N$  has common flicker noise characteristics with a  $1/f$  slope [88]. At high feedback gain, output timing jitter mainly conveys the electronic noise jitter from 10 Hz to 50 kHz and the laser's inherent jitter is totally obscured by the feedback loop. Once the feedback gain is gradually decreased from 40 dB to -20 dB, more and more low-frequency components of  $J_o^2$  coincide with  $2J_M^2$  and the accurate inherent timing jitter of the master laser is revealed at the output of the SH-BOC. Please note that above 50 kHz, the measurement is limited by  $J_L^2$  which is defined as the dominant noise floor at the input of the baseband analyzer<sup>9</sup>.

Figure 3.4(a) shows the timing jitter spectral density measured by the SH-BOC for varying feedback gain settings. As predicted by the simulation, a high feedback gain value leads to a large locking bandwidth which in turn prohibits the observation of the laser's inherent jitter for low offset frequencies. Therefore, the measured jitter spectral densities with gain values above 10 dB in Figure 3.4(a) correlate only with the other spectra for frequencies higher than 10 kHz. As the feedback gain is decreased, the locking bandwidth is reduced and the inherent jitter of the laser is revealed for offset frequencies below 1 kHz (see the spectra for 0-dB gain or lower). Due to the low timing jitter of the laser, the jitter spectral density above 30 kHz is obscured by the electronic noise floor of the

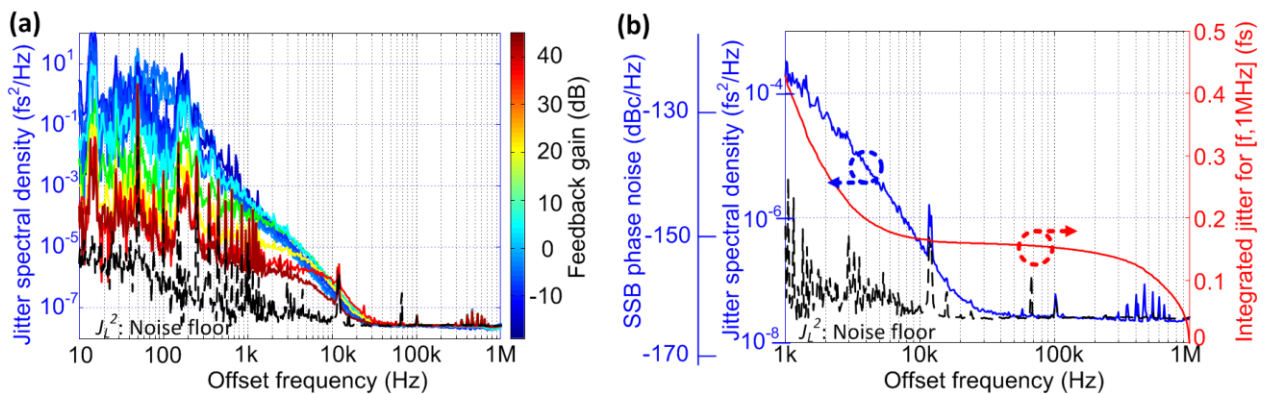


**Figure 3.4: Experimental results of the SH-BOC timing jitter measurement.**

(a) Timing jitter spectral density measured by the SH-BOC for varying feedback gain settings. (b) Free-running timing jitter of the master laser. Blue curve: timing jitter spectrum and single-sideband phase noise at 10 GHz carrier for -10 dB servo gain; red curve: integrated timing jitter. Figure is reproduced from our article [89].

<sup>9</sup>In this case, it was limited by the noise floor of the BPD.

system  $J_L^2$  (dashed black curve in Figure 3.4(a) and (b)). Figure 3.4(b) shows the free-running timing jitter of the master laser between 1 kHz and 1 MHz measured at -10-dB feedback gain.<sup>10</sup> Integration of the jitter spectral density yields an extremely low timing jitter of approximately 400 as for offset frequencies between 1 kHz and 1 MHz providing an upper limit estimate for the master laser's noise. Since the operational locking bandwidths in our applications are mostly higher than 10 kHz, the relevant frequency range for the integrated jitter is above 10 kHz where the master laser exhibits an integrated jitter of 170 as. However, the true value will be even lower since the laser jitter above 30 kHz is limited by the detection noise floor. If we assume that the master laser jitter is dominated by the ASE noise above this frequency, the jitter spectral density will follow a -20 dB/decade slope yielding an RMS jitter of only ~60 as integrated between 30 kHz and 1 MHz.

### 3.2 LONG-TERM FREQUENCY AND ENVIRONMENTAL STABILITY

Figure 3.5 compares the phase noise measurements of the master laser (blue curve, identical to the one in Figure 3.4(b)) and a conventional, low-noise microwave oscillator (red curve) at a 10-GHz carrier. Above 1-kHz offset frequency, the master laser possesses far lower phase noise decreasing down to -160 dBc at 30 kHz. In the low offset frequency range, however, the microwave oscillator shows a comparable and even slightly better performance, where the contribution of the technical noise sources to the timing jitter of the master laser becomes dominant. As the in-loop SH-BOC suppresses the inherent noise of the master laser for frequencies lower than the locking bandwidth, quantitative noise comparison between the two sources is not possible below 200 Hz.

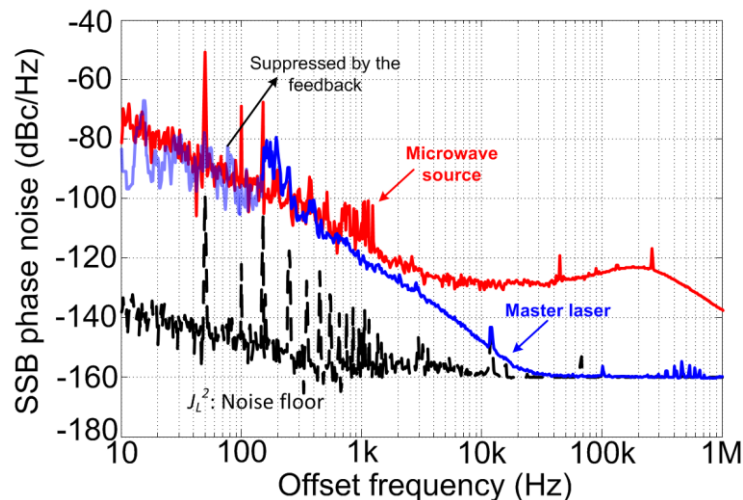


**Figure 3.5: Phase noise comparison of the master laser with a microwave source.**

Blue curve: SSB phase noise of the master laser, red curve: SSB phase noise of a microwave source (Agilent E8257D), black curve: measurement noise floor. All curves scaled at 10 GHz.

<sup>10</sup>3-dB locking bandwidth of the feedback loop is at ~ 200 Hz.

Nonetheless, it is intuitive to expect larger phase noise from the master laser when compared to the microwave oscillator for this low offset frequency range. This is indeed the case that the repetition rate of mode-locked lasers is highly influenced by acoustic vibrations and environmental fluctuations below 1 kHz resulting in integrated timing jitters in the picosecond range at 1 Hz [90].

As we have seen an example in Figure 3.5, mode-locked lasers provide an excellent short-term timing precision. However, they possess poor long-term stability due to thermal and acoustic effects contracting and expanding the laser cavity. Therefore, the effect of long-term frequency instabilities of the master laser on a timing distribution system is discussed in this section.

Precision of a timing distribution system can be assessed by measuring the relative drift between two independently stabilized fiber links which would require an experimental setup similar to the one given in Figure 3.6. The output of the master laser is split into two separate fiber links. Signal transmission delay of each link is stabilized with a timing detector (TD) measuring the timing fluctuations of the round-trip traveled pulses with respect to the new laser pulses and applies feedback control on a variable delay in the link. At the end station, an out-of-loop TD detects the relative timing error between the output pulse trains of the two fiber links. Suppose that every  $m^{\text{th}}$  pulse from the master laser and every  $(m-m_1)^{\text{th}}$  roundtrip traveled pulse meet with each other at TD1 in Figure 3.6 ( $m$  and  $m_1$  are integers). Then, the measured timing error by TD1 is:

$$\Delta t_{TD1} = m_1 T_R - \frac{2}{c} (d_{ref1} - L_1) \quad (3.9)$$

where  $T_R$  is the period of the pulse train emitted from the master laser,  $c$  is the speed of light in vacuum,  $d_{ref1}$  is the reference arm of the fiber link 1 (i.e., the distance from PBS1 to M1: |PBS1 M1|),

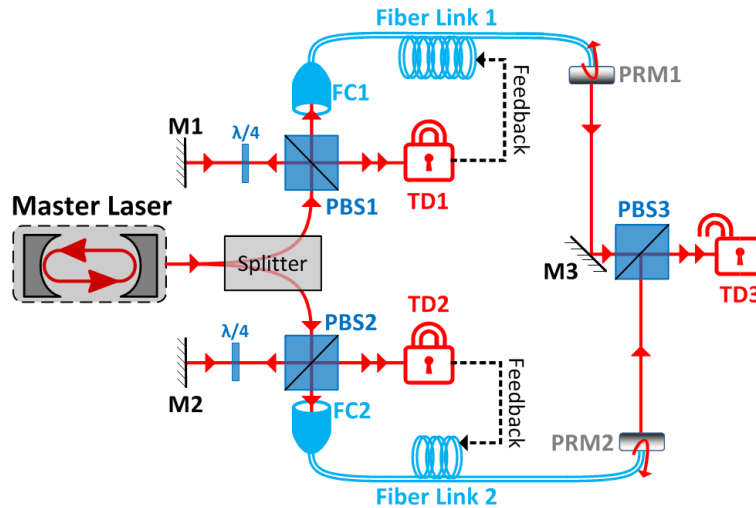


**Figure 3.6: A setup for measuring the precision of a timing distribution system.**

M: silver mirror; PBS: polarization beam splitter; FC: fiber coupler; TD: timing detector; PRM: partially reflecting mirror. TDs are symbolized with “lock symbols”. Closed lock refers to an in-loop detector, whereas open lock corresponds to an out-of-loop detector.

and  $L_1$  is the total link length from PBS1 to PRM1 (i.e.,  $L_1 = |\text{PBS1 FC1}| + n|\text{FC1 PRM1}|$  where  $n$  is the refractive index of the fiber). Similarly, every  $m^{\text{th}}$  pulse coincides with every  $(m-m_2)^{\text{th}}$  pulse ( $m_2$  is an integer) at TD2:

$$\Delta t_{TD2} = m_2 T_R - \frac{2}{c}(d_{ref2} - L_2) \quad (3.10)$$

where  $d_{ref2}$  is the reference arm of the fiber link 2 (i.e.,  $|\text{PBS2 M2}|$ ), and  $L_2$  is the total length from PBS2 to PRM2 (i.e.  $L_2 = |\text{PBS2 FC2}| + n|\text{FC2 PRM2}|$ ). Once the links are stabilized via TDs, the feedback loops keep the timing error of each link at zero, i.e.  $\Delta t_{TD1} = \Delta t_{TD2} = 0$ :

$$m_1 T_R = \frac{2}{c}(d_{ref1} - L_1) \quad (3.11)$$

$$m_2 T_R = \frac{2}{c}(d_{ref2} - L_2) \quad (3.12)$$

Then, one can observe the out-of-loop timing drift between the  $(m-m_3)^{\text{rd}}$  pulse from fiber link 1 and the  $(m-m_4)^{\text{th}}$  pulse from fiber link 2 using TD3 ( $m_3, m_4$  are integers). Suppose that at the beginning of the measurement, the out-of-loop TD3 is aligned so that its output shows zero timing error, i.e.,  $\Delta t_{out} = 0$ :

$$(m_3 - m_4)T_R = \frac{1}{c}[L_2 + d_{out2} - L_1 - d_{out1}] \quad (3.13)$$

where  $d_{out1}$  and  $d_{out2}$  are the out-of-loop paths of fiber link 1 and fiber link 2 respectively, i.e.,  $d_{out1} = |\text{PRM1 M3}| + |\text{M3 PBS3}|$  and  $d_{out2} = |\text{PRM2 PBS3}|$ . Then, if the repetition rate of the master laser changes, the period of the pulse train will shift by some amount  $\Delta T_R$  and the new period will be  $T_R + \Delta T_R$ . To keep the links stabilized, the in-loop detectors TD1 and TD2 will adjust the variable delays by  $\Delta L_1$  and  $\Delta L_2$  so that  $\Delta t_{TD1} = \Delta t_{TD2} = 0$ . Then, Equations (3.11) and (3.12) will give:

$$m_1(T_R + \Delta T_R) = \frac{2}{c}(d_{ref1} - L_1 - \Delta L_1) \quad (3.14)$$

$$m_2(T_R + \Delta T_R) = \frac{2}{c}(d_{ref2} - L_2 - \Delta L_2) \quad (3.15)$$

In this case, the out-of-loop detector will detect a timing error given by:

$$\Delta t_{out} = (m_3 - m_4)(T_R + \Delta T_R) - \frac{1}{c}[L_2 + \Delta L_2 + d_{out2} - L_1 - \Delta L_1 - d_{out1}] \quad (3.16)$$

Then by solving Equations (3.11) - (3.16) together, the detected timing error yields:

$$\Delta t_{out} = \frac{\Delta L_2}{(L_2 - d_{ref2})c}(d_{ref2} - d_{ref1} + d_{out2} - d_{out1}) \quad (3.17)$$

In the experiment, the total link length is in kilometer-scale, whereas the reference paths are in centimeter-scale, i.e.,  $L_2 \gg d_{ref2}$ . Furthermore, for a stabilized link the ratio of  $\Delta L/L$  must be equal to  $\Delta f_R/f_R$ , where  $\Delta f_R$  is the variation of the repetition rate. Therefore, the timing error observed between the two independently stabilized fiber links will be:

$$\Delta t_{out} = \frac{\Delta f_R (\Delta d_{ref} + \Delta d_{out})}{f_R c} \quad (3.18)$$

where  $\Delta d_{ref}$  and  $\Delta d_{out}$  are the uncompensated beam paths in the reference and out-of-loop arms respectively (i.e.,  $\Delta d_{ref} = d_{ref2} - d_{ref1}$  and  $\Delta d_{out} = d_{out2} - d_{out1}$ ). For a master laser operating at 200 MHz repetition rate, a pulse period drift of 1 ps (i.e.,  $\Delta T_R$ ) will result in a repetition rate shift of 40 kHz (i.e.,  $\Delta f_R \approx f_R^2 \Delta T_R$ ). Even if one can align and stabilize the length of uncompensated beam paths with 1-cm precision (i.e.,  $\Delta d_{ref} + \Delta d_{out} = 1$  cm), there will be still a timing error of  $\sim 7$  fs through Equation (3.18) due to 40 kHz fluctuation of the laser's repetition rate. Therefore, it is imperative to pay close attention to the long-term stability and environmental isolation of the master laser and uncompensated reference paths in the experimental setup.

To minimize environmentally induced timing fluctuations, an optical enclosure is built as shown in Figure 3.7. A super invar plate<sup>11</sup> with dimensions of 900 × 1200 × 4.8 mm is placed on top of a water-cooled breadboard, whose temperature is controlled by a cooling thermostat (Lauda RP 845C). All free-space optics are fixed on the invar sheet and the effective timing instability of reference beam paths due to thermal expansion is reduced to  $\pm 1$  as/cm with temperature fluctuations stabilized better than  $\pm 0.05$  K. A lead-foam is placed beneath the setup to damp table vibrations. The optical enclosure is built as two embedded layers to cut the air current in the laboratory and provide an efficient environmental stability for the inner optical components. Furthermore, the inner layer is covered with an acoustic heavy foil, whereas a humidity insulation material is used for the outer layer to protect the setup from environmental humidity variations.

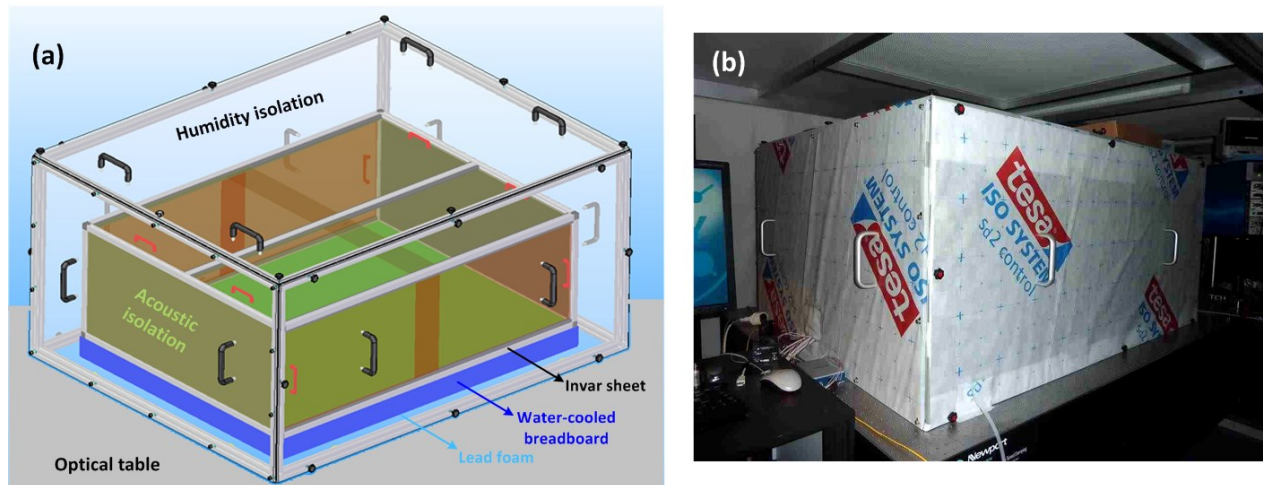


**Figure 3.7: Environmental insulation of the master laser and reference beam paths.**  
 (a) Sketch of the environmental isolation enclosure and (b) its photo as built in the lab.

<sup>11</sup>With a thermal expansion coefficient of only 0.63  $\mu\text{m}/\text{m}\cdot^\circ\text{C}$  for  $-55$  to  $+95$   $^\circ\text{C}$ .

To avoid long-term drifts due to cavity length fluctuations and improve the frequency stability of the master laser, the repetition rate is locked to a microwave oscillator (whose phase noise is presented in Figure 3.5) using a microwave PLL. However, one has to maintain a relatively low locking bandwidth here ( $\sim 100$  Hz), as can be seen in Figure 3.5 the master laser surpasses the microwave source in terms of low-noise performance for higher offset frequencies ( $>200$  Hz). Figure 3.8 shows the experimental readings of the master laser's repetition rate after locking to the microwave oscillator. The blue curve shows the electronic spectrum of the repetition rate at the 6<sup>th</sup> harmonic ( $\sim 1.3$  GHz), whereas the red curve reveals the tracking readings of the spectrum peak for 5 consecutive days. Total frequency drift at the 6<sup>th</sup> harmonic of the repetition rate is only 15 Hz which corresponds to a timing error of only 4 as due to Equation (3.18) and considering a total uncompensated beam path of 10 cm.

When these improvements in the long-term stability are combined with the ultralow laser jitter in high offset frequencies ( $>1$  kHz), the master laser is ready to serve in the development of a precise timing distribution.

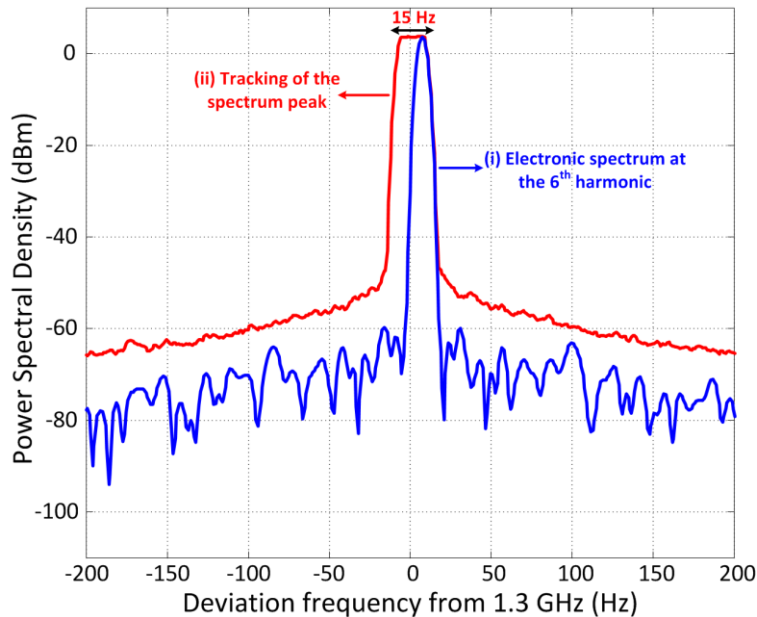


**Figure 3.8: Long-term repetition rate stability of the master laser.**

The measurement is performed at the 6<sup>th</sup> harmonic of the repetition rate for 5 days. X-axis is centered at 1.3 GHz and shows the deviation frequency from this value. Resolution bandwidth is 5 Hz.

## 4 NOISE-FREE FIBER LINK TRANSMISSION

Drift- and jitter-free distribution of pulsed optical signals is essential for the construction of a high precision timing system in order to preserve the low noise properties of the master laser during the delivery to remote locations. Fiber-optic links are the preeminent choice to efficiently deliver optical signals to remote locations. However, in an unstabilized link, environmental perturbations on the fiber (e.g., temperature, humidity, and mechanical stress) induce variations in the arrival time of the delivered optical pulses. In order to stabilize the transmission delay of the fiber links in the attosecond regime, first the round-trip timing error must be determined with high precision. As presented in Section 2.2, BOC is a highly sensitive method to measure timing fluctuations between optical pulses and it can be also employed to detect time of flight fluctuations of pulses circulating in a fiber link [57]. First demonstrations of timing-stabilized fiber links using BOCs were performed with standard single mode (SM) fibers and the results have showed substantial polarization-mode-dispersion limiting the system to a daily precision of  $\sim 10$  fs RMS [30,44,91]. To eliminate the polarization effects, our group in collaboration with OFS [92] has developed special polarization-maintaining (PM) fiber links with the ability to compensate 2<sup>nd</sup> and 3<sup>rd</sup> order dispersion [93]. This PM approach is further developed in this thesis to ensure drift-free fiber link transmission with attosecond precision.

### 4.1 GENERAL FIBER LINK STABILIZATION SCHEME

Figure 4.1 illustrates the operation principle of fiber link stabilization using a BOC to correct for time-of-flight fluctuations of the optical pulses. In this scheme, output pulse train of the master laser is divided into two parts: link-pulses and reference-pulses. Link-pulses are coupled into the fiber-based timing link (with km-scale length) and travel to the remote site. There is a partially-reflecting

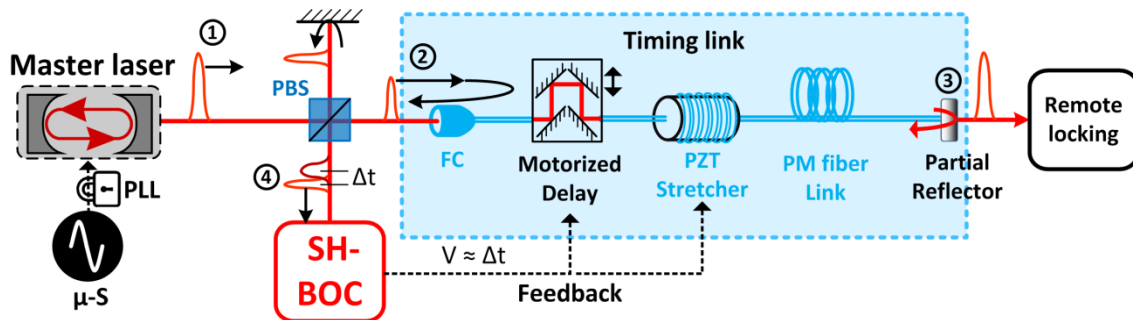


**Figure 4.1: Operation principle of fiber link stabilization using BOCs.**

$\mu$ -S: microwave source; PLL: phase-locked-loop; PBS: polarization beam splitter; FC: fiber-collimator; SH-BOC: second-harmonic BOC;  $\Delta t$ : time-of-flight fluctuations;  $V$ : SH-BOC voltage response. The blue box indicates the major elements of the timing link.

mirror at the end of the timing link, which reflects a certain fraction of the link-pulses back to the link input and transmits the remaining fraction to the link output for remote locking experiments. At the link input, the back-reflected link-pulses are overlapped spatially and temporally with the reference-pulses which are newly emitted from the master laser and travel only a small distance in free-space (few centimeters) to preserve their low-jitter properties. After recombination, the link- and reference-pulses are sent to a SH-BOC (presented in Section 2.2.1) which detects the relative timing jitter of the link-pulses induced by the environmental fluctuations on the timing link. Finally, the SH-BOC voltage response is applied by the locking electronics to a motorized delay stage and a PZT fiber stretcher as slow- and fast-feedback controls to correct for the detected timing jitter. Note that since these variable delay elements work in a bidirectional manner, the fundamental assumption of the fiber-link stabilization is that the timing errors acquired in the fiber link during the forward- and reverse-propagation are equal. This has two main consequences. First, fastest timing error which can be compensated is limited by the round-trip delay of the timing link. Environmental fluctuations on the fiber mainly include thermal expansion, temperature- and humidity-induced changes of the refractive index, mechanical stress and acoustic vibrations, out of which the vibrations act on the fastest time scale. However, even these periods are typically longer than a millisecond ( $<1$  kHz) and do not pose a severe limitation for the link stabilization as long as the fiber length is shorter than 100 km. Second consequence is that any asymmetrical fluctuation causing different timing errors on the forward- and reverse-propagation cannot be corrected by the round-trip error compensation scheme. For instance, nonlinear effects on the fiber link transmission can cause such effects when the peak power values of the pulses propagating on the forward- and reverse-direction are not equal which will be discussed thoroughly in Section 4.3.

## 4.2 EXPERIMENTAL RESULTS: TRADITIONAL FEEDBACK

In this section, results of various timing-link stabilization experiments using the traditional feedback scheme will be discussed and its limitations will be investigated.

### 4.2.1 FIBER LINK STABILIZATION WITH FREE-SPACE BOCs

The general principle and implementation of the fiber link stabilization using BOCs with free-space optics has been already demonstrated by our former group members [30,57,93]. Nonetheless, it is a valuable practice to repeat these experiments in order to gain practical insight in the system and analyze its limitations for further development. Therefore, the first experimental results achieved during my PhD studies are from the stabilization of a 3.5-km PM dispersion-compensated fiber link using free-space optics. Figure 4.2 shows the internal elements of the fiber link consisting of three different fiber types. The largest section is made of a standard PM 1550 panda-style fiber

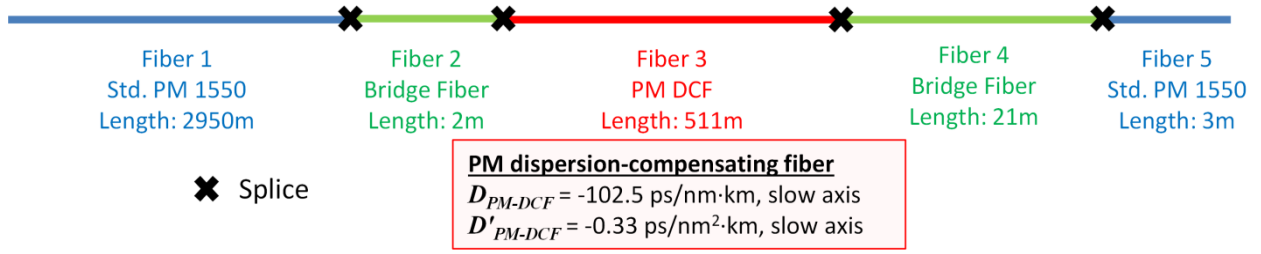


**Figure 4.2: Schematic of the 3.5-km fiber link.**

$D_{PM-DCF}$ : dispersion parameter and  $D'_{PM-DCF}$ : dispersion slope (i.e.,  $\frac{dD}{d\lambda}$ ) of the PM-DCF.

(OFS TruePhase™ 1550) with a total length of 2950 m. To compensate for the negative dispersion introduced by the standard PM fiber, 511-m of a custom PM dispersion compensating fiber (PM-DCF) is developed and fabricated in collaboration with OFS laboratories. The PM-DCF also exhibits a panda-style geometry with a measured birefringence of  $2.9 \times 10^{-4}$ , 0.4-dB/km attenuation and 1520-nm cutoff wavelength. To minimize losses due to the small mode-size of the PM-DCF ( $A_{\text{eff}} = 22 \mu\text{m}^2$ ), an intermediate bridge fiber (PM Raman type) is spliced between the standard PM fiber and the PM-DCF. The dispersion and dispersion slope are  $-102.5 \text{ ps}/(\text{nm}\cdot\text{km})$  and  $-0.33 \text{ ps}/(\text{nm}^2\cdot\text{km})$  respectively, for the slow axis at 1550 nm, providing compensation of not only for the second-order (SOD, i.e., group velocity dispersion) but also for the third-order dispersion (TOD) of the standard PM fiber. Ratios of the dispersion coefficients between the two fiber types are:

$$\frac{\beta_{2,PM-DCF}}{\beta_{2,Std-PM}} = -5.663 \quad (4.1)$$

$$\frac{\beta_{3,PM-DCF}}{\beta_{3,Std-PM}} = -5.613$$

$\beta_{2,Std-PM}$  and  $\beta_{3,Std-PM}$  are the SOD and TOD coefficients of the standard PM fiber, whereas  $\beta_{2,PM-DCF}$  and  $\beta_{3,PM-DCF}$  are the SOD and TOD coefficients of the PM-DCF. Due to this ratio difference, it is not possible to achieve perfect compensation for SOD and TOD simultaneously. For instance, if the SOD of the 3.5-km fiber is eliminated, 26-m worth of TOD from the standard PM fiber will remain uncompensated. An optical auto-correlator is used to confirm the temporal duration of the link pulses. Due to the residual TOD, a pulse duration of  $\sim 400 \text{ fs}$  is measured at the end of the 3.5-km fiber link.

The experimental setup for fiber link stabilization using free-space BOCs is shown Figure 4.3. The master laser is a commercially available mode-locked laser (Origami 15 from One-Five GmbH) whose low-noise properties are presented in Section 3.1. In order to avoid long-term frequency drifts, the repetition rate of the master laser is locked to a microwave source (Agilent E8257D) with  $\sim 100\text{-Hz}$  locking bandwidth (for details refer to Section 3.2). Such a low-frequency bandwidth is easily achieved with a simple microwave PLL as described in Figure 4.3(b). Output of the master laser is divided into two parts by the first polarization beam splitter (PBS1): the first part goes to



BOC1. Due to some splicing errors, the polarization extinction ratio of the complete PM fiber is only 16.7 dB. To improve this ratio, a linear polarizer is placed at the input of the fiber link.

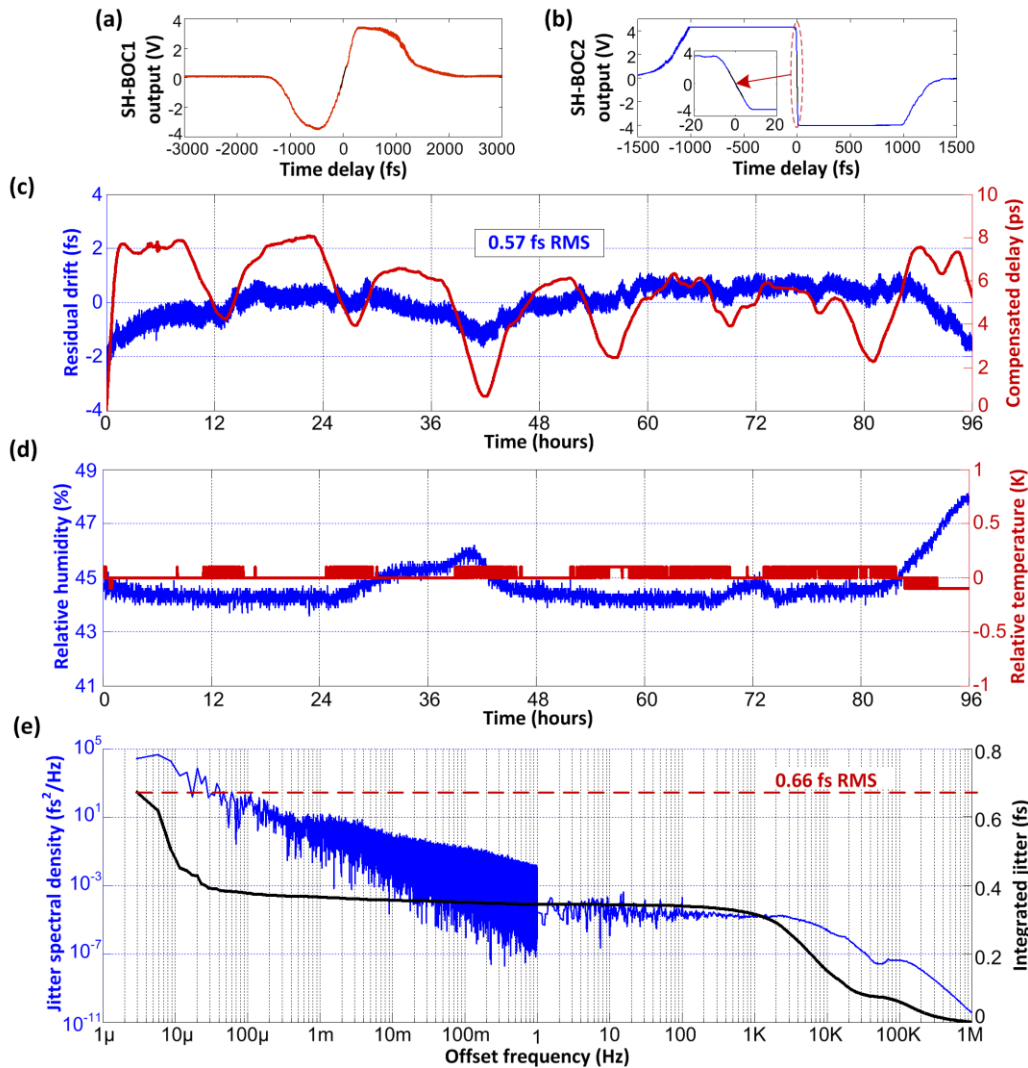
Power management of the fiber link is critical: high link output power is desirable for high signal-to-noise ratio, while low link operating power is needed to avoid fiber nonlinearity-induced timing errors. As a precaution, the fiber link is operated with a maximum average power of +13 dBm to avoid significant fiber nonlinearities. The input power to the fiber link is set to +8 dBm such that after forward propagation, the link transmission losses result in +0-dBm link power. The custom-built bidirectional EDFA is then used in the last section of the timing link to boost the link output power to +13 dBm. +3 dBm is reflected back by the partially reflecting mirror (with 10% back reflection) and reamplified by the EDFA back to +13 dBm. Finally, the back-propagated pulses are combined with new laser pulses in SH-BOC1 at the link input to perform the link stabilization.

Figure 4.3(c) shows the traditional feedback system employed for the link delay stabilization. First, the BOC error signal is processed by a PI controller whose output is divided into two paths. The first path is amplified by a high voltage amplifier (Menlo Systems, HVA 150) to control a PM fiber stretcher (Optiphase PZ3) with a sensitivity of 6.4 fs/V and resonance frequency of 16 kHz. The fiber stretcher is responsible for compensating the fast timing jitter of the link and permits a locking bandwidth around 2 kHz. The second path is sampled by a data acquisition card (DAQ) so that when the PI controller reaches its output voltage limit, the motorized-delay (General Photonics MDL-002) is activated through a home-developed Labview program serving as the slow compensation to the fluctuating link delay. The motorized delay has a tuning range of 560 ps that can counteract a thermal expansion of 5.5 K average temperature fluctuation in a 3.5-km fiber link.

To evaluate the performance of the link stabilization experiment, output pulse train from the link and fresh laser pulses in the out-of-loop section (traveling only the distance of  $\sim 10$  cm from PBS1 to PBS3 in Figure 4.3(a)) are combined in the free-running SH-BOC2. Once the feedback system is engaged to stabilize the timing link, SH-BOC2 output is used for the data acquisition of the out-of-loop measurements as shown in Figure 4.3(d). First, the timing sensitivities of the two SH-BOCs are measured. For +16 dBm average power from the reference path and +2 dBm average power returning from the link, the timing sensitivity of the in-loop SH-BOC1 is 14 mV/fs (see Figure 4.4(a)) measured with a BPD transimpedance gain of  $2 \times 10^6$  V/A and a bandwidth of 150 kHz. With +11-dBm average power from the link output and +19-dBm reference power, the response of the out-of-loop SH-BOC1 curve is also measured with the same BPD settings as shown in Figure 4.4(b). A higher timing sensitivity of 500 mV/fs is achieved due to the higher input power for both arms.

In order to measure the long-term residual drift of the link delay, the out-of-loop SH-BOC voltage is first filtered by a 1-Hz low pass filter, and then recorded by a DAQ card with 2-Hz sampling rate to

avoid aliasing (see Figure 4.3(d)). Link stabilization for 96 h is achieved without interruption. The recorded data for the residual drift and the compensated link delay are shown in Figure 4.4(c). The remaining timing drift at the link output has a maximum deviation of about 3 fs and an RMS value of 0.57 fs, which is comparable to the former results achieved for the 1.2-km PM link [93]. In the meantime, the motorized delay compensates for 8-ps variation in the link length. During the course of the measurement, the temperature in the laboratory has a maximum deviation of 0.2 K (red curve in Figure 4.4(d)), whereas the relative humidity has a fluctuation of 4% during the 4-day measurement (blue curve in Figure 4.4(d)). From Figure 4.4(c) and (d), it can be seen that residual



**Figure 4.4: Experimental results of the fiber link stabilization with free-space BOCs.**

(a) In-loop SH-BOC1 response versus the time delay between the input pulses. (b) Out-of-loop SH-BOC2 response. (c) Residual timing drift measured by the out-of-loop SH-BOC2 (blue curve) and corrected link delay by the motorized delay (red curve). (d) Relative humidity (blue curve) and temperature change (red curve) in the laboratory. (e) Timing jitter spectral density from 3  $\mu$ Hz to 1 MHz (blue curve) and its corresponding integrated timing jitter (black curve).

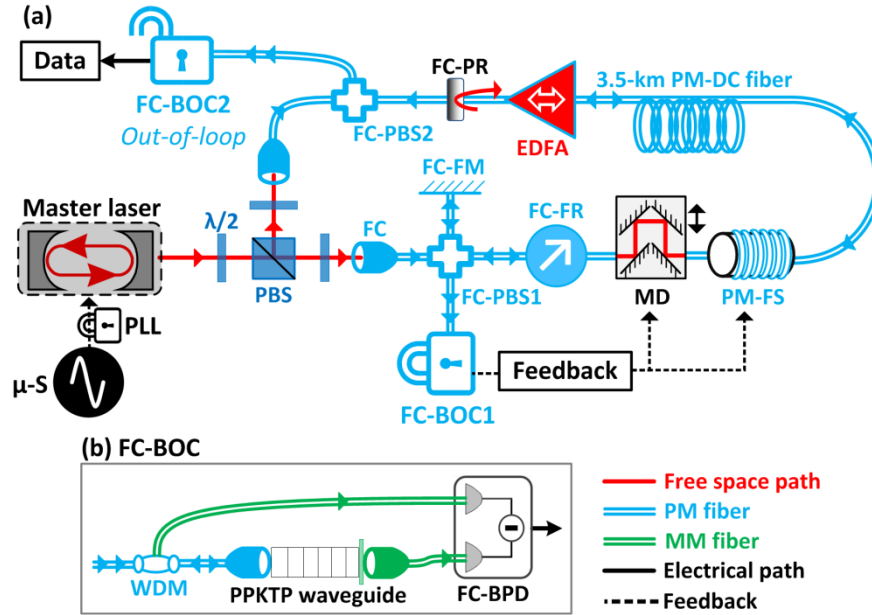
link drift is partially correlated with the relative humidity. Since the reflection ratio of the coating at the end of the PPKTP crystal is dependent on the humidity, any humidity fluctuation introduces a timing error during the BOC detection. Therefore, the outer layer of the optical enclosure is covered with a humidity insulation foil as described in Section 3.2 for the subsequent experiments.

Figure 4.4(e) illustrates the timing jitter spectral density of the complete out-of-loop measurements between 3  $\mu\text{Hz}$  and 1 MHz. The spectrum below 1 Hz is simply the Fourier transformation of the residual drift data in Figure 4.4(c), whereas the spectrum for offset frequencies larger than 1 Hz is measured with a baseband analyzer (Agilent E5052B) which Fourier transforms the out-of-loop SH-BOC2 output. Total integrated timing jitter of the fiber link is 0.66 fs RMS. As can be seen from the black curve in Figure 4.4(e), the link stabilization experience almost no noise between 1 kHz and 20  $\mu\text{Hz}$  (i.e.,  $\sim 12$  h). Therefore, the largest contributions to the link timing jitter come from the day and night environmental fluctuations (below 20  $\mu\text{Hz}$ ) in the laboratory and the inherent timing jitter of the master laser (above 2 kHz) which is transferred to the out-of-loop by the feedback loop (for detailed explanation refer to Section 4.3.4).

#### 4.2.2 FIBER LINK STABILIZATION WITH FIBER-COUPLED BOCs

Timing distribution systems employed in operational FEL facilities need fiber networks consisting of 25 or more timing links which require tremendous attention to the alignment and stability of the free-space optics to minimize timing-drifts induced by beam pointing instabilities. This situation also necessitates pre-amplification of the master laser's output to overcome excessive free-space to fiber coupling losses to provide adequate power for all timing links. To eliminate free-space optics and its disadvantages from the timing distribution system, we demonstrate for the first time an all fiber implementation of timing link stabilization using fiber-coupled BOCs (FC-BOC, presented in Section 2.2.2).

A diagram of the experimental setup is shown in Figure 4.5. The only free-space components used in this experiment are the initial power separation elements comprised of a PBS and three half-wave plates. After the PBS, output of the master laser is coupled into two separate fiber paths: out-of-loop reference path and link stabilization section. The out-of-loop reference path is a 1-m long PM fiber serving as the reference arm for the out-of-loop FC-BOC2. The link stabilization section starts with a FC-PBS1 that divides the optical power further into two segments. The first segment (traveling to the right through FC-PBS1 in Figure 4.5(a)) is directed into the timing link which is identical to the one in Figure 4.3 except here we use a fiber-coupled Faraday rotator to guide the link-pulses into in-loop detector upon roundtrip propagation. The second segment is sent into a 0.5-m fiber having a fiber-coupled Faraday mirror at the end which turns the polarization of the pulses by  $90^\circ$  upon reflection and sends them into the in-loop FC-BOC1 to serve as the reference pulses for



**Figure 4.5: Experimental setup for all-fiber-coupled timing link stabilization.**

(a) Main schematic of the experiment. (b) Elements of the FC-BOCs.  $\mu$ -S: microwave source, PLL: phase-locked-loop, PBS: polarization beam splitter,  $\lambda/2$ : half-wave plate, FC: fiber-collimator; FC-PBS: fiber-coupled polarization beam splitter; FC-FM: FC Faraday mirror; FC-FR: FC Faraday rotator; MD: motorized delay; PM-FS: PM fiber stretcher; EDFA: PM erbium doped fiber amplifier; FC-PR: FC partial reflector; WDM: wavelength division multiplexer; MM fiber: multi-mode fiber; FC-BPD: fiber-coupled BPD.

the timing stabilization of the 3.5-km link. Both of the FC-BOCs employed in this experiment are based on PPKTP waveguide chips in fiber-coupled packages with internal temperature control as described in Section 2.2.2 [77]. A schematic of the module is shown in Figure 4.5(b). WDM serves a fiber-coupled dichroic beam-splitter that couples the input pulses into the waveguide for cross-correlation and separates the second-harmonics from the fundamentals. The second-harmonic signals are then fed to the ports of a fiber-coupled BPD. Link timing errors detected by the in-loop FC-BOC1 are applied to the fiber stretcher and to the motorized stage using the same feedback mechanism as described in Figure 4.3(c). Once the link stabilization loop is activated, the output of the fiber-coupled partial reflector and the out-of-loop reference fiber are combined in FC-PBS2 and coupled into the free-running FC-BOC2 to evaluate the performance of the link stabilization experiment. In order to minimize the drifts coming from the length fluctuations in the FC-BOC reference paths, all setup elements are placed in a temperature-stabilized optical enclosure, except the 3.5-km fiber link spool which is put outside and exposed to environmental fluctuations in the laboratory. Furthermore, outer layer of the optical enclosure is covered with a humidity insulation foil to suppress the humidity effects on the BOC detection.

Measured voltage responses of the FC-BOCs against the time delay between the incoming orthogonal pulses are given in Figure 4.6(a). Due to the spatial mode mismatch between the input

PM fiber and the waveguide, second-harmonic light collected on the reverse path is approximately 10 dB lower than that of the forward path in FC-BOCs. Therefore, a 10-dB attenuator is inserted in the forward path to symmetrize the cross-correlation curve. This issue prevents the FC-BOCs from reaching higher timing sensitivities when compared with bulk-optics BOCs. Nevertheless, the FC-BOCs demonstrate comparable performance to the previous work with free-space optics even with

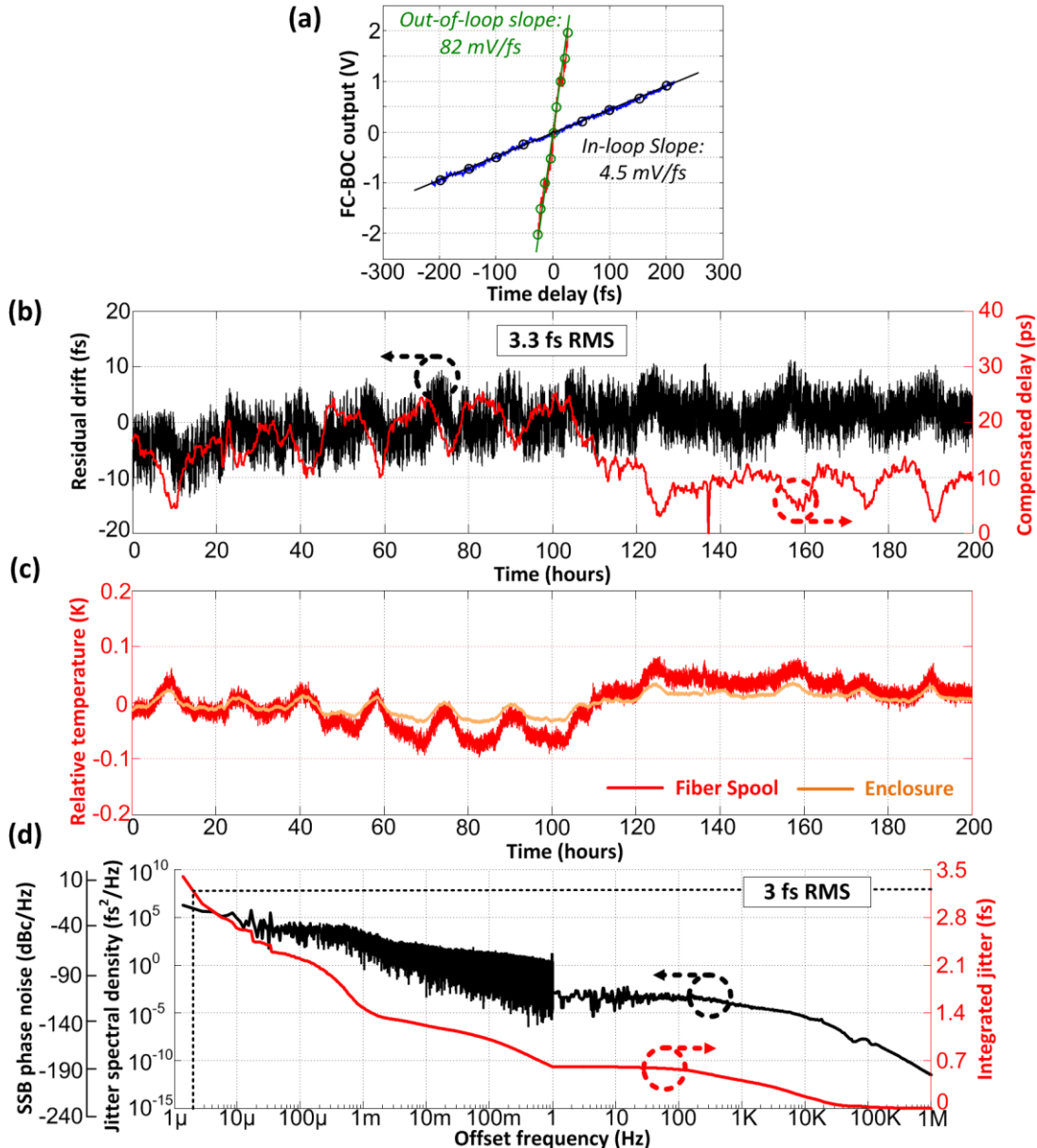


**Figure 4.6: Experimental results of all-fiber-coupled timing link stabilization.**

(a) FC-BOC output versus the delay between the pulses. Blue curve corresponds to the in-loop and red curve corresponds to the out-of-loop FC-BOC response. (b) Residual timing drift measured by the out-of-loop FC-BOC2 (black curve) and corrected link propagation delay (red curve). (c) Relative temperature change during the measurement. (d) Timing jitter spectral density and single-sideband phase noise scaled at 10 GHz carrier (black curve) and its integrated timing jitter (red curve). This figure is reproduced from our article [89].

the current coupling losses. For each FC-BOC, five different measurements are performed and the mean values of the timing sensitivities are 4.5 mV/fs ( $\pm 0.32$  mV/fs) and 82.0 mV/fs ( $\pm 4.9$  mV/fs) for the in-loop and out-of-loop FC-BOC, respectively (BPD transimpedance gain:  $2 \times 10^6$  V/A, bandwidth: 150 kHz, and responsivity: 0.5 A/W).

Relative timing stability of the 3.5-km PM fiber link is monitored continuously for 200 h. Black curve in Figure 4.6(b) shows the residual timing drift measured by low-pass filtering the output of FC-BOC2 at 1 Hz. A remaining drift of only 3.3 fs RMS is measured for 200 h of continuous link stabilization, and the motorized delay has corrected for over 25-ps timing error (red curve in Figure 4.6(b)). Relative temperature fluctuations of the 3.5-km PM fiber spool and the optical enclosure are plotted in Figure 4.6(c). Maximum deviation of the temperature is about 0.18 K and 0.06 K on the case of the fiber spool and inside the enclosure, respectively. The observed environmental stability of our laboratory is similar to targeted temperature stability of the tunnel in the European XFEL (largest FEL facility in the world) which is less than 1-K change per day [94]. Hence, our setup can easily counteract such an environmental instability as it can withstand  $\sim 5.5$  K average temperature fluctuation for a 3.5-km fiber link limited by the range of the motorized delay. The main drawback of the fiber-coupled system when compared to the free-space system is that the uncompensated fiber reference arms are much more sensitive to the environmental fluctuations (e.g., temperature, humidity, acoustic vibrations, mechanical stress, etc.). As can be seen in Figure 4.6(b) and (c), the correlation between the residual drift and the enclosure temperature confirms that the drift is mainly limited by the environmental fluctuations penetrating into the FC-BOCs. The optical enclosure is large in volume, making it difficult to isolate the enclosed fibers completely from the laboratory environment. Even though we have spent considerable effort to splice as short fiber reference arms as possible, the system still contains in total  $\sim 2.5$  m of uncompensated fiber (reference arms of the FC-BOCs and the fiber pigtail between FC-PR and FC-PBS2 in Figure 4.5(a)). A temperature fluctuation of 0.1 K on a 2.5-m uncompensated fiber would introduce approximately 5-fs error to the timing detection due to thermal expansion and contribute directly to the final drift. Hence, the observed residual drift in our experiment agrees well with the recorded relative temperature change.

Timing jitter spectral density of the link stabilization and its integrated jitter for the complete measurement range are given in Figure 4.6(d) (black and red curves, respectively). The spectrum from 1 Hz up to 1 MHz is measured with a baseband spectrum analyzer from the out-of-loop FC-BOC2, whereas the spectrum below 1 Hz is obtained by taking the Fourier transformation of the residual drift data shown in Figure 4.6 (b). Total timing jitter above 1 Hz is kept below 0.7 fs RMS. Unlike the free-space link-stabilization where there is almost no detected noise between 1 kHz and

20  $\mu\text{Hz}$ , sub-fs stability cannot be maintained with the fiber-coupled system for frequencies below 1 Hz where environmental fluctuations cause considerable jitter. Nevertheless, a phase noise of only -20 dBc/Hz at an offset frequency of 2  $\mu\text{Hz}$  from a 10-GHz carrier is achieved and the total integrated jitter from 2  $\mu\text{Hz}$  up to 1 MHz is only 3 fs RMS.

#### 4.2.3 TIMING TRANSFER OVER A MULTI-KM FIBER LINK NETWORK

Relevant precision of an operational timing distribution system is determined rather by the relative instability between the remote slave optical and microwave oscillators that are synchronized to the master laser by a timing network consisting of many fiber links. Therefore, it is essential to evaluate the out-of-loop performance of such a fiber network by performing a heterodyne measurement between two independently stabilized fiber links. Figure 4.7 shows the schematic of our fiber-link network experiment consisting of two independently stabilized fiber links with a total length of 4.7 km. This time, the output of the master laser is split into two separate timing links. Timing link 1 is the one with 3.5-km length used in Sections 4.2.1 and 4.2.2, whereas timing link 2 comprises of a 1.2-km PM dispersion-compensated fiber spool, a PM fiber stretcher, and a free-space motorized stage with 100-ps range. The stabilization of each timing link is done by a free-space SH-BOC due to its superior long-term stability when compared with FC-BOCs. All free space optics are mounted on a temperature-stabilized invar board, whereas the fiber spools are placed on opposing sides of the optical table and exposed to environmental fluctuations in the laboratory. SH-BOC1 and SH-BOC2 are the in-loop timing detectors stabilizing the timing links using the same feedback system described in Figure 4.3(c). At the remote end of the timing links, a free-running detector (SH-BOC3) is built to evaluate the timing stability of the fiber network.

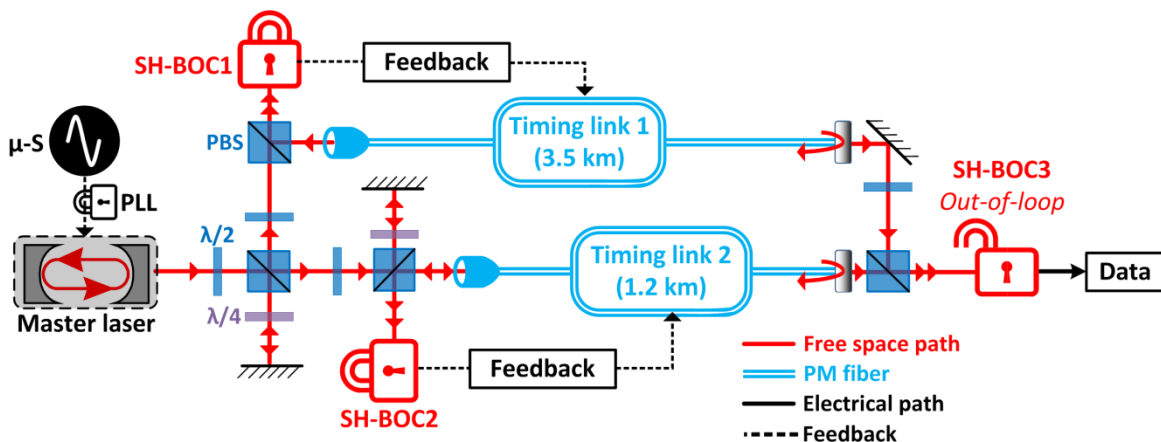


**Figure 4.7: Experimental setup for fiber-link network stabilization.**

$\mu\text{-S}$ : microwave source; PLL: phase-locked-loop; PBS: polarization beam splitter;  $\lambda/2$ : half-wave plate;  $\lambda/4$ : half-wave plate; SH-BOC: second-harmonic BOC. Feedback and data acquisition systems are identical to the ones in Figure 4.3. BOCs are symbolized with “lock symbols”. Closed lock is an in-loop detector, whereas open lock is an out-of-loop detector.

Figure 4.8(a) displays the residual timing drift (below 1 Hz) between the two link outputs measured by the out-of-loop detector. Even though the two timing links experience different environmental conditions (see the blue and red curves in Figure 4.8(b)), the fiber link network maintains a timing instability of 0.7 fs RMS for 14 h of measurement. The orange curve in Figure 4.8(b) shows the temperature readings inside the enclosure with a maximum deviation of only 0.05 K. This corresponds to a much lower value when compared to the temperature outside of the enclosure experienced by the links ( $\sim 0.25$  K) and ensures the environmental stability of the uncompensated beam paths of the reference arms.

Although our link stabilization experiments using free-space BOCs show consistently sub-fs residual timing drift over several days (see Figure 4.4(c) and Figure 4.8(a)), there are still quite apparent long-term fluctuations of an unidentified source. One noticeable correlation is the environmental instability (i.e., humidity and temperature). Hence, first implementations of fiber link stabilization have stated that the residual drift arises from the fluctuations of the reference paths due to environmental instability [30,57,95]. However, we still observe noticeable drift patterns even with reference path lengths of few centimeters having 0.05-K temperature instability. Furthermore, this correlation is quite vague in our fiber network results in Figure 4.8 where the temperature readings inside the enclosure show almost no correspondence to the residual drift.

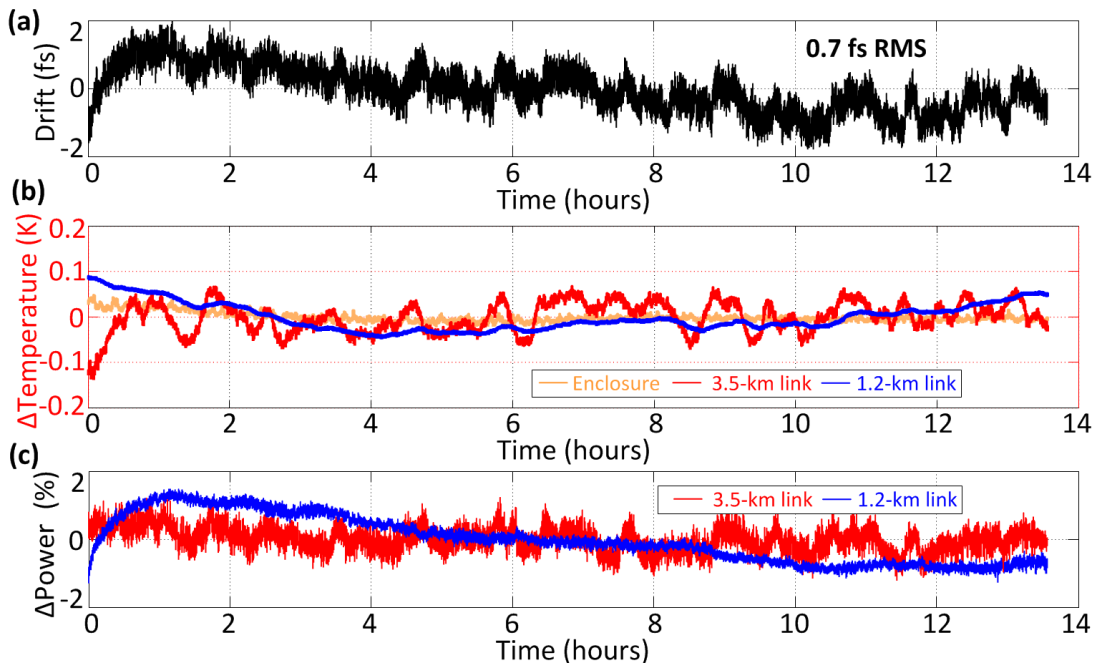


**Figure 4.8: Experimental results of the fiber-link network stabilization.**

(a) Residual timing drift between the timing links measured by SH-BOC3. (b) Temperature change ( $\Delta$  Temperature) of the enclosure and the timing links during the measurement. (c) Power fluctuations ( $\Delta$  Power) of the timing links measured at the link outputs.

After thoroughly investigating the effects of individual setup elements, we have identified the source of the remaining timing drift as the operational power fluctuations of the timing links. Figure 4.8(c) illustrates the measured output powers of both timing links which show a clear correlation with the measured residual drift for the complete duration of measurement. For instance, the output power of the 1.2-km link has a smooth variation exhibiting a step increase in the 1<sup>st</sup> hour and a slow fall for the remaining duration which defines the main trend of the observed residual drift. On the other hand, the 3.5-km link shows rather fast power fluctuations (below 1-hour period) over a certain mean value which portrays the spiky structure of the residual drift beneath its long-term smooth variation.

There are two main elements causing the operational link power to fluctuate. First, long-range correction of a timing link is performed by a motorized stage with long delay arms; e.g., a 10-cm range is required to correct for  $\pm 1.5$ -K temperature change in a 3.5-km link. Movement of the motorized delay introduces inevitable beam misalignments that cause power fluctuations coupling into the link. We measure the coupled power change of our delay stages when their delay position is

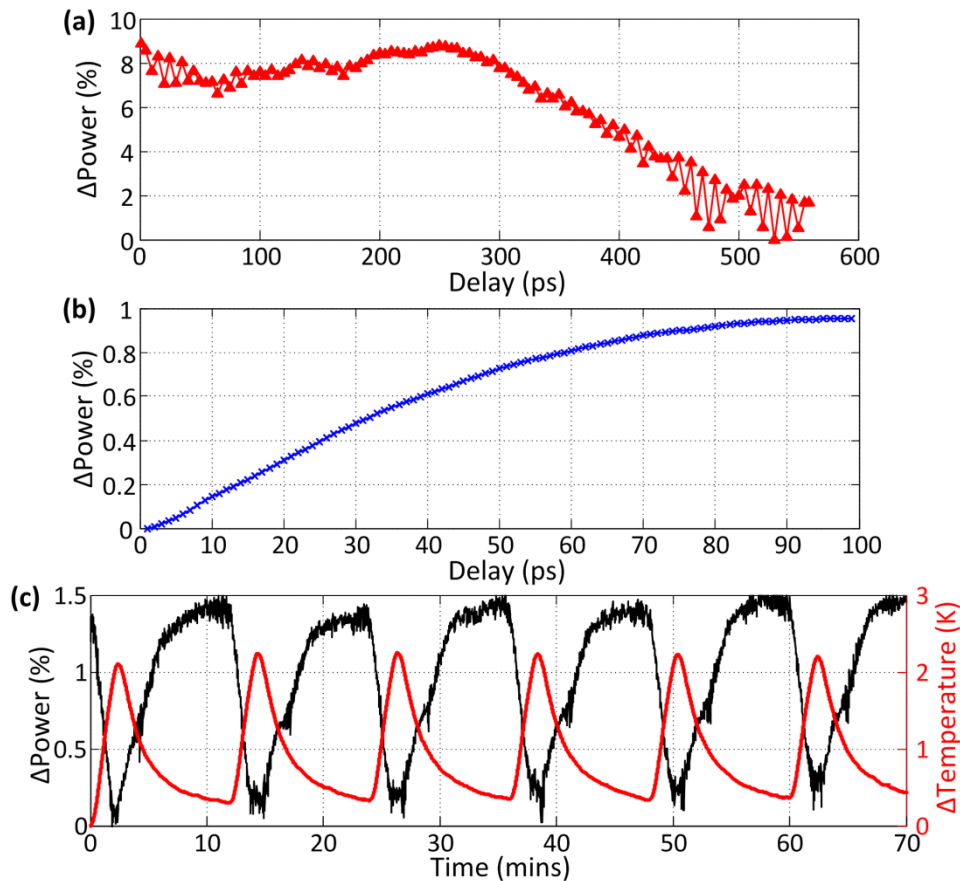


**Figure 4.9: Setup elements causing the link power fluctuations.**

Coupled power variation of the motorized delays in (a) timing link 1 and (b) timing link 2 vs. their delay position. (c) Output power dependence of the EDFA against the temperature.

scanned through the complete range. The motorized delay used in timing link 1 is a commercially available product (General Photonics MDL-002) and reveals an overall power fluctuation of 10% (see Figure 4.9(a)). Realizing this poor performance of the commercial products, we have constructed a motorized delay by mounting a retro-reflecting mirror on a linear positioning stage with 50-nm precision (PI M-111). By carefully aligning the mirror and the fiber collimator, we are able to decrease the coupled power fluctuations of timing link 2 to less than 1% as shown in Figure 4.9(b). Second element causing major power fluctuations is the EDFA positioned at the end of the timing link. Even though the drivers providing the energy source for the EDFAs have internal feedback loops to stabilize their pump currents, the amplification ratio of the gain medium is dependent on the temperature. We observe a relative power variation of  $\sim 1.5\%$  at the output of the EDFA for a temperature variation of 2 K as shown in Figure 4.9(c).

### 4.3 FIBER LINK INDUCED TIMING ERRORS

Now that the source of the residual timing drift has been identified, we can try to remove it from our system. The most straightforward solution would be the stabilization and isolation of the timing links and EDFAs. However, this is not feasible in practice due to the size of the operational facilities and there will be always some residual environmental fluctuations similar to the case in Figure 4.8(b). Therefore, a more scientific approach would be to investigate the physical mechanism between the power fluctuations and the timing jitter of the pulses traveling inside the fiber links.

#### 4.3.1 BOC RESPONSE TO TEMPORAL PULSE PROFILE DISTORTIONS

First of all, it is vital to comprehend the detection mechanism of the BOC in detail when stabilizing a fiber-based timing link. Suppose that  $E_1$  and  $E_2$  are the electric fields of the link-pulses and reference pulses, respectively launched into the BOC to detect their relative timing and  $E_3$  is the electric field of the sum-frequency pulse in the retarded time frame of  $E_3$ . Then, the sum-frequency generation in a BOC can be determined by the coupled wave equations with undepleted-fundamental-frequency approximation [96]:

$$\left[ \frac{\partial}{\partial z} + \left( \frac{1}{v_1} - \frac{1}{v_3} \right) \frac{\partial}{\partial t} \right] E_1 = 0 \quad (4.2)$$

$$\left[ \frac{\partial}{\partial z} + \left( \frac{1}{v_2} - \frac{1}{v_3} \right) \frac{\partial}{\partial t} \right] E_2 = 0 \quad (4.3)$$

$$\frac{\partial}{\partial z} E_3 = i \frac{d_{eff} \omega_3}{n_3 c} E_1 E_2 \quad (4.4)$$

where  $v_i$  denote the group velocities of the electric fields  $E_i$  ( $i=1, 2, 3$ ),  $d_{eff}$  is the nonlinear optical coefficient,  $\omega_3$  is the carrier angular frequency of  $E_3$ ,  $n_3$  is the refractive index of  $E_3$  in the nonlinear crystal, and  $c$  is the speed of light in vacuum. By solving these three equations,  $E_3$  becomes:

$$E_3(t) = K \int_0^{L_C} E_1(t - k_1 z) E_2(t - k_2 z) dz \quad (4.5)$$

where  $L_C$  is the crystal length and

$$K = i \frac{d_{eff} \omega_3}{n_3 c} \quad (4.6)$$

$$k_1 = \frac{1}{v_1} - \frac{1}{v_3} \quad (4.7)$$

$$k_2 = \frac{1}{v_2} - \frac{1}{v_3} \quad (4.8)$$

If there is an initial delay  $T_D$  between  $E_1$  and  $E_2$ , and  $L_C$  is sufficiently long, Equation (4.5) can be approximated as:

$$E_3(t, T_D) = K \int_0^{\infty} E_1(t - k_1 z) E_2(t - k_2 z - T_D) dz \quad (4.9)$$

Since the optical pulses in the reference path are very short ( $\sim 150$  fs), they can be approximated by Dirac delta functions. Therefore,  $E_3$  is simplified as:

$$E_3(t, T_D) = \begin{cases} K E_1\left(t - k_1 \frac{t - T_D}{k_2}\right), & t > T_D \\ 0, & \text{else} \end{cases} \quad (4.10)$$

The optical power of the sum-frequency generated on the forward pass  $P_F$  is:

$$P_F(T_D) = \int_{-\infty}^{+\infty} |E_3(t, T_D)|^2 dt \quad (4.11)$$

$$P_F(T_D) = |K|^2 \frac{k_2 - k_1}{k_2} \int_{T_D}^{\infty} |E_1(t)|^2 dt \quad (4.12)$$

In first-order linear approximation, Equation (4.12) is simplified as:

$$P_F(T_D) = \begin{cases} |K|^2 \frac{k_2 - k_1}{k_2} E, & T_D < T_{D0} - \frac{1}{2} T_{BOC} \\ |K|^2 \frac{k_2 - k_1}{k_2} \frac{E}{T_{BOC}} \left(T_D - T_{D0} - \frac{1}{2} T_{BOC}\right), & T_{D0} - \frac{1}{2} T_{BOC} \leq T_D \leq T_{D0} + \frac{1}{2} T_{BOC} \\ 0, & T_D > T_{D0} + \frac{1}{2} T_{BOC} \end{cases} \quad (4.13)$$

where  $T_{D0}$  is the zero-crossing time of the BOC,  $T_{BOC}$  is the linearly varying range of  $P_F$ , and  $E = \int |E_1(t)|^2 dt$ . Temporal center-of-gravity (COG) of  $E_1$  is defined as its first order moment in  $t$ :

$$T_{COG} = \frac{1}{E} \lim_{T \rightarrow \infty} \int_{-T}^T t |E_1(t)|^2 dt \quad (4.14)$$

and since

$$\int_{-T}^T t |E_1(t)|^2 dt = t \int_{-\infty}^t |E_1(\tau)|^2 d\tau \Big|_{-T}^T - \int_{-\infty}^{\infty} \int_{-\infty}^t |E_1(\tau)|^2 d\tau dt \quad (4.15)$$

$$= -TE + \frac{k_2}{|K|^2(k_2 - k_1)} \int_{-T}^T P_F(t) dt$$

By inserting  $P_F(T_D)$  from Equation (4.13), we finally get,

$$T_{COG} = T_{D0} \quad (4.16)$$

Consequently:

$$\Delta T_{COG} = \Delta T_{D0} \quad (4.17)$$

This means that any change in the temporal COG of the link-pulses will shift the zero-crossing of the BOC curve and there will be an unavoidable timing error. Figure 4.10 is the graphical illustration of the BOC response to temporal profile distortions of the input pulses. In the presence of first order distortions causing only amplitude modulation of the input pulse envelopes, the zero-crossing time of the BOC preserves its position. If the timing link is stabilized by activating a feedback loop on this point, output timing of the link will be immune to amplitude fluctuations (similar to the case simulated in Figure 2.3). However, if the input pulses are subject to higher order distortions causing temporal COG shifts in the pulse profile, the zero-crossing time of the BOC will shift by the same amount due to Equation (4.17). In this case, even locking at the BOC zero-crossing will cause timing errors since zero-voltage signal constitutes the reference point for the feedback loop which will track its shift inadvertently.

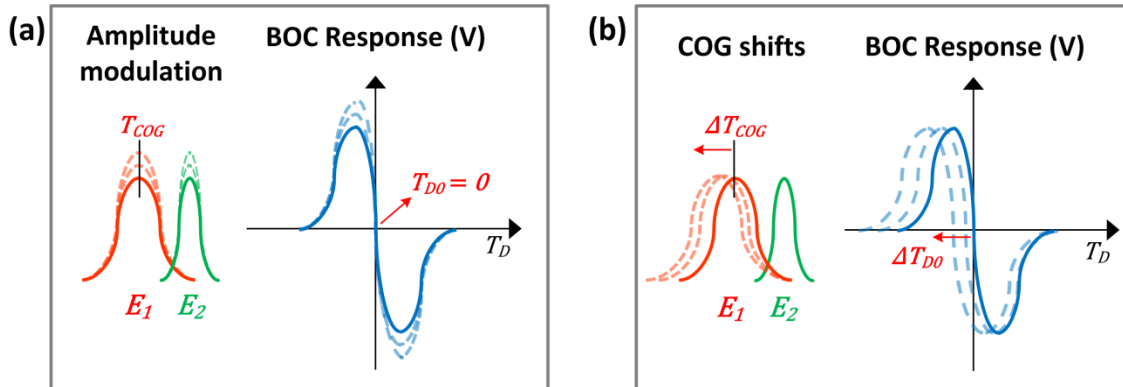


**Figure 4.10: BOC response to temporal profile distortions of the input pulses.**

(a) Effect of first order amplitude modulations. (b) Effect of higher order pulse distortions causing temporal COG shift.  $E_1$  and  $E_2$ : input electric fields of the link- and reference-pulses;  $T_D$ : initial time delay;  $T_{COG}$ : temporal COG;  $T_{D0}$ : zero-crossing time of the BOC.

### 4.3.2 TEMPORAL COG SHIFTS DURING NONLINEAR PULSE PROPAGATION

Next, we study nonlinear pulse propagation inside optical fibers and its influences on the temporal profile of the transmitted optical pulses. Let's define  $A(z, T)$  as the slowly varying envelope of the pulse electric field traveling through the fiber link in its retarded time frame. The electric field of the optical pulse in a fiber is governed by the nonlinear Schrödinger equation [97]:

$$\frac{\partial A}{\partial z} = \left( -\frac{\alpha}{2} - \frac{i\beta_2}{2} \frac{\partial^2}{\partial T^2} + \frac{\beta_3}{6} \frac{\partial^3}{\partial T^3} \right) A + i\gamma \left( |A|^2 A + \frac{i}{\omega_0} \frac{\partial}{\partial T} (|A|^2 A) - T_R A \frac{\partial |A|^2}{\partial T} \right) \quad (4.18)$$

where  $\alpha$  is the fiber loss,  $\beta_2$  and  $\beta_3$  are the SOD and the TOD coefficients,  $\gamma$  is the nonlinear coefficient for self-phase modulation (SPM),  $\omega_0$  is the carrier angular frequency, and  $T_R$  is the Raman parameter. As described in Figure 4.2, our timing links consist of two fiber sections: standard PM fiber, and PM dispersion compensating fiber. Here we assume that  $\alpha$  and  $T_R$  are constant, whereas  $\beta_2$ ,  $\beta_3$  and  $\gamma$  are  $z$ -dependent. The slowly varying envelope of the pulse can be written in terms of a normalized amplitude function  $U(z, t)$  on a time scale  $t$  normalized to the input pulse duration  $T_0$ :

$$A(z, T) = \sqrt{P_0} \exp\left(-\frac{\alpha z}{2}\right) U(z, t) \quad (4.19)$$

where  $t = T/T_0$  and  $P_0$  is the peak power of the input pulse. Plugging this pulse envelope function into the nonlinear Schrödinger equation results in:

$$\frac{\partial U}{\partial z} = -\frac{i\beta_2}{2T_0^2} U_{tt} + \frac{\beta_3}{6T_0^3} U_{ttt} + i\gamma P_0 \exp(-\alpha z) \left( |U|^2 U + \frac{i}{\omega_0 T_0} (|U|^2 U)_t - \frac{T_R}{T_0} U |U|_t^2 \right) \quad (4.20)$$

where the subscript  $t$  indicates the temporal partial derivative, i.e.,  $U_t \equiv \partial U / \partial t$ . Furthermore, temporal COG of  $A(z, t)$  can be written as:

$$t_{COG} = \frac{\int_{-\infty}^{\infty} T |A(T)|^2 dT}{\int_{-\infty}^{\infty} |A(T)|^2 dT} = T_0 \int_{-\infty}^{\infty} t |U(t)|^2 dt \quad (4.21)$$

Based on Equation (4.16), we know that timing drift detected by the BOC can be characterized by changes in  $t_{COG}$ . Hence by inserting Equation (4.20) into (4.21); spatial derivative of  $t_{COG}$  is given by:

$$\begin{aligned} \frac{dt_{COG}}{dz} = T_0 \int_{-\infty}^{\infty} t \left[ \frac{i\beta_2}{2T_0^2} (U_{tt}^* U - U_{tt} U^*) + \frac{\beta_3}{6T_0^3} (U_{ttt}^* U + U_{ttt} U^*) \right. \\ \left. - \frac{3\gamma P_0 \exp(-\alpha z)}{\omega_0 T_0} |U|_t^2 |U|^2 \right] dt \end{aligned} \quad (4.22)$$

For time points far away from a single pulse ( $t \rightarrow \pm\infty$ ), it is reasonable to assume that the pulse temporal profile is well-behaved and decays to zero:

$$\lim_{t \rightarrow \pm\infty} U(z, t) = 0 \quad (4.23)$$

$$\lim_{t \rightarrow \pm\infty} \frac{\partial^n U(z, t)}{\partial t^n} = 0, \quad n = 1, 2, 3, \dots \quad (4.24)$$

Then Equation (4.22) can be written as:

$$\frac{dt_{COG}}{dz} = \frac{i\beta_2}{2T_0}\Omega + \frac{\beta_3}{2T_0^2}\Gamma + \frac{3\gamma P_0 \exp(-\alpha z)}{2\omega_0}S \quad (4.25)$$

Where

$$\Omega = \int_{-\infty}^{\infty} (U_t U^* - U U_t^*) dt \quad (4.26)$$

$$\Gamma = \int_{-\infty}^{\infty} |U_t|^2 dt \quad (4.27)$$

$$S = \int_{-\infty}^{\infty} |U|^4 dt \quad (4.28)$$

The spatial derivatives of  $\Omega$  and  $\Gamma$  can be further calculated as:

$$\frac{d\Omega}{dz} = i2\gamma P_0 \exp(-\alpha z) \frac{T_R}{T_0} F_1(z) \quad (4.29)$$

$$\frac{d\Gamma}{dz} = i\gamma P_0 \exp(-\alpha z) \left( F_2(z) - \frac{T_R}{T_0} F_3(z) \right) \quad (4.30)$$

where

$$F_1(z) = \int_{-\infty}^{\infty} (|U|_t^2)^2 dt \quad (4.31)$$

$$F_2(z) = \int_{-\infty}^{\infty} |U|_t^2 (U U_t^* - U^* U_t) dt \quad (4.32)$$

$$F_3(z) = \int_{-\infty}^{\infty} |U|_{tt}^2 (U U_t^* - U^* U_t) dt \quad (4.33)$$

With a numerical calculation,  $F_2(z)$  and  $F_3(z)$  can be easily verified to be nonzero for Gaussian and hyperbolic secant pulses with nonzero residual dispersion. Substituting the integrated forms of Equations (4.29) and (4.30) into (4.25) and integrating (4.25) over the fiber link length  $L$ , we get:

$$\begin{aligned} t_{COG} = & \frac{1}{2T_0^2} \int_{-\infty}^{\infty} |U_t(t, 0)|^2 dt \int_0^L \beta_3 dz \quad (4.34) \\ & - P_0 \left[ 2 \frac{T_R}{T_0^2} \int_0^L \beta_2 \int_0^z \gamma \exp(-\alpha z_1) F_1(z_1) dz_1 dz \right. \\ & + \frac{1}{T_0^2} \int_0^L \beta_3 \int_0^z \gamma \exp(-\alpha z_1) F_2(z_1) dz_1 dz \\ & - \frac{T_R}{T_0^3} \int_0^L \beta_3 \int_0^z \gamma \exp(-\alpha z_1) F_3(z_1) dz_1 dz \\ & \left. + \frac{3}{2\omega_0} \int_0^L \gamma \exp(-\alpha z) S(z) dz \right] \end{aligned}$$

Suppose that the optical power inside the fiber link fluctuates with a ratio  $\delta$  such that  $P_0(1+\delta)$ . Then according to Equation (4.34), the temporal COG of the pulse will also fluctuate by (i.e.,  $t_{COG} + \Delta t_{COG}$ ):

$$\begin{aligned}
\Delta t_{COG} = -P_0\delta & \left[ 2 \frac{T_R}{T_0^2} \int_0^L \beta_2 \int_0^z \gamma \exp(-\alpha z_1) F_1(z_1) dz_1 dz \right. \\
& + \frac{1}{T_0^2} \int_0^L \beta_3 \int_0^z \gamma \exp(-\alpha z_1) F_2(z_1) dz_1 dz \\
& - \frac{T_R}{T_0^3} \int_0^L \beta_3 \int_0^z \gamma \exp(-\alpha z_1) F_2(z_1) dz_1 dz \\
& \left. + \frac{3}{2\omega_0} \int_0^L \gamma \exp(-\alpha z) S(z) dz \right] \tag{4.35}
\end{aligned}$$

Finally, Equation (4.35) clarifies the physical mechanism behind the residual timing drift in the fiber links that limits the long-term precision of our timing distribution system. Power fluctuations induce temporal shifts in the COG of the optical pulses at the link output through a composite effect of link nonlinearities (i.e., residual SOD, TOD, SPM, self-steepening and Raman effect) which cannot be corrected by the BOC detection scheme (due to Equation (4.17)).

### 4.3.3 SIMULATION RESULTS

The implications of Equation (4.34) are not only limited to comprehend the contribution of power fluctuations to the residual timing drift. On the contrary, it can also be solved to study other noise sources in the fiber links such as the effect of residual dispersion and the influence of inherent timing jitter of the master laser on the pulse propagation. Therefore, we also develop a numerical model to simulate pulse timing jitter during nonlinear pulse propagation in the fiber link.

In the simulation, a pulse train of 216-MHz repetition rate and 170-fs pulse duration is propagated in a 3.5-km PM dispersion-compensated fiber with an EDFA and a partial reflector at the link output. The split-step Fourier method with adaptive step length is used for the solutions of the nonlinear Schrödinger equation (4.18) and for the BOC coupled field equations (4.2) – (4.4). BOC response curve is calculated for each link-pulse after round-trip propagation against a noise-free reference pulse. Temporal shift in the BOC zero-crossing point is identified as timing error.

First, the timing drift introduced by link power fluctuations is investigated that are related to environmental fluctuations occurring on slow timescales below 10 Hz. As mentioned in Section 4.2.1, there is a small difference between the ratios of SOD and TOD of the standard PM 1550 fiber and the PM-DCF (see Equation (4.1)). Therefore, when the SOD of the 3.5-km link is eliminated, 26-m worth of TOD would remain uncompensated. Figure 4.11(a) shows the calculated timing drift introduced by link power fluctuations at different residual TOD values. 26-m worth of residual TOD from the standard PM fiber would introduce a drift of  $\sim 2$  fs for  $\pm 5\%$  link power fluctuations which agrees well with our experimental results in Figure 4.4(c) and Figure 4.8(a). Furthermore, Figure 4.11(b) indicates that +10-dBm link power (corresponding to a pulse peak power of  $P_{\text{peak}}=270$  W) is

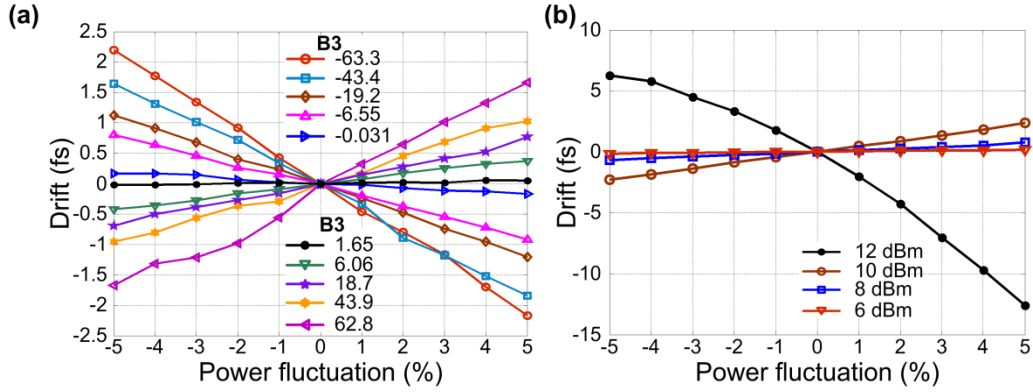


**Figure 4.11: Timing drift introduced by link power fluctuations.**

B2: residual SOD normalized by the SOD of 1-m standard PM 1550 fiber, B3: residual TOD normalized by the TOD of 1-m PM 1550 fiber. (a) Simulation results for different residual TOD values when the link input power is +8 dBm and B2=-0.13. (b) Simulation results for different link input power levels for each curve B2=-0.13 and B3=18.7. This figure is reproduced from our article [98].

the threshold before significant amplitude-to-timing conversion occurs due to severe nonlinear pulse distortions that may result in 4-fs timing error from  $\pm 5\%$  power fluctuations. Therefore, link power variations and residual TOD must be minimized to achieve long-term attosecond precision.

Besides the long-term drifts related with link power fluctuations, fast timing jitter of an optical pulse train (i.e.,  $>1$  kHz) can also be enhanced during nonlinear pulse propagation. For these calculations, inherent timing jitter of the master laser is simulated with the master equation of a fast saturable absorber mode-locked laser by adding ASE noise, whose amount corresponds to the measured jitter in Figure 3.4(b) (0.4 fs,  $>1$  kHz). Then the master equation is solved using the fourth-order Runge-Kutta method in the interaction picture [99].

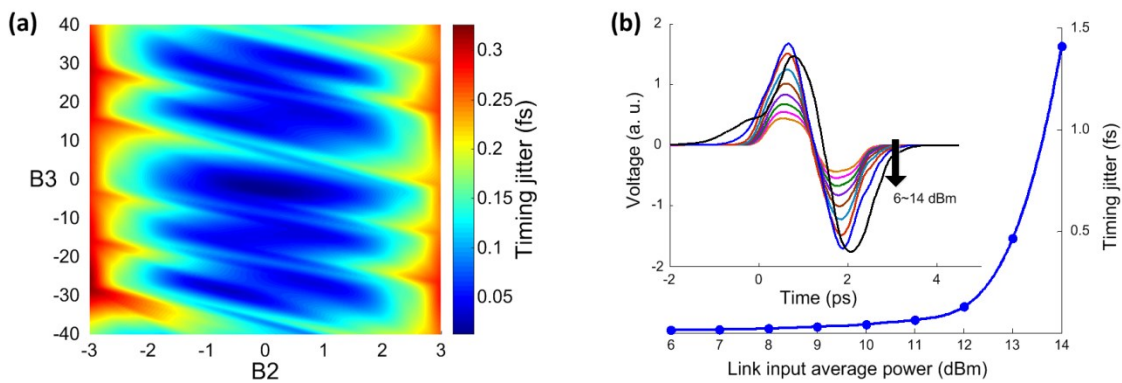


**Figure 4.12: Timing jitter induced by the fiber nonlinearities.**

B2: residual SOD normalized by the SOD of 1-m standard PM 1550 fiber, B3: residual TOD normalized by the TOD of 1-m PM 1550 fiber. (a) Link-induced Gordon-Haus jitter due to residual link dispersion. (b) Link-enhanced ASE noise due to fiber nonlinearities and the corresponding BOC characteristics at each input power level. This figure is reproduced from our article [98].

The simulation is repeated for a train of laser pulses in the presence of pulse timing jitter. RMS timing error of the BOC response curves is calculated to obtain the excess jitter caused by the fiber link propagation.

Based on our simulation results, residual link dispersion and nonlinearities add considerable excess jitter even in the absence of environmental noise. They will determine the high-frequency limit above 1 kHz for the link stabilization if not carefully understood and compensated for. As can be seen in Figure 4.12(a), center-frequency fluctuations of the optical pulse are converted to timing jitter via residual SOD and TOD. This noise contribution, often called Gordon-Haus jitter [100], can cause a timing error of 0.3 fs in the case of uncompensated SOD equivalent to 3-m standard PM fiber. Furthermore, spontaneous emission noise is also converted to timing jitter and its impact is further enhanced by link nonlinearities (see Figure 4.12(b)). This noise source is bounded at 0.13 fs for average power levels below +12 dBm ( $P_{\text{peak}}=430$  W) but escalates to 1.4 fs at +14 dBm ( $P_{\text{peak}}=682$  W). Hence, the link input power must be optimized carefully since this jitter source reaches the femtosecond-level before a visible distortion of the BOC response can be observed (see the inset of Figure 4.12(b)).

#### 4.3.4 FEEDBACK LOOP ANALYSIS OF TIMING LINK STABILIZATION

In order to investigate how the link-induced noise sources affect the timing distribution system, we also develop a feedback model for the timing link stabilization. According to the feedback flow in Figure 4.13(a), the timing jitter of the fiber link  $J_I$  is detected by the BOC and converted to a voltage signal by the transfer function  $H_{BOC}$ . Then the BOC signal is amplified by the internal amplifier of the BPD with the transfer function  $H_{BPD}$  and the detector noise  $E_{BOC}$ . The BPD signal is fed to the PI controller  $H_{PI}$  in a negative feedback configuration. The output of the PI controller together with its electronic noise  $E_{PI}$  is amplified and converted to a jitter value  $J_F$  by the fiber stretcher  $H_{PZT}$ , which acts as a compensating jitter to maintain the lock.

During the link propagation, additional noise from link-induced Gordon-Haus jitter and link-enhanced timing jitter due to fiber nonlinearities arises through  $H_{LR}$  and  $H_{LF}$ . Since we perform error detection upon round-trip link propagation, delayed copies of the compensation jitter  $J_F$ , master laser's inherent jitter  $J_M$  and the environmental jitter imposed on the link  $J_E$  are also added to the link jitter beside the original sources. Round-trip link delay  $2\tau_L$  is considered for  $J_F$  and  $J_M$ . Since the environmental noise is usually insignificant above 10 kHz, the forward and backward link transmissions for a 3.5-km link impose the same environmental jitter value  $J_E$  on the link pulses. Therefore, only one-way link delay  $\tau_L$  is applied to  $J_E$  as it already includes one-way integrated jitter.

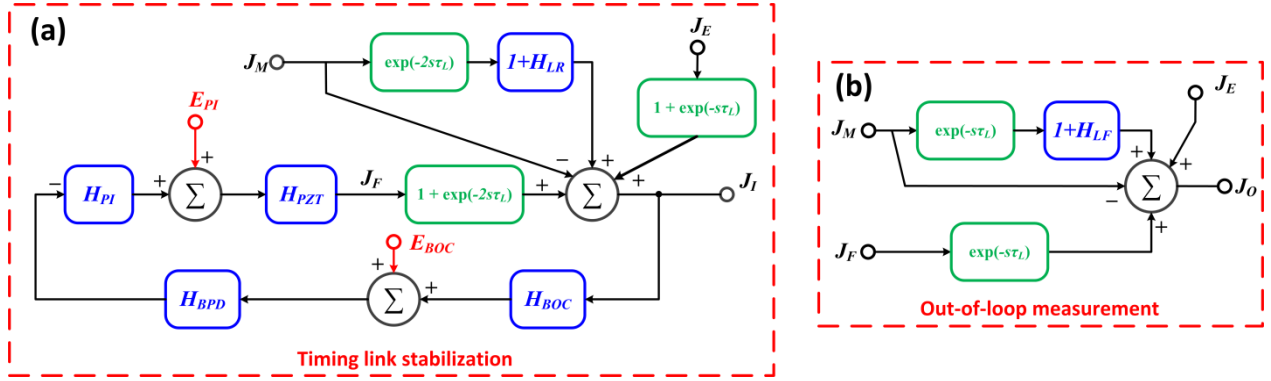


**Figure 4.13: Feedback model of timing link stabilization.**

Feedback flow diagram of (a) timing link stabilization and (b) out-of-loop measurement.  $J_M$ : free-running timing jitter of the master laser;  $J_E$ : total environmental jitter imposed on the link for one-way travel;  $J_I$  and  $J_O$ : timing jitter detected by the in-loop and out-of-loop BOC;  $J_F$ : equivalent jitter generated by the feedback loop to maintain the lock;  $H_{BOC}$ ,  $H_{BPD}$ ,  $H_{PI}$  and  $H_{PZT}$ : transfer functions of the BOC, BPD, PI controller and PZT fiber stretcher, respectively;  $H_{LF}$  and  $H_{LR}$ , the equivalent transfer functions of the link-induced timing jitter for forward and round-trip transmission;  $E_{BOC}$  and  $E_{PI}$ : electronic noise of the BOC and the PI controller;  $\tau$ : one-way fiber link travel time;  $s=j\omega$ : complex frequency.

The in-loop jitter  $J_I$  is the relative jitter between the round-trip link pulses and new pulses from the master laser. The out-of-loop jitter  $J_O$  is the relative jitter between the link output pulses and new pulses from the master laser. For the out-of-loop measurement model in Figure 4.13(b),  $J_F$  and  $J_M$  experience one-way link delay  $\tau_L$ . Furthermore, the environment contributes a timing jitter  $J_E$  and  $J_M$  experiences an additional link-induced timing jitter via  $H_{LF}$ . Based on this model, the timing jitter detected by the in-loop BOC is:

$$J_I = J_M[-1 + \exp(-2s\tau_L)(1 + H_{LR})] + J_F[1 + \exp(-2s\tau_L)] + J_E[1 + \exp(-s\tau_L)] \quad (4.36)$$

$$\text{where } J_F = [-(J_I H_{BOC} + E_{BOC})H_{BPD}H_{PI} + E_{PI}]H_{PZT}$$

and the out-of-loop measurement yields:

$$J_O = J_M[-1 + \exp(-s\tau_L)(1 + H_{LF})] + J_F \exp(-s\tau_L) + J_E \quad (4.37)$$

Similar to Equations (3.2) and (3.3), we define  $J_N$  as the electronic noise jitter term; and  $H$  as the total transfer function of the BOC lock:

$$J_N = -\frac{E_{BOC}}{H_{BOC}} + \frac{E_{PI}}{H_{BOC}H_{BPD}H_{PI}} \quad (4.38)$$

$$H = H_{BOC}H_{BPD}H_{PI}H_{PZT} \quad (4.39)$$

Furthermore, let us introduce a factor  $k$  representing the degree of symmetry between the link-induced jitter on the forward and backward propagations:

$$k = \frac{H_{LF}}{H_{LR}} \quad (4.40)$$

By solving Equations (4.36) – (4.40) together, out-of-loop timing jitter of the link is found as:

$$J_O = C_E J_E + C_N J_N + C_M J_M + C_L H_{LR} J_M \quad (4.41)$$

and the transfer coefficients are given by:

$$C_E = \frac{1 + H[1 - \exp(-s\tau_L)]}{1 + H[1 + \exp(-2s\tau_L)]} \quad (4.42)$$

$$C_N = \frac{H \exp(-s\tau_L)}{1 + H[1 + \exp(-2s\tau_L)]} \quad (4.43)$$

$$C_M = \frac{1 + H[1 - \exp(-s\tau_L)]}{1 + H[1 + \exp(-2s\tau_L)]} [\exp(-s\tau_L) - 1] \quad (4.44)$$

$$C_L = \frac{k + H[k - \exp(-2s\tau_L)(1 - k)]}{1 + H[1 + \exp(-2s\tau_L)]} \exp(-s\tau_L) \quad (4.45)$$

where  $s$  is the complex frequency. There are four main noise sources at the out-of-loop timing jitter: the environmental noise imposed on the link, the electronic noise of the system, the master laser's inherent jitter and the link-induced jitter. The coefficients  $C_E$ ,  $C_N$ ,  $C_M$  and  $C_L$  determine the contribution of each noise source to the out-of-loop timing jitter and they can be calculated using the transfer functions of the experimental equipment (see Appendix A.1 and Table A.2). Figure 4.14(a)-(c) show the frequency dependence of  $|C_E|$ ,  $|C_N|$  and  $|C_M|$  for varying feedback gain.

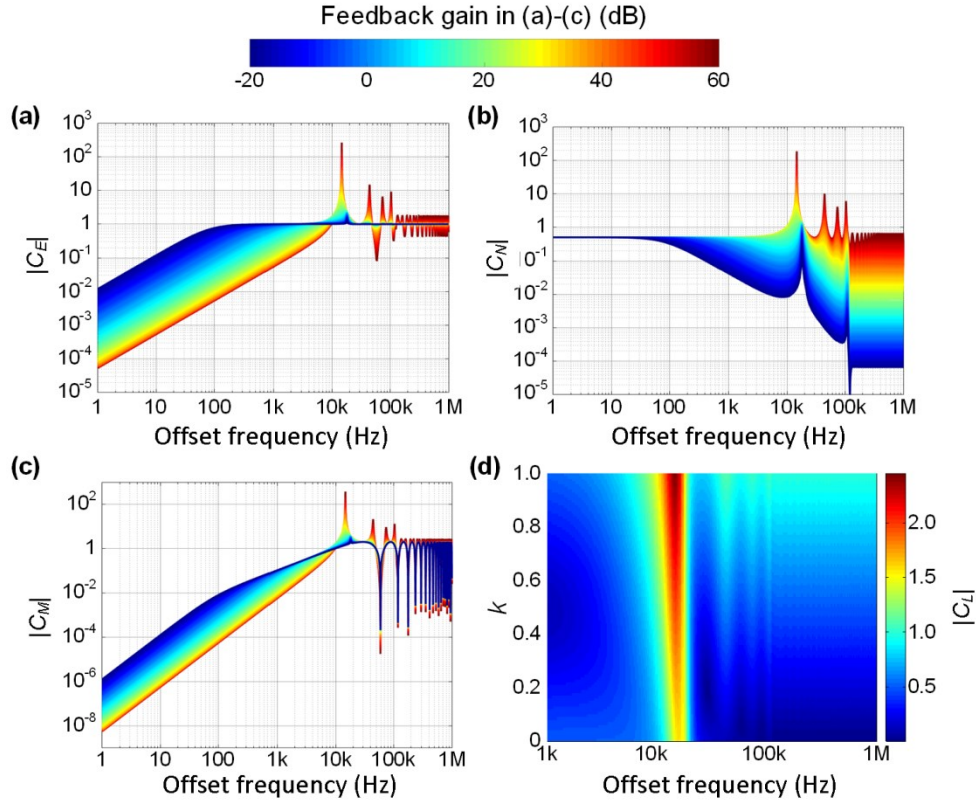


**Figure 4.14: Simulation results of the timing link feedback model.**

(a)-(c) Transfer coefficients for the environmental noise, electronic noise and inherent timing jitter of the master laser for different feedback gains as indicated in the top legend. (d) Transfer coefficient for the link-induced jitter for different  $k$  values. This figure is reproduced from our article [87].

High feedback gain is necessary to suppress the environmental noise below 1 kHz (Figure 4.14(a)). However, the electronic noise from the BOC lock rises with the increasing gain (Figure 4.14(b)) and noise amplification peaks appear in the complete system (Figure 4.14(a)-(c)) at frequencies  $n/4\tau_L$  ( $n$  is an odd integer) as well as around the resonant frequency of the fiber stretcher ( $\sim 16$  kHz). Therefore, a moderate value for the feedback gain (e.g., 20 dB) must be chosen to optimize the system performance. At 20-dB feedback gain,  $|C_L|$  exponentially increases from 0.02 at 1 kHz to 4.6 at  $\sim 16$  kHz which means that the inherent jitter of the master laser can appear in the out-of-loop measurement through the feedback loop even with amplification.

Figure 4.14(d) displays the calculated transfer coefficient of the link-induced jitter for varying  $k$  values at 20-dB feedback gain. If the amounts of link-induced jitter during the forward and reverse link propagation are almost identical (e.g., in the case of Gordon-Haus jitter shown in Figure 4.12(a)), then  $k$  equals to 0.5, and  $|C_L|$  increases from 0.12 at 1 kHz to 2 at 14.6 kHz. If the power in the reverse link propagation is much higher than in the forward propagation (e.g., in the case of the nonlinearity-induced jitter shown in Figure 4.12(b)), the majority of the timing jitter is coming from the backward trip and  $k$  is almost zero. In this case,  $|C_L|$  is about 0.5 at 1 kHz and approaches 1.5 at 16 kHz. On the other hand, if the forward power is greater than the reverse,  $k$  is close to 1, and  $|C_L|$  rises from 0.5 to 2.4 within [1 kHz - 14 kHz]. Above all, the link-induced jitter in Figure 4.12(a) and (b) is transferred to the link output through the feedback loop; either partially, completely or even with amplification.

## 4.4 ATTOSECOND PRECISION FIBER LINK NETWORK

### 4.4.1 KEY IMPROVEMENTS IN THE FIBER LINK STABILIZATION

Considering the outcomes of the jitter and feedback analysis presented in the previous section, we revisit the link network experiment by constructing the setup shown in Figure 4.15. When compared with the previous demonstration in Figure 4.7, key improvements are summarized as follows:

- Timing stabilization of the two fiber links is performed by polarization-noise-suppressed BOCs (PNS-BOCs in Figure 4.15(b)). By inserting a highly birefringent material (e.g., BBO) before each SH-BOC, the undesired polarization components of the input pulses (i.e.,  $E_{1y}$  and  $E_{2x}$ ) are spatially separated and only the desired ones (i.e.,  $E_{1x}$  and  $E_{2y}$ ) generate second-harmonic light. This improves the long-term stability of the BOC by removing the background polarization noise and ensuring an ideal zero AM-to-PM conversion at the zero-crossing point of the BOC response (refer to Section 2.2.1 for the analytical derivation).
- Input and output optical power of each fiber link is carefully adjusted to minimize the nonlinearity-induced jitter (see Figure 4.12(b)) as well as to maximize the SNR for BOC locking.

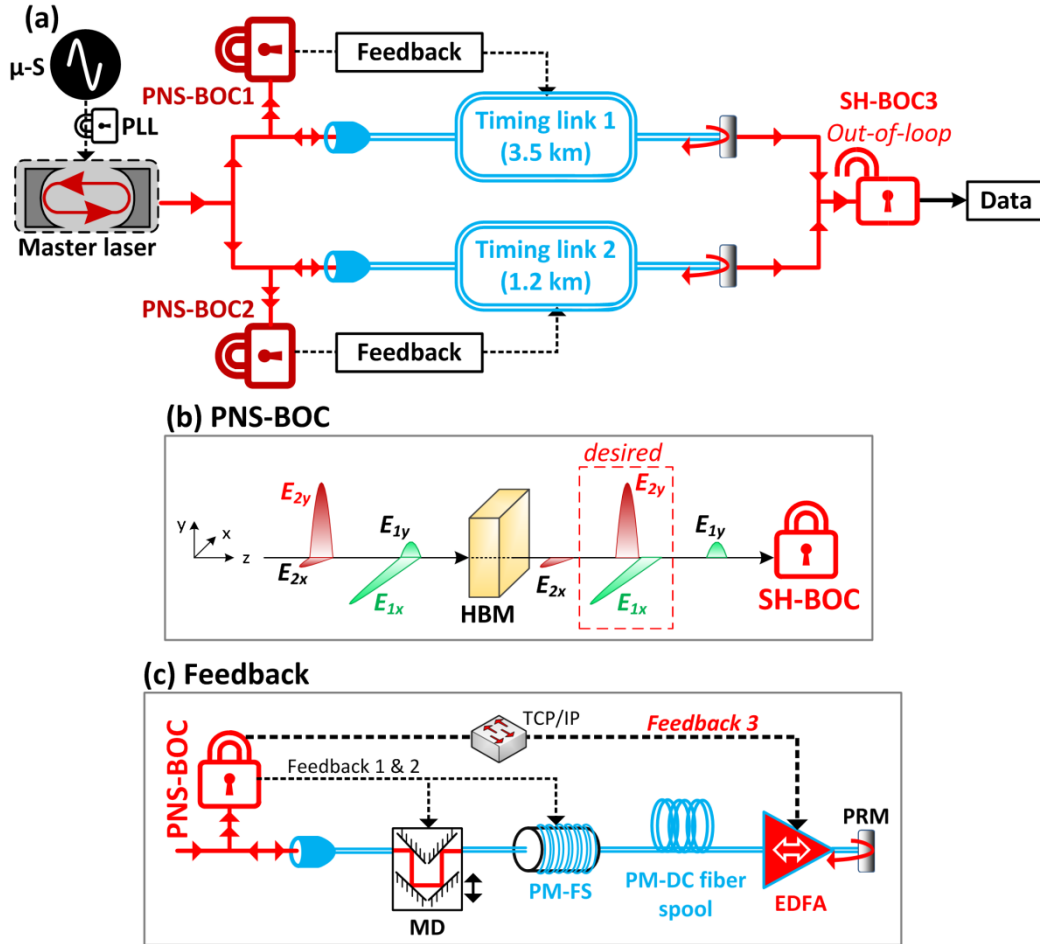


**Figure 4.15: Improved experimental setup for fiber-link network stabilization.** (a) Main schematic of the experiment. (b) Polarization-noise-suppressed BOCs (PNS-BOCs) used in link stabilization. (c) New feedback scheme including link power stabilization via EDFA (*Feedback 3*).  $\mu$ -S: microwave source; PLL: phase-locked-loop; HBM: highly-birefringent material; MD: motorized delay; PM-FS: PM fiber stretcher; TCP/IP: transmission control protocol / internet protocol.

- Residual SOD and TOD of the links are compensated with additional dispersion-compensating fiber to suppress the link-induced Gordon-Haus jitter (see Figure 4.12(a)) and to minimize the output pulse durations for high SNR in the BOCs.
- Fast and slow feedback controls via the fiber stretcher and the motorized delay (Feedback 1 and 2 in Figure 4.15(c)) operate simultaneously to correct for the detected timing link fluctuations. Since these two controls are not orthogonal to each other, actuation of one of them causes a noise source for the other. For instance, if the motorized delay moves fast with large steps, the bandwidth of the fiber stretcher may not be sufficient to catch up with this variation and timing fluctuations will be observed in the out-of-loop results. On the other hand, if the motorized delay is too slow, the feedback control will not be able to respond to the environmental fluctuations and the lock will be lost. Therefore, coordination of the fast and slow feedback controls in terms

response time and bandwidth is necessary to achieve efficient link stabilization. After an experimental investigation, we have optimized the motorized delay response with 0.01 mm/s that can compensate a temperature drift of 0.001°C/s for a 3.5-km link.

- Since the link power is amplified by the EDFA to provide sufficient pulse energy both for link stabilization and remote laser synchronization, the average power of forward propagating and backward propagating pulses are not equal to each other (e.g., +8 dBm and +13 dBm, respectively for timing link 1). Since the accumulated temporal COG is proportional to the pulse peak power, the forward- and backward-propagation in the link result in different amounts of temporal shifts causing an asymmetrical timing fluctuation which cannot be corrected by a roundtrip feedback mechanism. To eliminate this power-fluctuation-induced drift (as observed in Figure 4.8), a new feedback mechanism is developed as shown in Figure 4.15(c). In this scheme, operational power fluctuations of each link are measured by the BPD monitor ports (i.e., the detected optical power by the individual photodetectors) of the PNS-BOCs at the link input station. Then a feedback signal is sent to the pump current of the EDFA through a TCP/IP network to stabilize the link power. Alternatively, the observed link power fluctuation can be used as a feedforward signal to control the delay of an out-of-loop PZT mirror. However, one has to be careful in this case with the environmental stability of uncompensated beam paths whose fluctuations would also cause timing drift.

#### 4.4.2 EXPERIMENTAL RESULTS: IMPROVED FEEDBACK

To evaluate the out-of-loop timing precision, the outputs of the timing-stabilized fiber links are combined in a free running SH-BOC and the experimental data is recorded with acquisition system described in Figure 4.3(d). Stabilization of the timing link network is operated continuously for 52 h and Figure 4.16(a) shows the measured residual timing drift between the two link outputs. The improved feedback scheme for the link stabilization effectively reduces the long-term fluctuations observed in the traditional method (see Figure 4.8(a)) and results in an unprecedented timing error of only 200 as RMS measured below 1-Hz offset frequency. Throughout the measurement, the temperature in the laboratory varies by 0.3 K and the relative humidity fluctuates by 4% (Figure 4.16(b)) and the resulting delay changes are  $\sim 35$  ps and  $\sim 10$  ps for the 3.5-km and the 1.2-km links, respectively (Figure 4.16(c)). With the help of the new feedback control, power fluctuations in the 1.2-km link are suppressed to within  $\pm 0.2\%$  (blue curve in Figure 4.16(d)). Due to the coarse resolution of the EDFA pump current, the power fluctuations in the 3.5-km link can only be stabilized to within  $\pm 1\%$  (red curve in Figure 4.16(d)) which serves as the main drift contribution below 1 Hz as can be seen in in Figure 4.16(a).

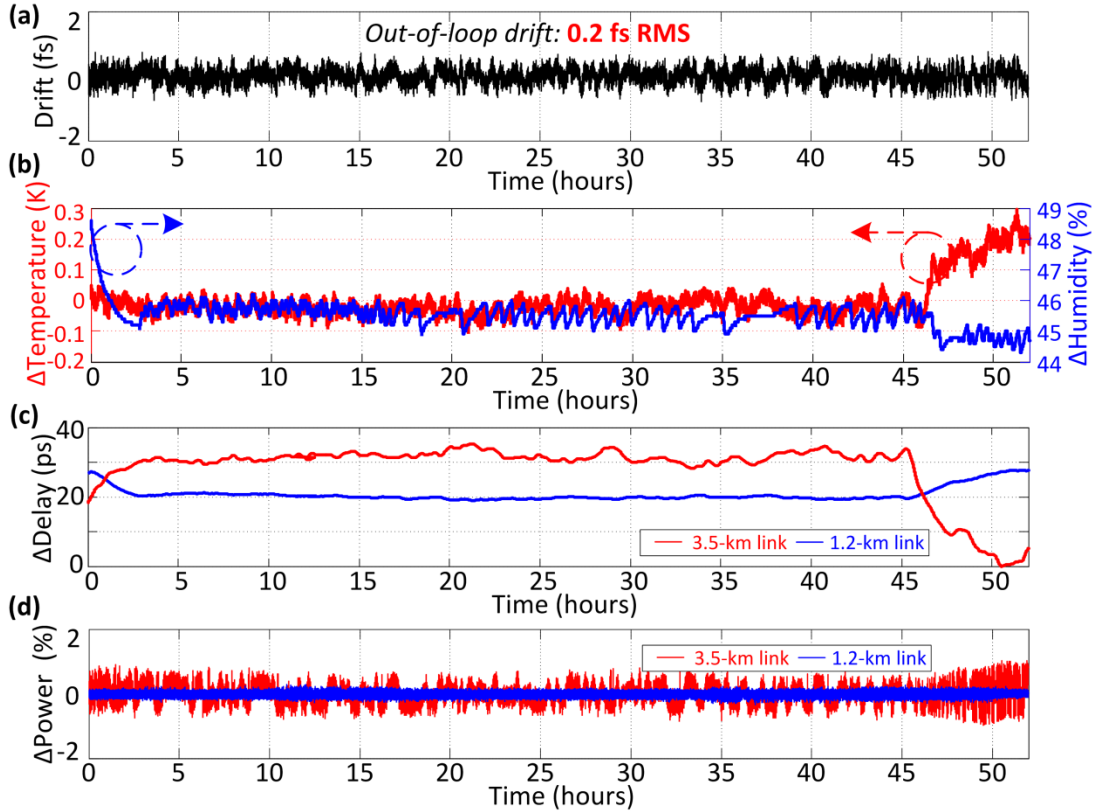


**Figure 4.16: Long-term measurement results of the improved link-network.**

(a) Residual timing drift measured by SH-BOC3. (b) Temperature ( $\Delta$  Temperature, left axis) and relative humidity change ( $\Delta$  Humidity, left axis) in the laboratory. (c) Corrected link drifts ( $\Delta$  Delay) by the motorized delays. (d) Power fluctuations ( $\Delta$  Power) of the timing links measured by the BPD monitor ports.

The complete jitter spectral density from 7  $\mu$ Hz to 1 MHz is plotted in Figure 4.17(a) (black curve) resulting in a total integrated jitter (red curve) of only 580 as RMS. The majority of the timing jitter stems from the offset frequencies larger than 1 kHz (i.e.,  $\sim$ 500 as for [1 kHz - 1 MHz]), whereas the noise sources within the locking bandwidth of the link stabilization are effectively suppressed (i.e., only  $\sim$ 290 as for [7  $\mu$ Hz - 1 kHz]) with the help of the improved experimental setup.

Another powerful way to present the long-term performance of oscillators is the Allan deviation (ADEV) method [101]. ADEV analyzes a time sequence to extract the intrinsic noise in the system as a function of the averaging time. In this way, one acquires a quantitative measure of how much the average value of that time sequence changes at a particular averaging time (i.e., relative instability). Figure 4.17(b) illustrates the calculated ADEV of the link network for different stabilization conditions. The red and blue curves represent the individual instabilities of the 3.5-km and 1.2-km links, respectively calculated from their motorized delay data shown in Figure 4.16(c). This suggests that if the timing links are not stabilized, they will exhibit an instability larger than  $10^{-14}$  in 1-s and  $10^{-16}$  in 10 000-s averaging time, in other words an average timing error of 10-fs and 1-ps in 1 s and 10 000 s, respectively.

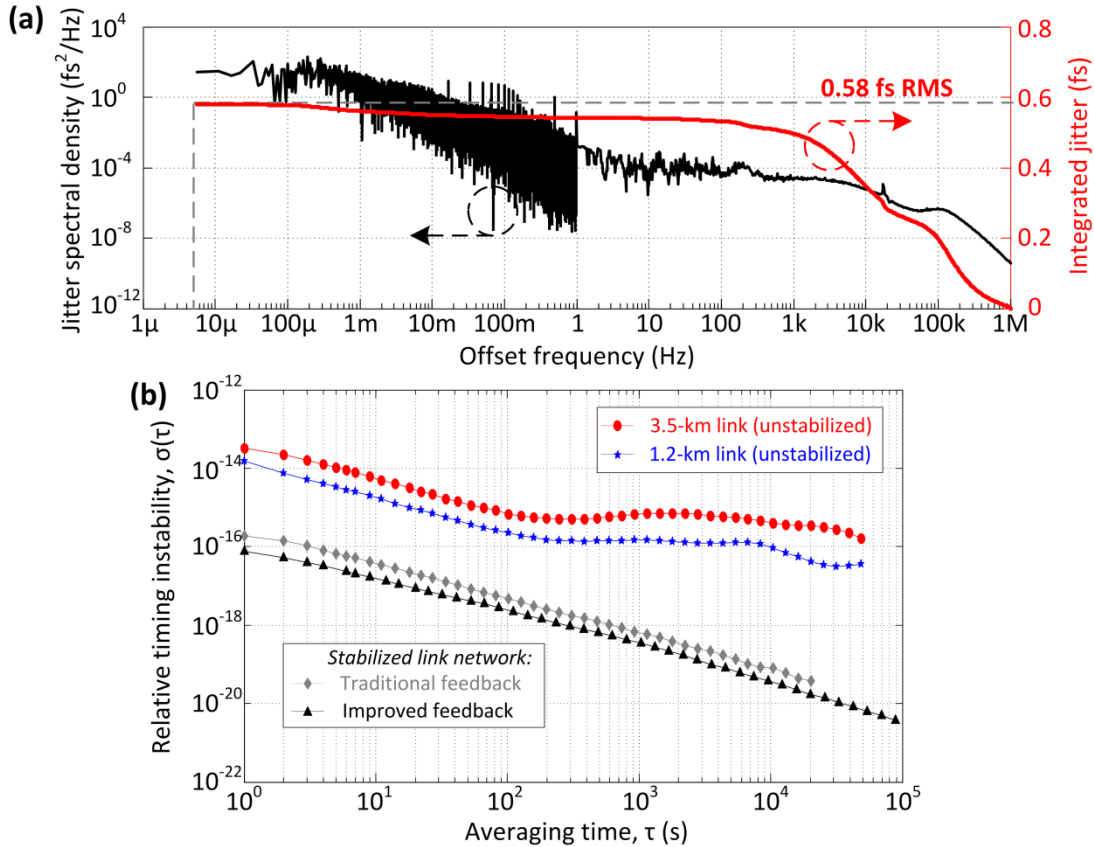


**Figure 4.17: Timing jitter and relative timing instability of the link network.**

(a) Timing jitter spectral density measured by the out-of-loop detector (black curve) and its integrated timing jitter (red curve). (b) Relative timing instability of the link network for different stabilization conditions expressed in terms of overlapping Allan deviation.

Once the link stabilization feedback loops are activated, the relative timing instability between the two link outputs drops significantly by at least two orders of magnitude. The gray curve in Figure 4.17(b) illustrates the link network results achieved with the traditional feedback control (calculated from the data in Figure 4.8(a)), whereas the black curve shows the relative timing instability of the network when the link power stabilization is engaged as well (calculated from the data in Figure 4.16(a)). Comparison of the two curves illustrates a clear long-term improvement for the complete range provided by the improved feedback control with a relative timing instability of only  $7.8 \times 10^{-17}$  in 1 s and  $3.7 \times 10^{-21}$  in 90 000-s averaging time.

## 5 LASER AND MICROWAVE SYNCHRONIZATION

New generation X-ray FELs and laser-based attoscience centers require many optical- and microwave-sources located in different stations working in an unprecedented temporal harmony to unfold their ultimate potential. So far, we have been able to demonstrate the first timing link network demonstrating attosecond precision. Now, the final task is to synchronize remote pulsed lasers and microwaves efficiently to our comprehensive timing network and determine the final output precision. One of the unique features of the pulsed, optical timing distribution system is the ability to synchronize other laser oscillators and microwave sources directly to the output of the distributed timing links using BOCs and BOMPDs, respectively.

This chapter starts with the general description of frequency synchronization of two oscillators using BOCs and BOMPDs. Then, local and remote synchronization of various mode-locked lasers is discussed together with their timing jitter analysis. Finally, an attosecond precision multi-kilometer laser-microwave network is demonstrated for the first time in the literature.

### 5.1 FREQUENCY SYNCHRONIZATION OF TWO OSCILLATORS

BOCs and BOMPDs can be used as high precision timing detectors to synchronize mode-locked lasers and microwave oscillators. This can be done with a simple optical PLL as shown in Figure 5.1, where the voltage response of the timing detector is used in a feedback loop to lock the frequency of the slave oscillator to that of the master oscillator. In Figure 5.1(a), pulse trains from two independent mode-locked lasers having a small repetition rate difference  $\Delta f_R$  are sent to a BOC to

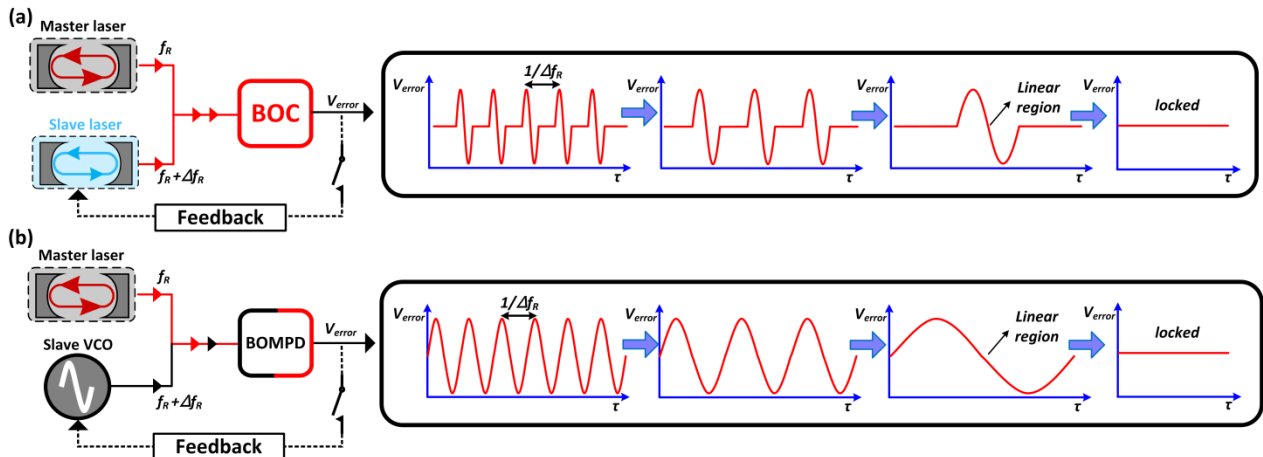


**Figure 5.1: Operating principle of frequency synchronization using BOCs and BOMPDs.** (a) Synchronization of two mode-locked lasers using a BOC. (b) Synchronization of a VCO and a mode-locked laser using a BOMPD.  $f_R$ : Repetition rate of the master oscillator;  $\Delta f_R$ : frequency mismatch of the slave oscillator;  $V_{error}$ : voltage response of the detector;  $\tau$ : absolute time measured by the oscilloscope.

measure their relative timing error. The repetition period difference between the two pulse trains  $\Delta T_R$  can be calculated as:

$$\Delta T_R = \frac{1}{f_R} - \frac{1}{f_R + \Delta f_R} = \frac{\Delta f_R}{f_R^2 + f_R \Delta f_R} \approx \frac{\Delta f_R}{f_R^2} \quad (5.1)$$

This means that the pulse trains temporally move with respect to each other by  $\Delta T_R$  in every  $T_R$  as depicted in Figure 5.2. As a result of this temporal pulse "sliding", the BOC generates a cross-correlation signal every time the pulses coincide. Assuming they first meet at  $\tau=0$ , then after  $n$  pulses of the master laser they overlap with each other one more time such that:

$$nT_R = (n-1)(T_R + \Delta T_R) \quad (5.2)$$

Since the repetition period is much larger than the period difference, i.e.,  $T_R \gg \Delta T_R$ ;  $n$  is found as:

$$n \approx \frac{T_R}{\Delta T_R} \quad (5.3)$$

Then, the response of the BOC will be a train of characteristic BOC traces as illustrated in Figure 5.1(a) with a frequency of:

$$f_{beat} = \frac{1}{nT_R} \approx \frac{\Delta T_R}{T_R^2} \quad (5.4)$$

By using Equation (5.1):

$$f_{beat} = \Delta f_R \quad (5.5)$$

In this way, one can record a BOC curve using an oscilloscope and measure the slope of the cross-correlation at the zero crossing point, in units of V/s. However, one has to convert the recorded time scale  $\tau$  (i.e., absolute time) to the relative time scale between the pulses  $\tau'$ . As Figure 5.2 indicates, one can simply deduct the conversion factor  $\xi$  (i.e.,  $\tau' = \xi\tau$ ) as:

$$\xi = \frac{\tau'}{\tau} \approx \frac{\Delta T_R}{T_R} = \frac{\Delta f_R}{f_R} \quad (5.6)$$

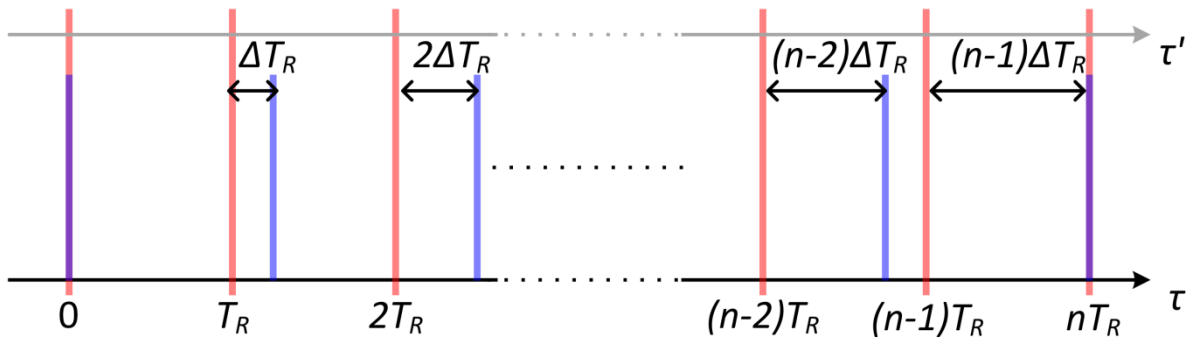


**Figure 5.2: Effect of repetition rate mismatch between two pulse trains.**

Two pulse trains represented with red and blue lines have a small repetition rate difference  $\Delta f_R$  and coincide in the nonlinear crystal for sum-frequency generation at times  $nT_R$  in the absolute time frame  $\tau$  and at times  $(n-1)\Delta T_R$  in the relative time frame  $\tau'$  between the pulse trains. The time axes are not to scale and  $\Delta T_R \ll T_R$ .

Similarly, when synchronizing a mode-locked laser with a microwave source, the voltage response of the BOMPD is a periodic signal as depicted in Figure 5.1(b) whose frequency is equal to the frequency mismatch between the two oscillators, i.e.,  $\Delta f_R$ . The timing sensitivity of the BOMPD in units of V/s can be derived from the linear slope around the zero crossings of the periodic signal. Again, the factor  $\xi$  in Equation (5.6) must be used to calibrate the absolute time scale recorded by the oscilloscope. Alternatively, the time scale can be multiplied with the frequency difference  $2\pi\Delta f_R$  to represent the phase error between the optical and microwave signal.

Response voltage of the BOC and the BOMPD can be used as a feedback signal to control the frequency of the slave oscillator via its intracavity PZT. Once the feedback control is activated, it will pull the frequency of the slave oscillator closer to that of the master which will stretch the periodic response curve further in time (see the sketches on the right in Figure 5.1). Once  $\Delta f_R$  is sufficiently small, the PLL will operate in the linear region of the detector output and lock the slave oscillator's frequency by suppressing the error voltage as tightly as possible to zero. Once a stable locking is achieved, the detector output will be a DC voltage.

## 5.2 REMOTE LASER SYNCHRONIZATION

In essence, remote synchronization of two oscillators is identical to the local synchronization provided that noise-free transmission of the master laser's signal is ensured. A perfect candidate for this task is a timing-stabilized fiber link whose development is detailed in Chapter 4. The setup built for the remote laser synchronization is shown in Figure 5.3. In this experiment, the output pulse train of the master laser is transmitted with the 3.5-km timing link whose time-of-flight fluctuations are stabilized by SH-BOC1. Then, the output of the timing link is used for the synchronization of the remote slave laser which is identical to the master laser (i.e., another Origami 15 produced by OneFive GmbH). Pulses from the link output and from the remote laser are combined on a PBS and the timing mismatch between the two pulse trains is detected by SH-BOC2. Due to limited frequency response of high voltage amplifiers, direct amplification of the error signal does not provide sufficient bandwidth to lock the remote laser tightly to the link output. Therefore, an alternative feedback scheme shown in Figure 5.3(b) is developed for the remote synchronization. Here, the BOC voltage is processed by a PI controller and separated in two paths to optimize the slow and fast feedback control on the remote laser's repetition rate independently. The first path is sampled by a DAQ card and used for generating a DC offset voltage to compensate slow timing drifts upon amplification. The second path remains unamplified to maintain a good phase margin for high locking bandwidths when correcting the fast timing jitter between the two lasers. A home-built voltage adder recombines the two paths to drive the PZT mounted on an intracavity mirror of the

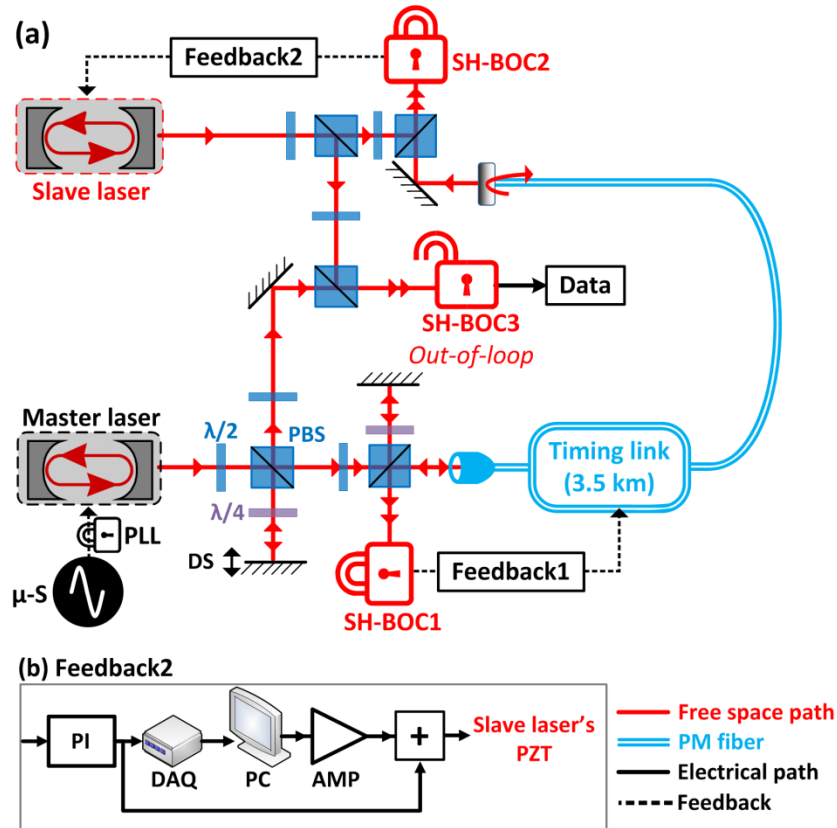


**Figure 5.3: Experimental setup for remote laser synchronization.**

(a) Main schematic of the experiment. (b) Feedback control scheme used for the remote laser locking via SH-BOC2.  $\mu$ -S: microwave source; PLL: phase-locked-loop;  $\lambda/2$ : half-wave plate,  $\lambda/4$ : quarter-wave plate; DS: delay stage; PI: PI servo controller; DAQ: data-acquisition card; AMP: electronic amplifier, +: home-built voltage adder.

remote laser. When the feedback controls of the link stabilization and the remote laser synchronization are activated, the original pulse trains of the master and remote laser are launched into a free-running detector (SH-BOC3) to measure their residual out-of-loop timing jitter.

To examine the influence of the link stability on the remote-laser synchronization, two sets of experimental results are recorded by the free-running SH-BOC3 as shown in Figure 5.4. The black curves are the results achieved when the timing link is stabilized using the traditional feedback scheme described in Section 4.2, whereas the results shown in red are obtained with the improved feedback scheme discussed in Section 4.4.1. As can be seen in Figure 5.4(a), the out-of-loop timing drift between the two lasers shows more than one order of magnitude improvement (i.e., a decrease from 2.3 fs RMS down to 94 as RMS over 44 h) when the system is operated with the improved feedback scheme including the link power stabilization. The inset in Figure 5.4(a) is closer look to the improved residual drift having a peak-to-peak timing deviation of only 400 as. Figure 5.4(b) and (c) show the compensated link delay fluctuations and the corrected frequency difference between the lasers. During the complete duration of the measurements, SH-BOC2 corrects about 350-Hz frequency mismatch of the slave laser's repetition rate via its intracavity PZT mirror in both cases.

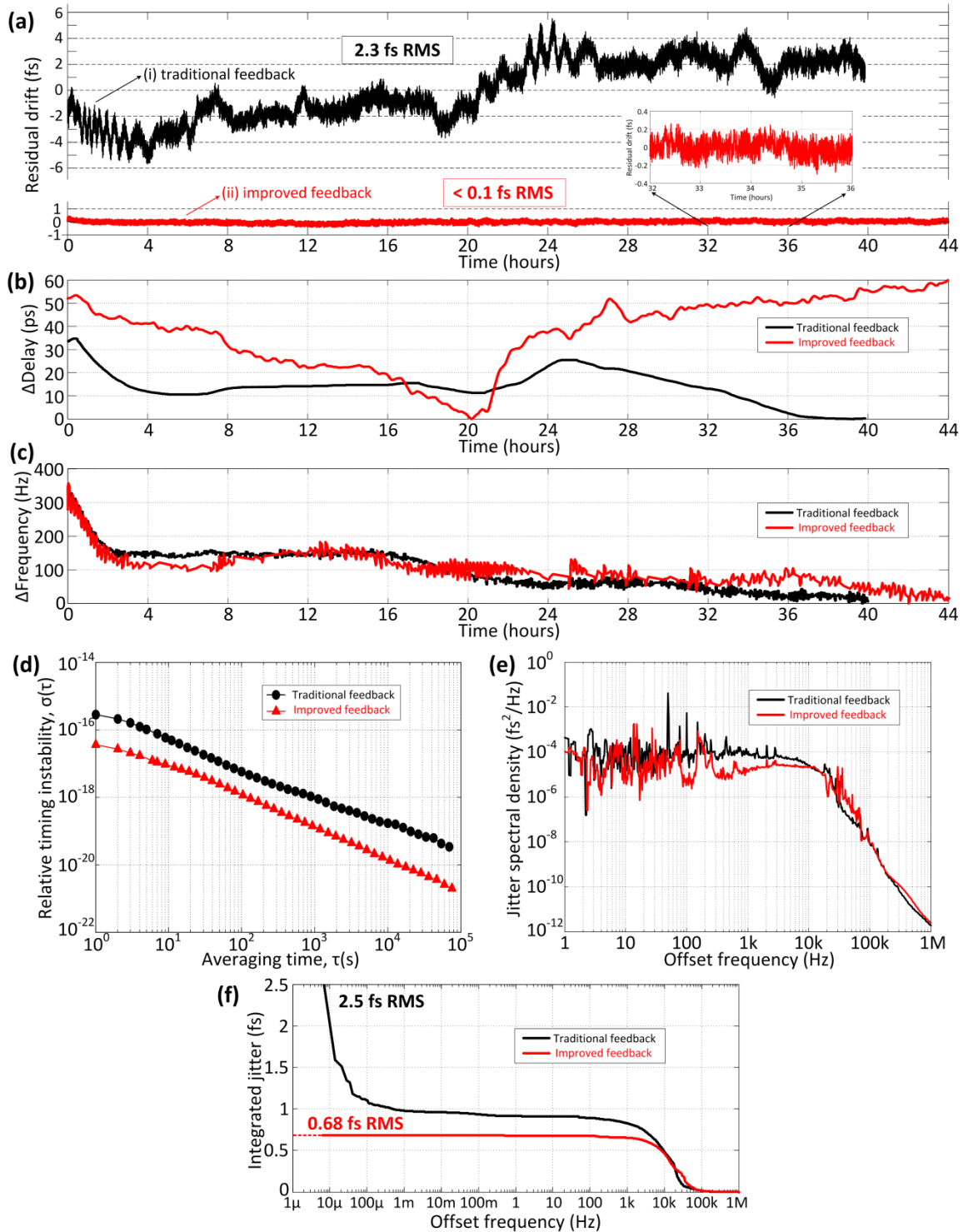


**Figure 5.4: Experimental results of the remote laser synchronization.**

(a) Out-of-loop timing drift below 1 Hz. (b) Compensated link drifts ( $\Delta$  Delay) by the motorized delays. (c) Corrected frequency mismatch ( $\Delta$  Frequency) of the slave laser. (d) Relative timing instability between the lasers. (e) Out-of-loop jitter spectral density. (f) Integrated timing jitter from 6.3  $\mu\text{Hz}$  to 1 MHz. Two sets of experimental data are recorded; black curves obtained with the traditional feedback and red curves obtained with the improved feedback for the link stabilization.

Furthermore, the improved feedback compensates for more timing drift in the link (60 ps) than the traditional feedback (25 ps), and yet it achieves far better long-term performance. This is also clearly visible from the relative timing instability in Figure 5.4(d). The improved feedback scheme achieves a remote synchronization with a record-low instability of  $3.5 \times 10^{-17}$  in 1-s decreasing to  $1 \times 10^{-20}$  in less than 3 h of averaging time.

The biggest limitation in high-frequency noise suppression is the operational PZT bandwidth of the slave laser which determines the fastest noise source that can be corrected by the feedback system. In our system, we are able to achieve remote-locking with up to 10-kHz locking bandwidth. If the feedback gain is further increased, the PZT resonance of the slave laser amplifies the noise at this frequency immensely and causes a large timing jitter. To circumvent this issue, we build a band-stop filter operating around 20 kHz and filter the PI controller output applied to the slaver laser's PZT. Figure 5.3(e) shows the out-of-loop timing jitter spectral density above 1 Hz between the two remotely synchronized mode-locked lasers. The black curve is obtained when there is no filtering at the output of PI controller; whereas the red curve corresponds to the result achieved with the band stop filter providing better noise suppression below 20 kHz offset frequency. Lastly, the complete integrated jitter of the two experiments is compared in Figure 5.4(f). The band-stop filter improves the high-frequency performance above 100 Hz from 0.90 fs to 0.67 fs. For offset frequencies smaller than 1 kHz, the improved feedback scheme (red curve) successfully suppresses all the noise sources down to a record low timing jitter of 200 as RMS, whereas the traditional system largely suffers from daily environmental fluctuations ( $<100 \mu\text{Hz}$ ) and delivers a total timing jitter of 2.5 fs RMS.

### 5.3 JITTER ANALYSIS OF THE TIMING DISTRIBUTION SYSTEM

As the red curve in Figure 5.4(f) indicates, the main contribution to the integrated timing originates from the noise above 1-kHz offset frequency. Therefore, in this section we investigate the high frequency noise sources of our timing distribution system with a comprehensive feedback loop analysis. In the experiments presented in this section, we use a home-built slave oscillator which is a titanium-sapphire (Ti:sa) Kerr-lens mode-locked laser operating at 800-nm center wavelength and 1.0833-GHz repetition rate.

#### 5.3.1 TIMING JITTER CHARACTERIZATION OF THE SLAVE LASER

As depicted in Figure 5.5(a), the Ti:sa laser is built as a ring cavity with two pairs of broadband dispersion-matched double-chirped mirrors (DCMs) which follow the design of our earlier work [102]. The Ti:sa crystal is placed at Brewster angle between the two dispersion matched concave DCMs with a radius of curvature of 25 mm. A 0.7-mm BaF<sub>2</sub> plate is used to compensate the intra-cavity dispersion. The output coupler is a BaF<sub>2</sub> wedge with a thickness of 1.43 – 1.77 mm which is

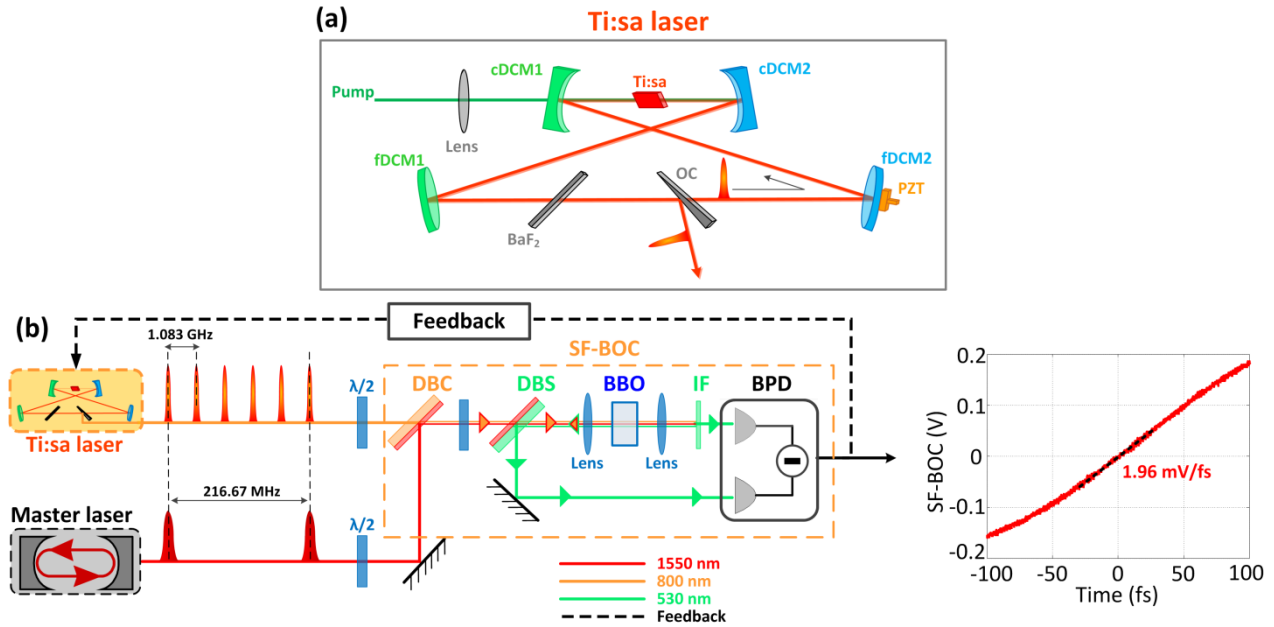


**Figure 5.5: Slave Ti:sa laser and its jitter characterization setup.**

(a) Schematic of the Kerr-lens mode-locked Ti:sa laser. (b) Experimental setup for characterizing the timing jitter of the Ti:sa laser. The right panel shows the measured SF-BOC response. cDCM: concave double-chirped mirror; fDCM: flat DCM; Ti:sa: titanium-sapphire crystal; BaF<sub>2</sub>: barium fluoride plate; OC: output coupler;  $\lambda/2$ : half-wave plate; DBC: dichroic beam combiner; DBS: dichroic beam splitter; BBO: beta barium borate crystal; IF: interference filter at 530 nm; BPD: balanced photodetector.

located in between the dispersion-matched flat DCMs to fine-tune the intra-cavity dispersion. With 6-W pump power at 532 nm and 4% output coupling ratio, the Ti:sa laser yields 650-mW average output power.

Ti:sa based laser systems are widely used in time and optical frequency transfer applications such as FEL synchronization, pump-probe experiments and clock comparison. Therefore, their jitter characterization holds a great importance to anticipate the temporal resolution of the complete system. By utilizing the low noise properties of the master laser presented in Section 3.1, we characterize the inherent timing jitter of our Ti:sa laser using the BOC method [85]. As displayed in Figure 5.5(b), the outputs of these two lasers are combined by a dichroic beam combiner, and then sent into the sum-frequency BOC (SF-BOC). Optical cross-correlation between the input pulses is realized with type-I sum-frequency generation between 800-nm and 1550-nm center wavelengths in a beta barium borate (BBO) crystal. The right panel in Figure 5.5(b) shows the voltage response of the SF-BOC. The mean value of the timing sensitivity is 1.96 mV/fs from five consecutive measurements resulting in a standard deviation of  $\pm 0.05$  mV/fs due to slope uncertainty.

Figure 5.6 shows the jitter characterization results of the Ti:sa laser from 1 kHz to 45 MHz (high-frequency limit is due to the BPD bandwidth). The electronic noise of the SF-BOC is measured when there is no input light on the device, whereas the shot noise limit is calculated from the photodetec-

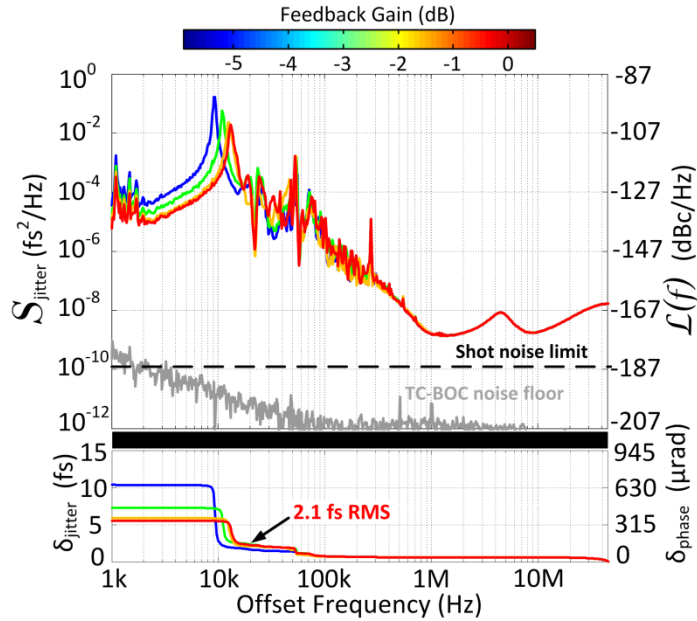


**Figure 5.6: Timing jitter characterization results of the Ti:sa laser.**

Left axes: timing jitter spectral density  $S_{\text{jitter}}$  and its integrated jitter  $\delta_{\text{jitter}}$  for different feedback gains. The color map on the top indicates the feedback gain value. Right axes: equivalent single-sideband (SSB) phase noise  $\mathcal{L}(f)$  and its integrated phase error  $\delta_{\text{phase}}$  scaled to 10-GHz carrier frequency. Figure is taken from our article [103].

ted voltages of the BPD (for details refer to Appendix A.1). The gray curve shows the detector noise floor of the SF-BOC which is below  $10^{-11}$   $\text{fs}^2/\text{Hz}$  for offset frequencies higher than 10 kHz. To ensure jitter characterization at the zero crossing of the SF-BOC, we measure the sum-frequency power with the individual photodetectors of the BPD each time when the lasers are locked. Both photodetectors read 0.15 V resulting in a measurement uncertainty of  $1.25 \times 10^{-10}$   $\text{fs}^2/\text{Hz}$  due to shot-noise (black dashed line in Figure 5.6) which confirms both balanced detection and broad-range shot-noise limited measurement.

The timing jitter spectral density of the Ti:sa laser is measured for different feedback gains. Ideally, one has to apply as low feedback gain as possible to decrease the locking bandwidth and reveal the laser's inherent jitter for small offset frequencies. Here, we are able to decrease our feedback gain by  $\sim 5$  dB (see red and blue curves in Figure 5.6). Beyond this point, the SF-BOC's linear range ( $\sim 200$  fs, as can be inferred from Figure 5.5(b)) is not sufficient to keep the two lasers locked due to the jitter caused by the acoustic and environmental disturbances on the Ti:sa laser cavity. Note that the Ti:sa laser has only a plastic cover; a more sophisticated acoustic insulation could decrease its environmental sensitivity. Nonetheless, we are able to resolve the laser's inherent jitter from 20 kHz to 45 MHz as all curves in Figure 5.6 overlap with each other in this frequency range. The integration of each spectrum results in  $\sim 2.1$ -fs RMS timing jitter for 20 kHz – 45 MHz, which is only 130- $\mu\text{rad}$  phase error for a 10-GHz carrier. Below 20 kHz, each measured spectrum

has a distinct peak value whose magnitude and frequency depend on the applied feedback gain. Therefore, the total integrated jitter for the complete offset frequency range varies from 5.5 fs (red curve) to 10.4 fs (blue curve).

To investigate the peaks observed in the jitter spectra and identify individual noise contributions of the setup elements, we utilize the feedback model for BOC-based laser synchronization developed in Section 3.1 (refer to Figure 3.2 for the feedback flow diagram). According to this model, the average jitter spectral density between the two lasers detected by the SF-BOC is given as:

$$\overline{J}_O^2 = \left| \frac{1}{1+H} \right|^2 (\overline{J}_M^2 + \overline{J}_S^2) + \left| \frac{H}{1+H} \right|^2 \overline{J}_N^2 \quad (5.7)$$

where  $J_M$  and  $J_S$  are the free-running jitter of the master and the slave laser,  $J_N$  is the electronic noise jitter term and  $H=H_{BOC}H_{BPD}H_{PI}H_{PZT}$  is the total transfer function of the SF-BOC lock (for detailed definitions refer to Appendix A.1). As Equation (5.7) specifies, there are three contributions to the output jitter of the SF-BOC: the free-running jitters of the master and the slave laser, and the electronic noise jitter of the system. Since the master laser exhibits fairly low noise ( $< 0.17$  fs RMS above 10 kHz, see Figure 3.4(b)) and the measurement is shot-noise limited (i.e.,  $J_N$  is insignificant), the dominant noise factor at the output of the SF-BOC is expected to be the slave laser's inherent jitter that is transferred to the SF-BOC output by  $|1/(1+H)|^2$ . Figure 5.7(a) and (b) show the calculated coefficients  $|1/(1+H)|^2$  and  $|H/(1+H)|^2$ , respectively using the transfer functions of the setup elements and the experimental parameters summarized in Table A.3. Please note that here we use the same feedback gain values as in the measurement results shown in Figure 5.6.

The transfer coefficients indicate that the inherent timing jitter of each laser is highly suppressed by the feedback loop for offset frequencies below 5 kHz (Figure 5.7(a)), whereas the electronic noise jitter is entirely carried to the output (Figure 5.7(b)). More remarkably, both of the transfer coefficients exhibit peak values above unity gain around the locking bandwidth which shift with the varied feedback gain. Therefore,  $J_M$ ,  $J_S$  and  $J_N$  are amplified at these offset frequencies, which clarifies the jitter peaks observed in the experimental results and their behavior in response to the applied feedback gain (see Figure 5.6). Furthermore, using Equation (5.7) we can calculate the free-running jitter of the Ti:sa laser as:

$$\overline{J}_S^2 = |1+H|^2 \overline{J}_O^2 - \overline{J}_M^2 - |H|^2 \overline{J}_N^2 \quad (5.8)$$

In Figure 5.7(c), we compare the calculated free-running jitter of the Ti:sa laser (gray curve) and the measured jitter between the two lasers at 0-dB feedback gain (identical to the red curve in Figure 5.6). As both curves nicely overlap with each other for offset frequencies larger than 20 kHz, the simulation result confirms the validity of our argument earlier that the dominant jitter contribution at the output of the SF-BOC stems from the slave Ti:sa laser. Since the feedback loop

obscures the noise between the master and the slave laser for frequencies lower than the locking bandwidth, the free-running jitter of the Ti:sa laser cannot be resolved experimentally below 20 kHz. However, thanks to our feedback model we estimate a total free-running jitter of 1.3 ps RMS integrated from 100 Hz to 1 MHz.

Time and optical frequency transfer applications mostly depend on the stable transmission of the master signal to the remote lasers using long optical fibers. Therefore, the following section discusses the experimental and simulation results on the remote synchronization of the Ti:sa laser using the timing link network presented in Section 4.4.

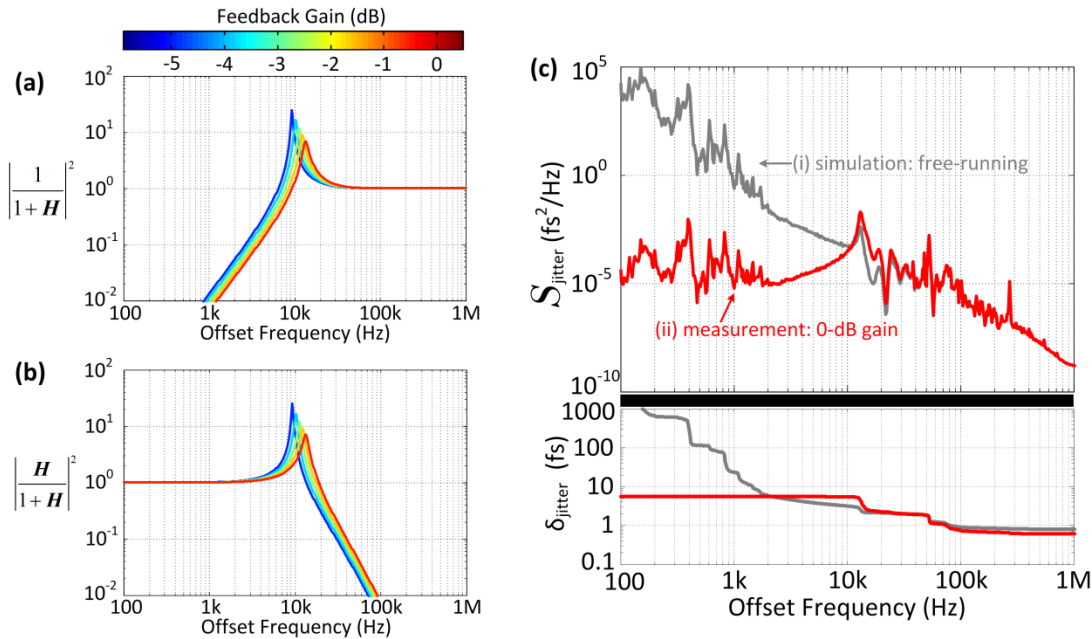


**Figure 5.7: Simulation results of the Ti:sa laser jitter characterization.**

(a) Transfer coefficient  $|1/(1+H)|^2$  of the master and slave laser's inherent jitter. (b) Transfer coefficient  $|H/(1+H)|^2$  of the electronic noise jitter. The color map on the top indicates the feedback gain values used in (a) and (b). (c) (i) Calculated free-running jitter of the Ti:sa laser using Equation (5.8) and (ii) measured jitter between the master and slave laser at 0-dB gain. Integrated jitter is shown on a logarithmic scale. Figure is taken from our article [103].

### 5.3.2 SYNCHRONIZATION OF THE SLAVE LASER ON A TIMING LINK NETWORK

Figure 5.8 shows the experimental setup built for the Ti:sa laser synchronization on the 4.7-km timing link network. The timing of the two fiber links is stabilized by PNS-BOCs using the feedback scheme described in Section 4.4.1. The Ti:sa laser is placed at the output location of the timing links. As the master laser and Ti:sa laser operate at different central wavelengths, two SF-BOCs are constructed between each link output and the Ti:sa laser output. SF-BOC1 synchronizes the Ti:sa laser to the link 1 output by tuning the repetition rate via its intracavity PZT mirror. To improve the phase margin of the remote synchronization and achieve higher locking bandwidth, the feedback scheme described in Figure 5.3(b) is employed between the SF-BOC1 and the Ti:sa laser.



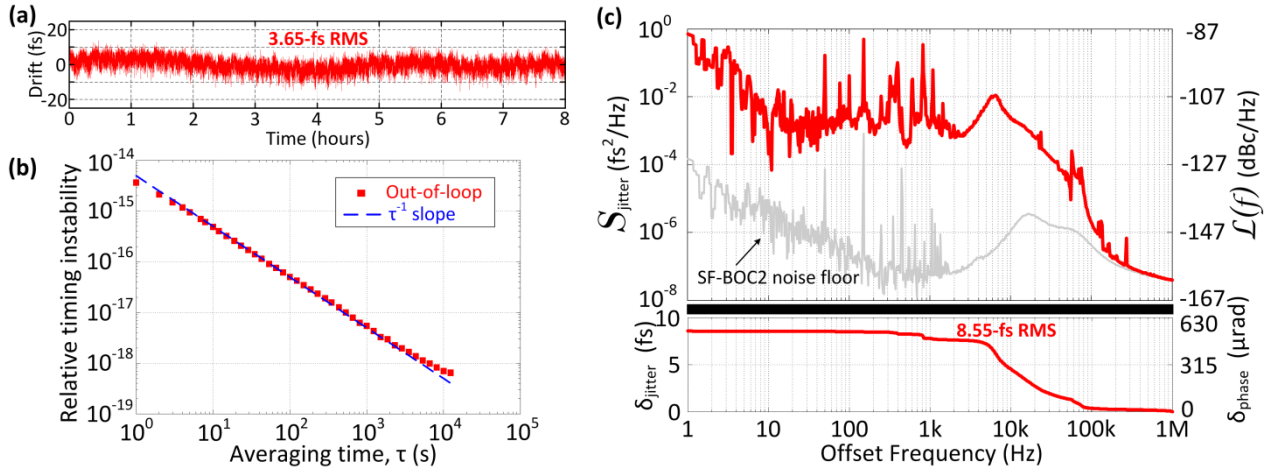


**Figure 5.9: Experimental results of the remote Ti:sa laser synchronization.**

(a) Out-of-loop timing drift below 1 Hz. (b) Calculated relative timing instability from the drift data. (c) Out-of-loop jitter spectral density  $S_{\text{jitter}}$  and its integrated jitter  $\delta_{\text{jitter}}$ ; right axes: equivalent SSB phase noise  $\mathcal{L}(f)$  and its integrated phase  $\delta_{\text{phase}}$  scaled to a 10-GHz carrier frequency. Figure is reproduced from our article [103].

fluctuations and acoustical vibrations. Therefore, an efficient isolation of the slave laser cavity from the environment is a prerequisite for a long-term stable timing distribution system.

Timing jitter spectral density for offset frequencies larger than 1 Hz is measured with a baseband analyzer which Fourier transforms the SF-BOC2 output. The red curve in Figure 5.9(c) shows the out-of-loop jitter between the remotely synchronized Ti:sa laser and timing link 2 output. The integrated jitter for 1 Hz – 1 MHz is 8.55 fs RMS corresponding to a phase error of 0.5 mrad for a 10-GHz carrier. As there are four BOCs and numerous locking elements used in this experiment, a comprehensive feedback loop analysis is pursued next to identify the factors influencing the observed timing jitter above 1 Hz offset frequency.

Figure 5.10 shows the feedback flow diagrams of each BOC-based timing measurement. The feedback models of the timing links in Figure 5.10(a) and (b) are identical to the one discussed in Section 4.3.4; except that the transfer functions  $H_{LR}$  and  $H_{LF}$  related with the fiber link nonlinearities are omitted for simplicity since the contribution of these effects are suppressed to below 0.2-fs RMS with the improved feedback scheme.

The feedback flow for the remote synchronization of the Ti:sa laser in Figure 5.10(c) is quite similar to the one for BOC-based laser synchronization discussed in Section 3.1. However, this time we have to consider two additional jitter sources: (i) environmental jitter  $J_{E,L1}$  and (ii) compensation jitter of timing link 1  $J_{F,L1}$  beside the inherent jitter of the master and the slave laser. Then again, one-way link delay must be applied to the inherent jitter of the master laser and to the link compensation jitter because they are actuated at the link input location.

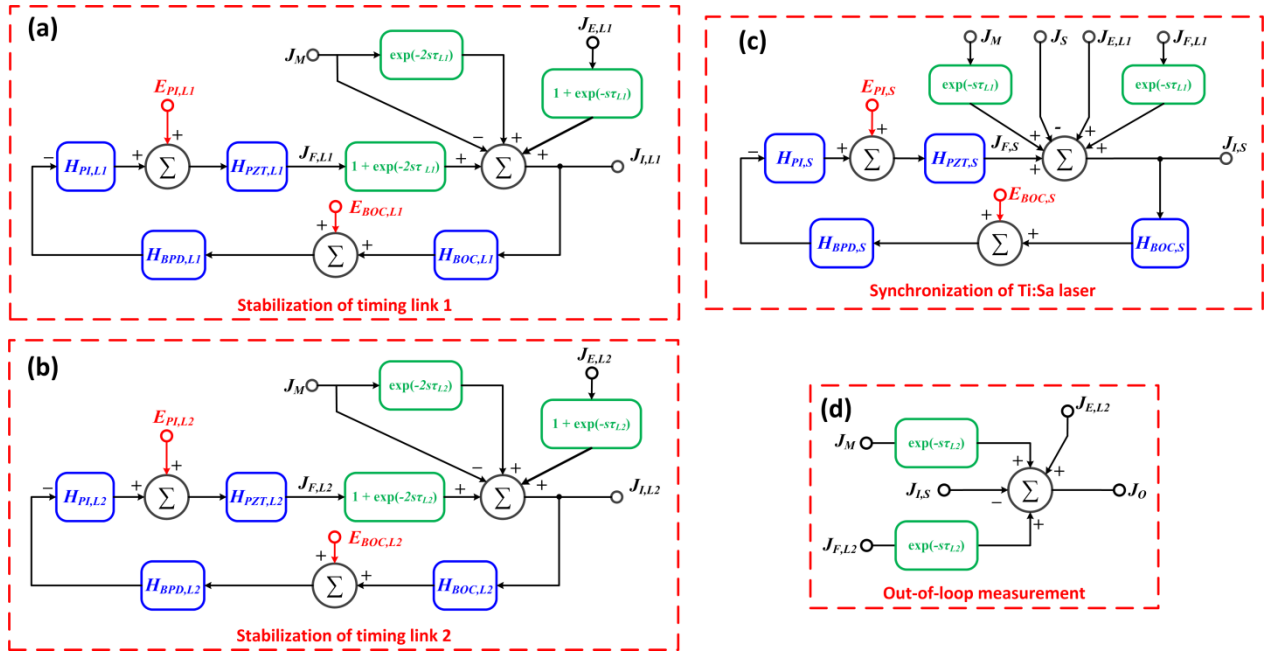


**Figure 5.10: Feedback model for the remote Ti:sa laser synchronization.**

Feedback flow diagrams in (a) stabilization of timing link 1 (b) stabilization of timing link 2, (c) remote synchronization of the Ti:sa laser via timing link 1, and (d) out-of-loop jitter measurement between the Ti:sa laser and timing link 2.  $J_E$ : total environmental jitter imposed on the link for one-way travel;  $J_I$ : timing jitter detected by the in-loop BOC;  $J_F$ : equivalent jitter generated by the feedback loop to maintain the lock;  $J_O$ : out-of-loop jitter between the Ti:sa laser and timing link 2 output;  $\tau$ : one-way fiber link travel time,  $s=j\omega$ : complex frequency. Subscripts  $L1$ ,  $L2$ , and  $S$  after each abbreviation refer to timing link 1, timing link 2 and the Ti:sa laser, respectively. Figure is reproduced from our article [103].

Starting with the feedback model of timing link 1 (Figure 5.10(a)) we get:

$$J_{I,L1} = J_M[-1 + \exp(-2s\tau_{L1})] + J_{F,L1}[1 + \exp(-2s\tau_{L1})] + J_{E,L1}[1 + \exp(-s\tau_{L1})] \quad (5.9)$$

$$\text{with } J_{F,L1} = [-(J_{I,L1}H_{BOC,L1} + E_{BOC,L1})H_{BPD,L1}H_{PI,L1} + E_{PI,L1}]H_{PZT,L1}$$

Similarly, from the stabilization of timing link 2 (Figure 5.10(b)):

$$J_{I,L2} = J_M[-1 + \exp(-2s\tau_{L2})] + J_{F,L2}[1 + \exp(-2s\tau_{L2})] + J_{E,L2}[1 + \exp(-s\tau_{L2})] \quad (5.10)$$

$$\text{with } J_{F,L2} = [-(J_{I,L2}H_{BOC,L2} + E_{BOC,L2})H_{BPD,L2}H_{PI,L2} + E_{PI,L2}]H_{PZT,L2}$$

The synchronization of the Ti:sa laser yields ((Figure 5.10(c)):

$$J_{I,S} = J_M \exp(-s\tau_{L1}) + J_{F,L1} \exp(-s\tau_{L1}) + J_{E,L1} - J_S + J_{F,S} \quad (5.11)$$

$$\text{with } J_{F,S} = [-(J_{I,S}H_{BOC,S} + E_{BOC,S})H_{BPD,S}H_{PI,S} + E_{PI,S}]H_{PZT,S}$$

The out-of-loop measurement results in ((Figure 5.10(d)):

$$J_O = J_M \exp(-s\tau_{L2}) + J_{F,L2} \exp(-s\tau_{L2}) + J_{E,L2} - J_{I,S} \quad (5.12)$$

By using a similar notation as in Equations (3.2) and (3.3), we introduce the electronic noise jitter terms  $J_{N,i}$  and total transfer functions  $H_i$  of each BOC lock (for details refer to Appendix A.1):

$$J_{N,i} = -\frac{E_{BOC,i}}{H_{BOC,i}} + \frac{E_{PI,i}}{H_{BOC,i}H_{BPD,i}H_{PI,i}} \quad (5.13)$$

$$H_i = H_{BOC,i}H_{BPD,i}H_{PI,i}H_{PZT,i} \quad (5.14)$$

where the subscript  $i=L_1, L_2, S$  refer to the BOC locks of timing link 1, timing link 2 and the slave Ti:sa laser, respectively. Then the equivalent jitter terms generated by the feedback controls are simplified as:

$$J_{F,L1} = H_{L1}(-J_{I,L1} + J_{N,L1}) \quad (5.15)$$

$$J_{F,L2} = H_{L2}(-J_{I,L2} + J_{N,L2})$$

$$J_{F,S} = H_S(-J_{I,S} + J_{N,S})$$

Finally, the out-of-loop timing jitter of the complete system is obtained by solving Equations (5.9) – (5.15):

$$J_O = C_M J_M + C_S J_S + C_{E,L1} J_{E,L1} + C_{E,L2} J_{E,L2} + C_{N,S} J_{N,S} + C_{N,L1} J_{N,L1} + C_{N,L2} J_{N,L2} \quad (5.16)$$

There are seven different noise sources together with the transfer coefficients given below which determine their contribution to the out-of-loop timing jitter:

$$C_M = \frac{(1 + 2H_{L2}) \exp(-s\tau_{L2})}{1 + H_{L2}(1 + \exp(-2s\tau_{L2}))} - \frac{1}{1 + H_S} \frac{(1 + 2H_{L1}) \exp(-s\tau_{L1})}{1 + H_{L1}(1 + \exp(-2s\tau_{L1}))} \quad (5.17)$$

$$C_S = \frac{1}{1 + H_S} \quad (5.18)$$

$$C_{E,L1} = -\frac{1}{1 + H_S} \frac{1 + H_{L1}[1 - \exp(-s\tau_{L1})]}{1 + H_{L1}[1 + \exp(-2s\tau_{L1})]} \quad (5.19)$$

$$C_{E,L2} = \frac{1 + H_{L2}[1 - \exp(-s\tau_{L2})]}{1 + H_{L2}[1 + \exp(-2s\tau_{L2})]} \quad (5.20)$$

$$C_{N,S} = -\frac{H_S}{1 + H_S} \quad (5.21)$$

$$C_{N,L1} = -\frac{1}{1 + H_S} \frac{H_{L1} \exp(-s\tau_{L1})}{1 + H_{L1}[1 + \exp(-2s\tau_{L1})]} \quad (5.22)$$

$$C_{N,L2} = \frac{H_{L2} \exp(-s\tau_{L2})}{1 + H_{L2}[1 + \exp(-2s\tau_{L2})]} \quad (5.23)$$

Since these noise sources are uncorrelated, we can add them on a mean-squared basis to derive the average jitter spectral density at the output of the system:

$$\begin{aligned} \overline{J_O^2} = & |C_M|^2 \overline{J_M^2} + |C_S|^2 \overline{J_S^2} + |C_{E,L1}|^2 \overline{J_{E,L1}^2} + |C_{E,L2}|^2 \overline{J_{E,L2}^2} + |C_{N,S}|^2 \overline{J_{N,S}^2} \\ & + |C_{N,L1}|^2 \overline{J_{N,L1}^2} + |C_{N,L2}|^2 \overline{J_{N,L2}^2} \end{aligned} \quad (5.24)$$

During the experiment, we have observed that the measured out-of-loop jitter is highly sensitive to the feedback parameters of SF-BOC1 lock (i.e., synchronization of the Ti:sa laser to the output of timing link 1). With the help of our feedback model, we can provide evidence for this observation by calculating the transfer coefficients for varied SF-BOC1 feedback gain (Figure 5.11).

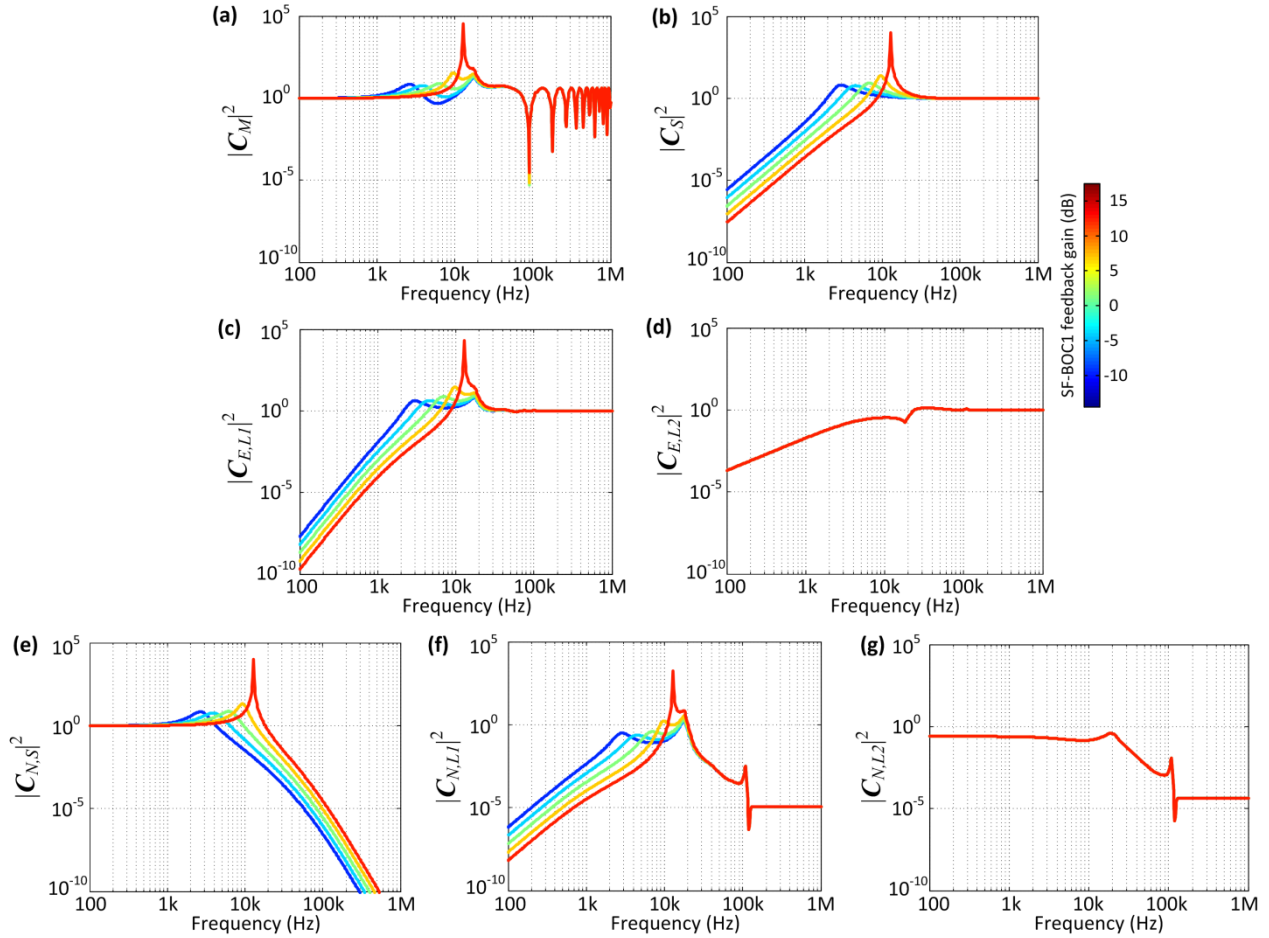


**Figure 5.11: Calculated transfer coefficients for varied SF-BOC1 feedback gain.**

Coefficients are given as following: (a) master laser's inherent jitter; (b) slave laser's inherent jitter; environmental noise imposed on (c) timing link 1 and (d) timing link 2; electronic feedback noise from (e) TC-BOC1 lock, (f) OC-BOC1 lock and (g) OC-BOC2 lock. The color map on the right-hand side is common for all figures. Graphs are calculated using the parameters given Table A.4. Figure is reproduced from our article [103].

Except for the environmental noise on timing link 2 and the electronic noise of its stabilization (Figure 5.11(d) and (g)), all other transfer coefficients are influenced by the synchronization of the Ti:sa laser. By increasing the SF-BOC1 feedback gain, we can suppress the excess noise coming from the inherent jitter of the Ti:sa laser, environmental disturbances imposed on timing link 1 and electronic jitter of its stabilization (see Figure 5.11(b), (c) and (f)). This is highly intuitive because higher feedback gain achieves ideally tighter synchronization between the link output and the Ti:sa laser. However, excess gain causes noise amplification peaks appearing around the PZT resonance of the Ti:sa laser (Figure 5.11(b), (c) and (f)) and introduces more electronic noise from SF-BOC1 lock (Figure 5.11(e)).

Figure 5.11(a) confirms once more that it is vital to have a master laser with low inherent noise, since it is transferred to the output entirely even with amplification around the PZT resonance of its intracavity mirror. Figure 5.11(d) expresses that the environmental jitter on timing link 2 is well

suppressed below 20 kHz. However, one has to pay attention to the electronic noise coming from its stabilization as it is transferred partially to the output by the feedback (Figure 5.11(g)).

Now that the transfer coefficients are calculated, we can determine the timing jitter spectral densities in Equation (5.24) and compare the results with the measured out-of-loop jitter. We obtain the environmental jitter imposed on the links ( $\overline{J_{E,L1}^2}$  and  $\overline{J_{E,L2}^2}$ ) experimentally by simply measuring their unlocked BOC output voltage with a baseband analyzer. Figure 5.12 shows the measurement results where the 3.5-km and 1.2-km links accumulate a total integrated jitter of 5.6 fs RMS and 2.2 fs RMS respectively for the offset frequency range of 100 Hz - 1 MHz.

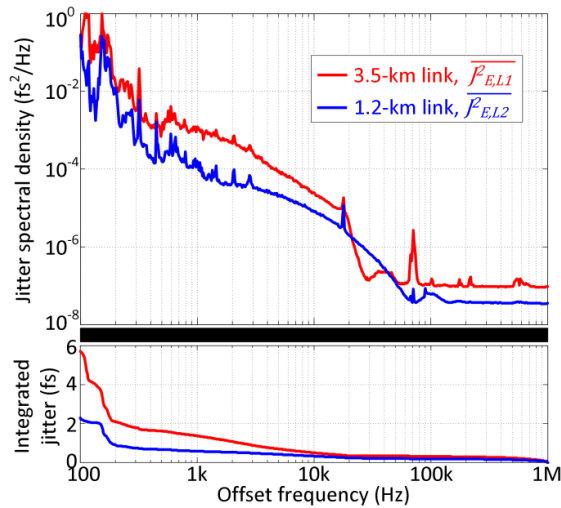


**Figure 5.12: Measured environmental noise imposed on the fiber links.**

Red curve:  $\overline{J_{E,L1}^2}$  measured by the free-running PNS-BOC1. Blue curve:  $\overline{J_{E,L2}^2}$  measured by the free-running PNS-BOC2.

We use the experimental data in Figure 3.4(b) for the master laser's inherent timing jitter ( $\overline{J_M^2}$ ), whereas we estimate the inherent timing jitter of the Ti:sa laser ( $\overline{J_S^2}$ ) by using Equation (5.8) as depicted with the gray curve in Figure 5.7(c). Lastly, we estimate the electronic jitter terms ( $\overline{J_{N,S}^2}$ ,  $\overline{J_{N,L1}^2}$  and  $\overline{J_{N,L2}^2}$ ) originating from the feedback controls based SF-BOC1, PNS-BOC1 and PNS-BOC2, respectively as explained in Appendix A.1.

Figure 5.13(a) presents the simulation results of the individual jitter contributions for offset frequencies 100 Hz to 1 MHz. Here, the low frequency limit is set by the free-running jitter of the master laser, which can be resolved down to 100 Hz. The inherent jitter of the Ti:sa laser is by far the largest noise factor with 8.19-fs integrated jitter (dark blue curve). This result points out that it is imperative to pay considerable attention to the low noise properties of the slave lasers before employing them in time and frequency transfer applications requiring higher precision. The inherent jitter of the master laser also plays an important role with 1.67-fs total jitter (light blue curve in Figure 5.13(a)). Its contribution becomes more noticeable for offset frequencies below 200

Hz, which justifies the stabilization of its repetition rate with a low-noise RF source. However, one has to maintain a relatively low locking bandwidth here, as the master laser surpasses the RF source in terms of low-noise performance for higher offset frequencies.

Large feedback gain in link stabilization helps to suppress the environmental noise on the fibers. However, one has to pay attention to the PZT resonances of the fiber stretchers. As can be seen from the dark green curve in Figure 5.13(a), the environmental jitter imposed on timing link 1 accumulates 1.5-fs jitter due to the excess noise around 18 kHz caused by its PZT resonance.

We can appreciate the advantage of low noise floors provided by the BOCs once more, since the least dominant jitter contributions in our system are the electronic noise coming from the feedback elements with a total integrated jitter below 0.3 fs.

Finally, the sum of all individual jitter spectral densities is compared with the out-of-loop measurement as shown in Figure 5.13(b). The experiment and the simulation agree very well with each other as the simulation estimates 8.49-fs RMS total integrated jitter, whereas the experiment shows 8.51 fs RMS for 100 Hz – 1 MHz. It even reveals many specific jitter structures such as electronic noise spurs below 2 kHz. However, there are some deviations between the two spectra for offset frequencies 5 kHz – 25 kHz. We suspect that they originate from the imperfect estimation of the PZT transfer function of the Ti:sa cavity mirror. The simulation results can be improved even further by measuring the PZT voltage response around its resonance. Note that above 200 kHz, the simulation result is obscured by the environmental noise and master laser jitter measurements which fall beyond the detector noise floor.

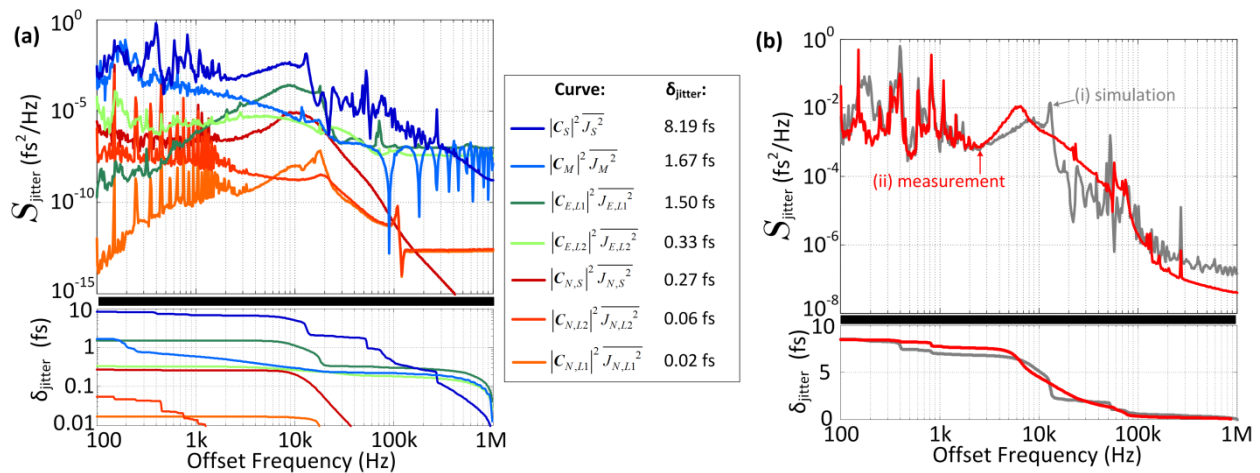


**Figure 5.13: Noise sources of the remote Ti:sa laser synchronization.**

(a) Simulation results of individual jitter contributions. The legend on the right shows the color code of the jitter spectral densities and their integrated jitter shown on a logarithmic scale. (b) Comparison between (i) the sum of all simulated jitter sources and (ii) the out-of-loop jitter measurement. Figure is taken from our article [103].

## 5.4 SYNCHRONOUS MODE-LOCKED LASER NETWORK

As discussed in Section 5.3, long- and short-term performance of a timing distribution system may be limited by the noise of the employed slave lasers even if perfect fiber link transmission is ensured. Building upon our knowledge and experience, we bring our timing distribution system one step further by constructing a synchronous mode-locked laser network delivering attosecond precision for an extended range of offset frequencies between 7  $\mu\text{Hz}$  and 1 kHz.

The mode-locked laser network is experimentally realized as described in Figure 5.14 where three mode-locked lasers are synchronized in a star network topology over two different timing-stabilized fiber links with 4.7-km total length. The timing signal of the master laser is delivered to the slave lasers with two independently stabilized fiber links, which have a relative total timing jitter 580 as RMS integrated from 7  $\mu\text{Hz}$  to 1 MHz as shown in Figure 4.17(a). The outputs of the timing links are used for the remote synchronization of two slave mode-locked lasers. Slave laser 1 (Origami-15 from OneFive GmbH) is identical to the master laser. A PNS-BOC for 1550-nm input pulses is built to synchronize slave laser 1 with the output of timing link 1.

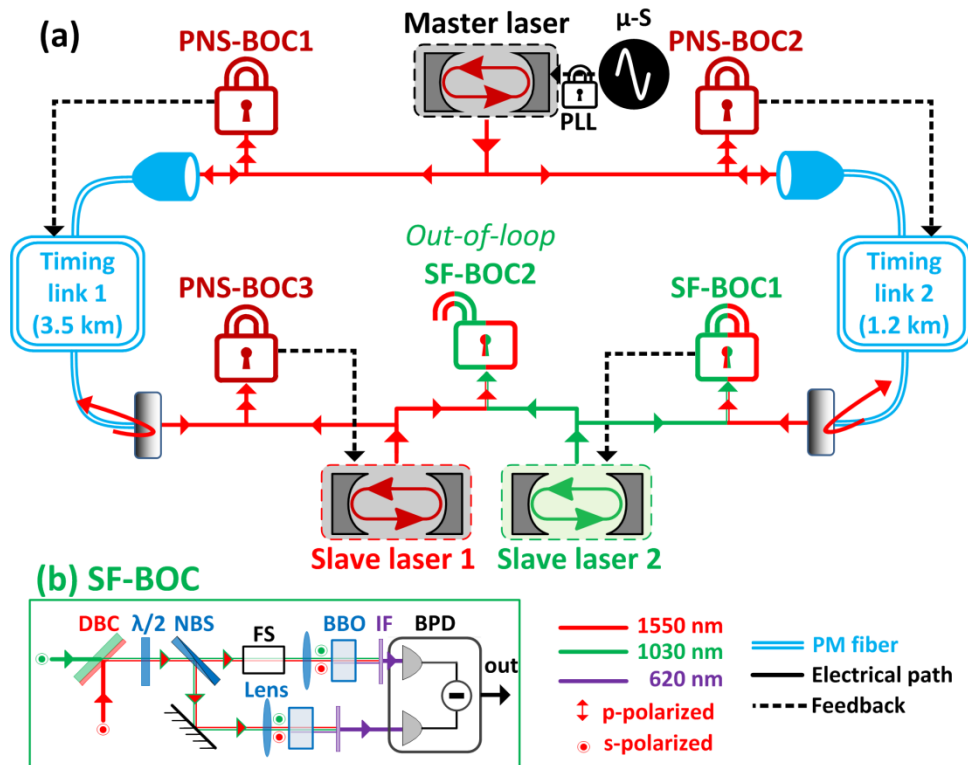


**Figure 5.14: Experimental setup for the synchronous mode-locked laser network.** (a) Layout of the experiment. (b) Elements of the SF-BOC built for 1550-nm and 1030-nm input pulse trains. DBC: dichroic beam combiner;  $\lambda/2$ : half-wave plate; NBS: neutral 50:50 beam splitter; FS: fused-silica plate; BBO: beta barium borate crystal; IF: interference filter at 620 nm; BPD: balanced photodetector.

Slave laser 2 (Origami-10 from OneFive GmbH), on the other hand, operates at 54.17-MHz repetition rate with an output optical spectrum centered at 1030 nm. To synchronize slave laser 2 to timing link 2 output, a type-I SF-BOC is built for input pulses of 1030-nm and 1554-nm center wavelengths using two BBO crystals as illustrated in Figure 5.14(b). The time delay difference between the two arms of SF-BOC is adjusted with a glass plate to maximize the timing sensitivity of balanced detection. A fraction of the output power from each slave laser is spared for an out-of-loop timing detector (SF-BOC2 in Figure 5.14(b)) to evaluate the timing precision of the synchronous laser network. Five independent measurements of SF-BOC2 timing sensitivity result in a mean value of 14.96 mV/fs with a measurement error of  $\pm 0.066$  mV/fs due to slope uncertainty.

The complete setup consumes a total space of two optical tables. The master laser, PNS-BOC1 and PNS-BOC2 are placed on the first optical table which is actively temperature stabilized and covered with an acoustically isolated enclosure as described in Section 3.2. The timing links are placed outside of the enclosure and exposed to environmental fluctuations in the laboratory. The link outputs connect to the second optical table where the slave lasers, PNS-BOC3, SF-BOC1 and SF-BOC2 are constructed in an optical enclosure without active temperature stabilization. Once all in-loop BOCs (PNS-BOC1-3 and SF-BOC1, symbolized with “closed lock symbols” in Figure 5.14(a)) and their feedback loops are employed, we use a manual delay stage to overlap the two pulse trains in time inside the free-running SF-BOC2 and measure their relative timing.

#### 5.4.1 TIMING DRIFT

The individual components of the timing links and their applied feedback controls are shown in Figure 4.15(c). As discussed in Section 4.2, detected timing error by the link-locking BOC is applied traditionally only to the fiber stretcher and the motorized delay to compensate for fast jitter and long-term drift, respectively (Feedback 1–2 in Figure 4.15(c)). Firstly, we stabilize our timing links with this traditional feedback scheme and synchronize the slave lasers to their output. Figure 5.15(a) shows the long-term stability measurements of the laser network with the traditional link stabilization detected by SF-BOC2. Even though one additional mode-locked laser is added to the system when compared with the setup in Figure 5.8, the residual out-of-loop drift is improved from 3.65 fs to 1.2 fs RMS over 16 h proving the superior environmental isolation of the two slave lasers in Figure 5.15. Nonetheless, the observed drift still undergoes quite noticeable fluctuations. As discussed in Section 4.3, this residual drift is attributed to the link power fluctuations caused by beam misalignments upon the movement of the free-space coupled motorized delays. Red and orange curve in Figure 5.15(a) show the optical power fluctuations of timing link 1 and 2 respectively measured after round-trip propagation. Over 16 h of measurement, the output power of timing link 1 exhibits an apparent drift of 4% peak-to-peak, whereas timing link 2 output is more

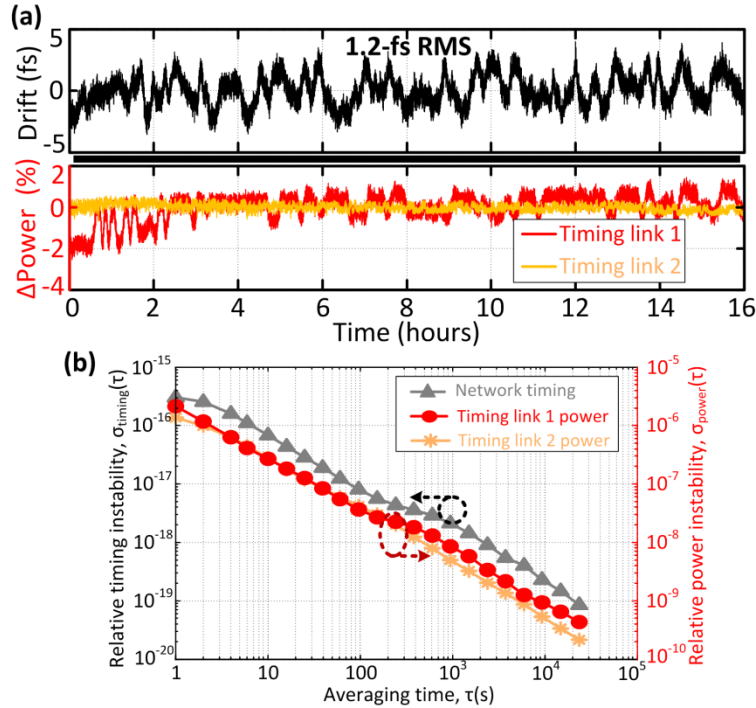


**Figure 5.15: Long-term stability measurements with traditional link stabilization.**

(a) Out-of-loop timing drift (black curve) of the laser network and detected power fluctuations ( $\Delta$  Power) of the timing links (red and orange curve) over 16 h. (b) Relative timing instability of the laser network (gray curve, scaled with left Y-axis), and relative power instability of the timing links (red and orange curve, scaled with right Y-axis) calculated from the data in (a) in terms of overlapping Allan deviation.

stable with less than 1% peak-to-peak power deviation. Even though detected power fluctuations are relatively small, the measured drift of the laser network shows a strong correlation especially with the power fluctuation of timing link 1. The correlation is even more obvious once we calculate the ADEVs of the relative timing- and power-instabilities using the drift and power fluctuation data (see Figure 5.15(b)). The slope of the network timing instability (gray curve) changes for averaging times longer than 200 s as a result of the relative power instability observed in timing link 1 (red curve). This proves once more the necessity of operational link power stabilization to proceed beyond the 1-fs resolution limit.

Figure 5.16 shows the long-term stability measurements of the synchronous mode-locked laser network when the 3<sup>rd</sup> feedback control on the EDFA's pump current is activated besides the fiber stretcher and motorized delay (see Figure 4.15(c)). Out-of-loop timing drift is decreased down to 0.6-fs RMS over 40 h of continuous measurement (black curve in Figure 5.16(a)) with no apparent long-term drift and power fluctuations. We suspect that the remaining drift originates from the uncompensated reference arms of the remote laser locks. This can be improved further if an active temperature stabilization is applied to the second optical table as well where the slave lasers and their BOCs are located.

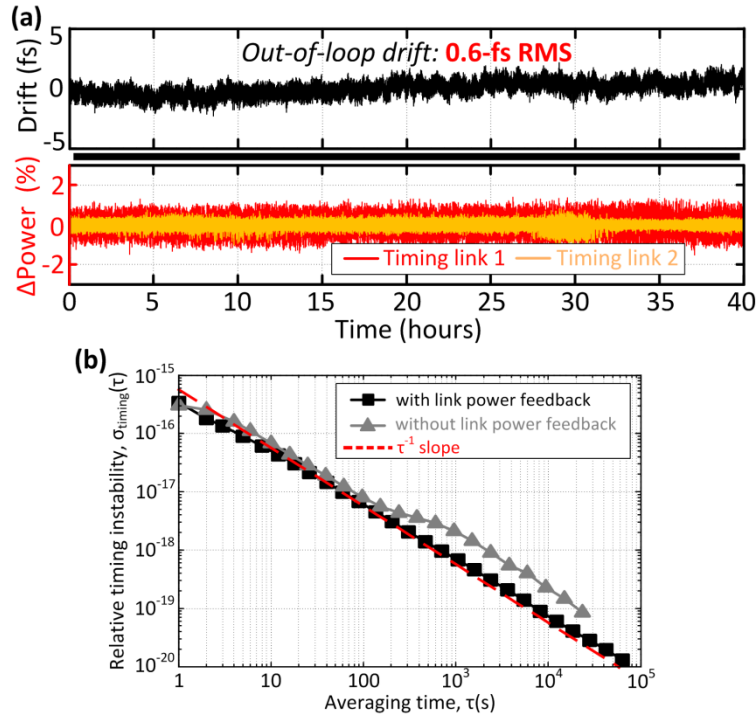


**Figure 5.16: Improved long-term stability with the suppression of link nonlinearities.**

(a) Out-of-loop timing drift (black curve) of the laser network and detected power fluctuations ( $\Delta$ Power) of the timing links (red and orange curve) over 40 h. (b) Relative timing instability of the laser network with and without the link power feedback on the EDFA pump current (black and gray curve, respectively).

Nevertheless, 0.6-fs RMS timing drift over 40 h corresponds to the lowest timing instability ever measured between two slave mode-locked lasers remotely synchronized to a common reference over multi-kilometer distance. Figure 5.16(b) shows the calculated ADEV (black curve) from the drift data in Figure 5.16(a). Relative timing instability of the mode-locked laser network is only  $5 \times 10^{-17}$  in 10-s averaging time ( $\tau$ ) and reaches  $1.2 \times 10^{-20}$  in 70000 s by following a deterministic  $\tau^{-1}$  slope (red dashed curve). When compared to the result with traditional link stabilization, there is a clear slope distinction especially for averaging times larger than 100 s.

#### 5.4.2 TIMING JITTER SPECTRAL DENSITY

Apart from determining the precision of the system on short time scales ( $<1$  s), timing jitter analysis holds a great importance to study the jitter contributions of the setup elements for further improvement. Timing jitter spectral density of the mode-locked laser network is measured with a baseband analyzer which Fourier-transforms the SF-BOC2 output above 1 Hz. The black curve in Figure 5.17 shows the out-of-loop jitter of the network when all five locks in Figure 5.14(a) are employed. If we exclude the power line spurs observed at the harmonics 50 Hz, the complete spectrum from 1 Hz to 1 MHz is below  $8 \times 10^{-4}$   $\text{fs}^2/\text{Hz}$  corresponding to a phase noise of only -118 dBc/Hz at 1 Hz offset frequency between two 10-GHz sources located 4.7-km far from each other.

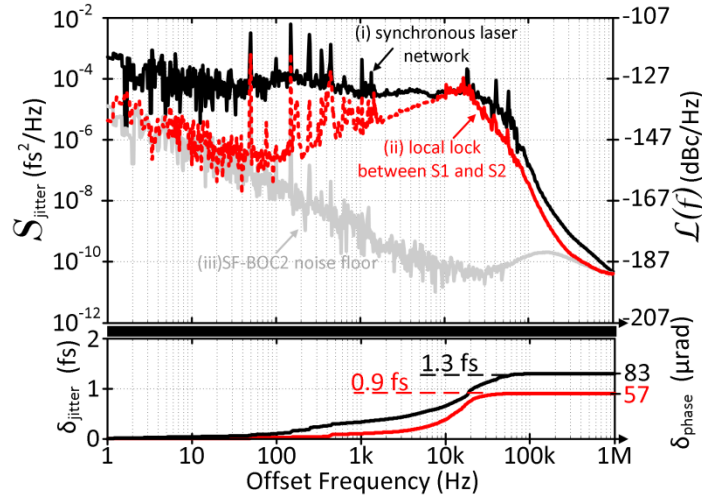


**Figure 5.17: Short-term stability measurements of the laser network.**

Left axes: Timing jitter spectral density  $S_{jitter}$  and its integrated jitter  $\delta_{jitter}$ ; right axes: equivalent single-sideband phase noise  $\mathcal{L}(f)$  and its integrated phase  $\delta_{phase}$  scaled at 10-GHz carrier frequency. (i) Synchronous laser network jitter measured by the free-running SF-BOC2; (ii) local jitter between slave laser 1 and 2 measured by in-loop SF-BOC2; (iii) noise floor of SF-BOC2.

Furthermore, the total integrated timing jitter of the network between 1 Hz and 1 MHz is only 1.3 fs ( $\pm 0.006$  fs) RMS corresponding to a phase error of 83  $\mu\text{rad}$  ( $\pm 0.4$   $\mu\text{rad}$ ) for a 10 GHz carrier frequency where the uncertainty in the measured values arises from the timing sensitivity error given in the previous section. To investigate the high frequency jitter limitations of the network, slave laser 1 and slave laser 2 are disengaged from their links and locally synchronized to each other using SF-BOC2. The red curve in Figure 5.17 shows the corresponding in-loop jitter spectral density which closely follows the network results for frequencies between 10 kHz and 1 MHz (less than 7 dB difference). As the in-loop detector obscures the noise between the slave lasers for frequencies lower than the locking bandwidth ( $< 10$  kHz), the local jitter spectral density shows larger deviation from the network results in this region (see the red dotted curve in Figure 5.17 for frequencies below 10 kHz). An out-of-loop measurement would even reveal higher amount of noise for the local timing jitter between the slave lasers below 10 kHz. Nevertheless, the integrated jitter is as high as 0.9 fs RMS pointing out the unsuppressed jitter of the slave lasers beyond the locking bandwidth as the prominent noise contribution.

In order to investigate the contribution of the slave lasers' jitter further and identify other noise sources in the system, we pursue a comprehensive feedback loop analysis of our laser network. The network consists of a master laser and two timing-stabilized fiber links which remotely synchronize two slave lasers to the master laser. Stabilization of the links and synchronization of the remote lasers are performed by BOC based locking schemes. The feedback flow diagrams are shown in Figure 5.18 which are adapted from our previous analysis in Section 5.3.2. Therefore, an interested



$$C_{S1} = \frac{1}{1 + H_{S1}} \quad (5.27)$$

$$C_{S2} = -\frac{1}{1 + H_{S2}} \quad (5.28)$$

$$C_{E,L1} = -\frac{1}{1 + H_{S1}} \frac{1 + H_{L1}[1 - \exp(-s\tau_{L1})]}{1 + H_{L1}[1 + \exp(-2s\tau_{L1})]} \quad (5.29)$$

$$C_{E,L2} = \frac{1}{1 + H_{S2}} \frac{1 + H_{L2}[1 - \exp(-s\tau_{L2})]}{1 + H_{L2}[1 + \exp(-2s\tau_{L2})]} \quad (5.30)$$

$$C_{N,S1} = -\frac{H_{S1}}{1 + H_{S1}} \quad (5.31)$$

$$C_{N,S2} = \frac{H_{S2}}{1 + H_{S2}} \quad (5.32)$$

$$C_{N,L1} = -\frac{\exp(-s\tau_{L1})}{1 + H_{S1}} \frac{H_{L1}}{1 + H_{L1}[1 + \exp(-2s\tau_{L1})]} \quad (5.33)$$

$$C_{N,L2} = \frac{\exp(-s\tau_{L2})}{1 + H_{S2}} \frac{H_{L2}}{1 + H_{L2}[1 + \exp(-2s\tau_{L2})]} \quad (5.34)$$

where the electronic noise jitter terms  $J_{Nj}$  and total transfer functions  $H_j$  of each BOC lock are defined as (for details refer to Appendix A.1):

$$J_{N,j} = -\frac{E_{BOC,j}}{H_{BOC,j}} + \frac{E_{PI,j}}{H_{BOC,j}H_{BPD,j}H_{PI,j}} \quad (5.35)$$

$$H_j = H_{BOC,j}H_{BPD,j}H_{PI,j}H_{PI,j} \quad (5.36)$$

for  $j=L1, L2, S1$  and  $S2$  referring to the specific BOC locks stabilizing timing link 1 and 2, and synchronizing slave laser 1 and 2, respectively. All jitter sources in Equation (5.25) have the units of  $s/\sqrt{\text{Hz}}$ . Since these noise sources are uncorrelated with each other, the average values of their cross products will be zero. Hence, the mean of the out-of-loop jitter spectral density (in units of  $s^2/\text{Hz}$ ) is:

$$\begin{aligned} \overline{J_O^2} = & |C_M|^2 \overline{J_M^2} + |C_{S1}|^2 \overline{J_{S1}^2} + |C_{S2}|^2 \overline{J_{S2}^2} + |C_{E,L1}|^2 \overline{J_{E,L1}^2} + |C_{E,L2}|^2 \overline{J_{E,L2}^2} + |C_{N,S1}|^2 \overline{J_{N,S1}^2} \\ & + |C_{N,S2}|^2 \overline{J_{N,S2}^2} + |C_{N,L1}|^2 \overline{J_{N,L1}^2} + |C_{N,L2}|^2 \overline{J_{N,L2}^2} \end{aligned} \quad (5.37)$$

All terms in Equation (5.37) can be either measured or calculated using experimental parameters. As the master laser and slave laser 1 are identical, we use the experimental data given in Figure 3.4(b) for both  $\overline{J_M^2}$  and  $\overline{J_{S1}^2}$  (i.e.  $\overline{J_M^2} = \overline{J_{S1}^2}$ ). We calculate the free running jitter of the slave laser 2 ( $\overline{J_{S2}^2}$ ) from the local synchronization measurement using Equation (5.8). As shown with the gray curve in Figure 5.19, slave laser 2 has an estimated free-running jitter of 330 fs RMS integrated from 100 Hz up to 1 MHz. Furthermore, we use the experimental results presented in Figure 5.12 for the environmental jitter imposed on the links  $\overline{J_{E,L1}^2}$  and  $\overline{J_{E,L2}^2}$ . Finally, we estimate  $J_{N,j}$  and  $H_j$  terms using transfer functions given in Appendix A.1 and experimental parameters in Table A.5.

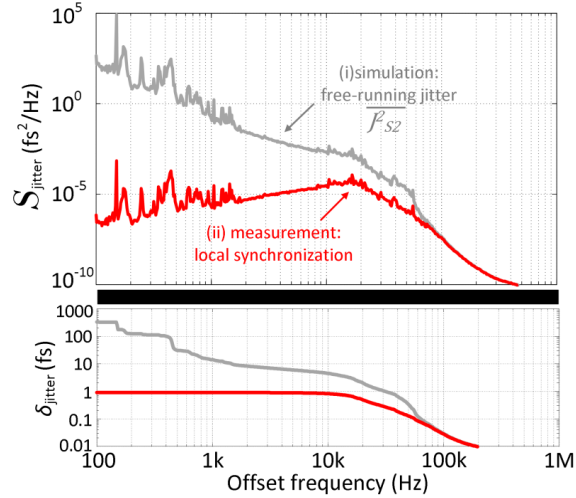


**Figure 5.19: Estimated free-running timing jitter of the slave laser 2.**

Free-running jitter (gray curve) is calculated from the local synchronization measurement (red curve) using Equation (5.8). Integrated jitter is shown on a logarithmic scale.

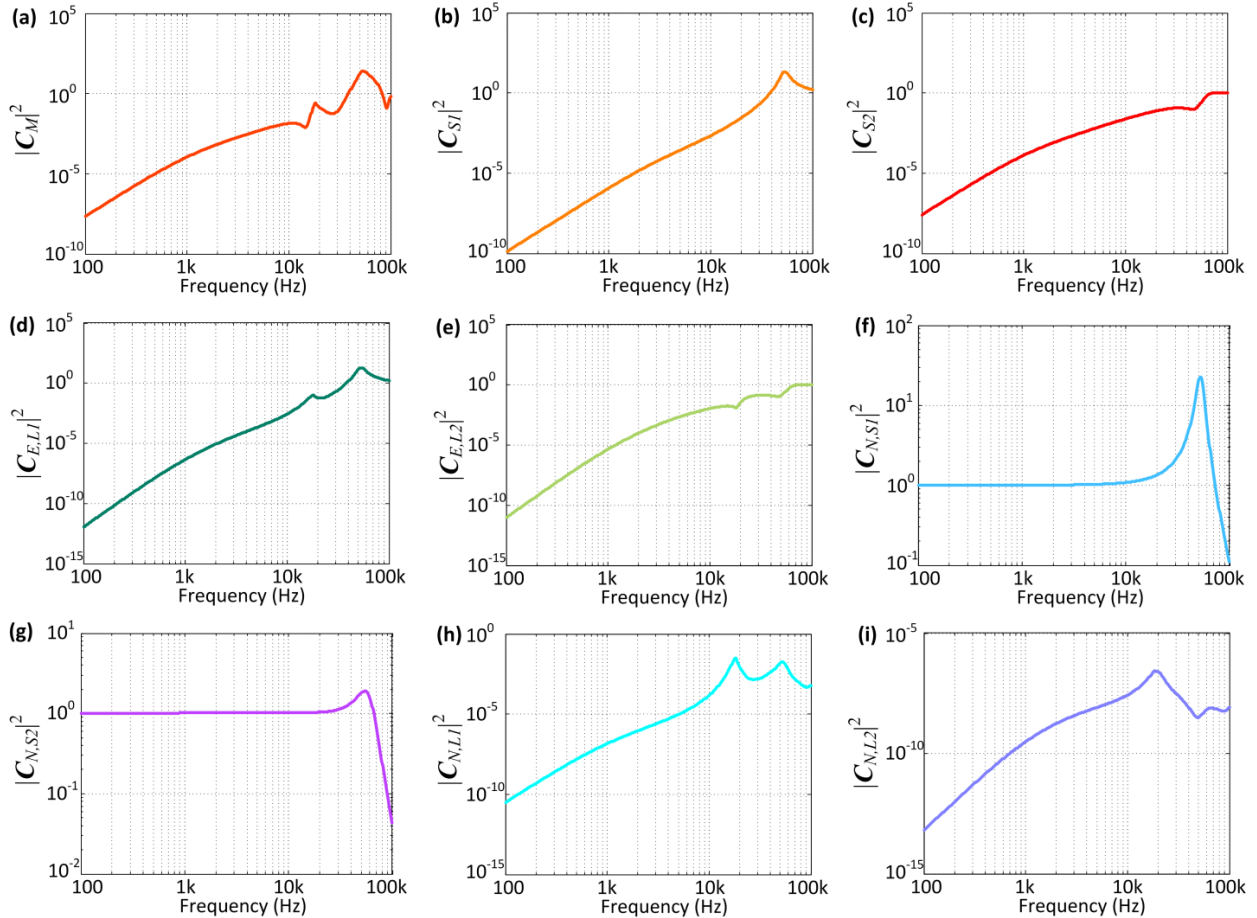


**Figure 5.20: Calculated jitter transfer coefficients of the laser network.**

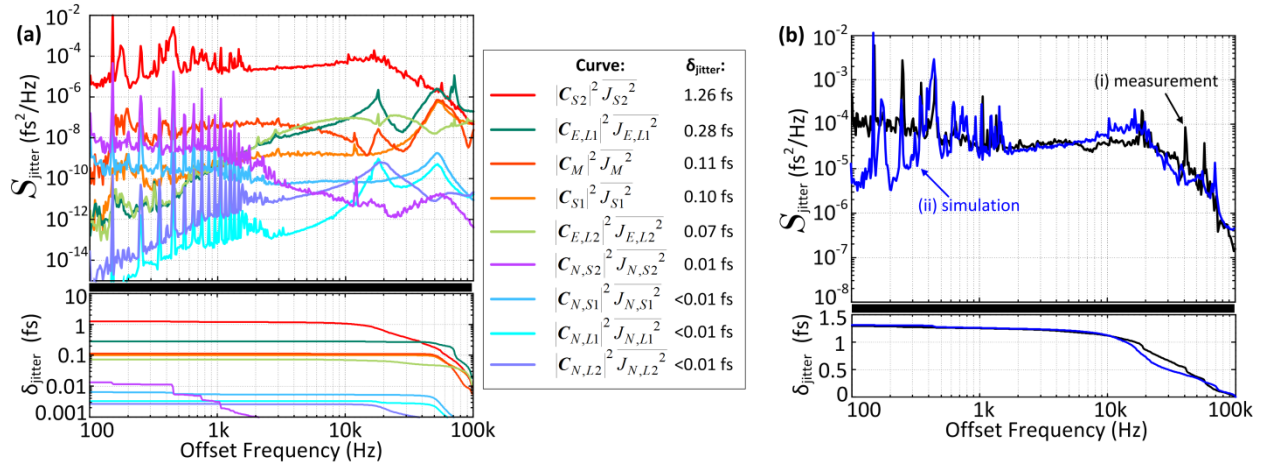
Transfer coefficients of (a) master laser’s inherent jitter; the inherent jitter of (b) slave laser 1 and (c) slave laser 2; environmental noise imposed on (d) timing link 1 and (e) timing link 2; (f) electronic feedback noise of remote laser locking (e) PNS-BOC3, (f) SF-BOC1, and link stabilizing (g) PNS-BOC1, (h) PNS-BOC2. The color of each curve is identical to the calculated individual jitter sources presented in Figure 5.21(a).

Figure 5.20 presents the calculated transfer coefficients of the all noise sources given in Equation (5.37). Unlike the case of a single laser synchronized to the timing link network (see Figure 5.11(a)), only a small fraction of the master laser's inherent jitter transferred to the network output in the low offset frequency regime due to the symmetry in the synchronization (see  $|C_M|^2$  in Figure 5.20(a)). This can be also inferred from the Equation (5.26) of  $C_M$  which would read zero if both of the links, the slave lasers and their locking feedback loops were identical. Similarly, all the other noise sources in the mode-locked laser network are highly suppressed in this frequency range, except the electronic noise of the two remote laser synchronizations (i.e., in Figure 5.20(f) and (g)) which are carried straight to the out-of-loop jitter by their feedback loops.

Figure 5.21(a) shows the simulation results of the jitter sources in Equation (5.37) at the output of SF-BOC2 using their calculated transfer coefficients given in Figure 5.20. The panel on the right provides the color map of the jitter spectral densities and their integrated jitter from 100 Hz to 100 kHz. Note that the lower limit for the offset frequency is set by the free-running jitter of the master laser which could be resolved down to 100 Hz, whereas higher frequency limit is given by the environmental jitter on the timing links which is smaller than the measurement noise floor for frequencies above 100 kHz.

As suspected from the local synchronization results shown in Figure 5.17, the prominent contribution to the observed out-of-loop jitter originates from the slave laser 2 and it dominates the complete jitter spectrum with 1.26-fs integrated jitter ( $|C_{S2}|^2 \overline{J_{S2}^2}$ , top red curve in Figure 5.21(a)). The environmental noise on timing link 1 and 2 ( $|C_{E,L1}|^2 \overline{J_{E,L1}^2}$ , dark green curve and  $|C_{E,L2}|^2 \overline{J_{E,L2}^2}$ , light green curve, respectively) are well suppressed by the feedback loops for offset frequencies below 10 kHz. However, one has to pay attention to the PZT resonances which makes the environmental jitter of timing link 1 the second largest noise source with 0.28-fs total jitter (see the jitter peak around 70-kHz of the dark green curve in Fig. 6(a)). The master laser ( $|C_M|^2 \overline{J_M^2}$ ) and the slave laser 1 ( $|C_{S1}|^2 \overline{J_{S1}^2}$ ) add only 0.11-fs and 0.10-fs integrated jitter to the network due to their low noise properties. Thanks to the noise floors provided by BOC locking schemes, the least dominant jitter contributions in the system are the four electronic noise jitter terms with total integrated jitter equal or less than to 0.1 fs.

Finally, we add all individual jitter spectral densities and compare the sum with the measured out-of-loop jitter spectral density of our synchronous laser network (see Figure 5.21(b)). Simulated jitter spectrum shows excellent agreement with the experiment and reveals many of the jitter structures observed in the measurement such as the servo bump around 20 kHz and electronic noise spurs below 1 kHz. The integration of the simulated jitter spectrum results in 1.31-fs total jitter agreeing quite well with experiment.



**Figure 5.21: Noise sources of the observed out-of-loop network jitter**

(a) Simulated individual jitter contributions. Subfigure on the right shows the color code of the jitter spectral densities and their integrated jitter from 100 Hz to 100 kHz. (b) (i) measured out-of-loop jitter, (ii) sum of all simulated jitter sources. Integrated jitter in (a) is shown in logarithmic scale.

Small deviations between the measurement and simulation exist especially for offset frequencies between 15 kHz and 40 kHz since this frequency range is highly influenced by the PZT resonances. The agreement between the simulation and the measurement could be improved even further with an experimental investigation of PZT resonance frequencies of the setup elements.

Figure 5.22 presents the timing jitter spectrum of the laser network for the complete measurement range from 7  $\mu$ Hz up to 1 MHz. The laser network exhibits a very low timing jitter in the attosecond regime (670 as) within the locking bandwidth of the system below 1 kHz. As indicated before, the prominent noise contribution stems from the offset frequencies larger than 1 kHz which is dominated by the inherent timing jitter of the slave lasers. By developing lower noise mode-locked lasers with faster repetition-rate-control systems, the high frequency performance of the synchronous laser network can also be promoted to the attosecond regime. Nevertheless when

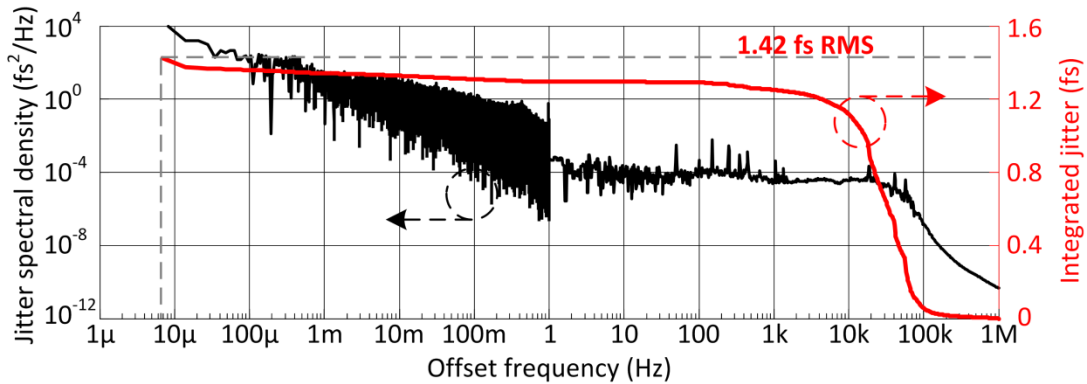


**Figure 5.22: Timing jitter spectrum of the laser network.**

Timing jitter spectral density measured by the out-of-loop detector (black curve) and its integrated timing jitter (red curve).

compared the results achieved with the Ti:sapphire laser shown in Figure 5.9, the laser network shows a substantial improvement from 8.55 fs to 1.3 fs ( $>1$  Hz) even though it includes an additional laser.

## 5.5 ATTOSECOND PRECISION LASER-MICROWAVE NETWORK

To achieve attosecond-precision timing-synchronization across both optical and microwave frequency domains, next experiments are performed in optical-to-microwave synchronization using BOMPDs [59,60]. Conventional microwave phase-locking techniques based on direct photodetection cannot realize long-term sub-fs precision due to sensitive operating conditions of zero AM-PM conversion in photodetectors and their limited RF phase discrimination. To circumvent these issues, we have developed free-space-coupled BOMPDs (FSC-BOMPD) based on Sagnac-interferometers as described in Section 2.3.1 which can efficiently reduce long-term drifts caused by the environment, and enable precise phase tuning without backlash, microwave reflection and loss. When compared with other optical-microwave phase detectors [59,60], FSC-BOMPD can provide a high SNR and an order of magnitude improvement in terms of long-term timing stability simultaneously which are essential to achieve attosecond precision in the laser-microwave network. In this section, FSC-BOMPD local synchronization results between the master laser and a low-noise VCO are presented first. Then, the FSC-BOMPDs are incorporated into our timing distribution system to demonstrate the first laser-microwave network breaking the femtosecond barrier in terms of timing precision.

### 5.5.1 LOCAL LASER-MICROWAVE SYNCHRONIZATION

The experimental setup for local laser-microwave synchronization is shown in Figure 5.23. A sapphire-loaded crystal oscillator (Raytheon; SLCO-10.833-NCS) serves as the tunable microwave source (i.e., VCO). It operates at 10.833-GHz center frequency, which is an integer multiple ( $=50 f_R$ ) of the master laser repetition rate. A low-phase-noise amplifier after the VCO is used to maximize the phase discriminant of the FSC-BOMPD. The output of the master laser is separated into the SGI, bias and reference paths with free space optics. Photodetected pulse train in the bias path is filtered at the 59th harmonic of the repetition rate, frequency-divided to 6.377 GHz ( $=29.5 f_R$ ), and adjusted in amplitude and phase to achieve quadrature bias condition given by Equation (2.11). Using similar detection electronics, the reference signal is generated at 108.33 MHz ( $=0.5 f_R$ ). When the microwave signal is applied to SGI, any phase error between the input signals will induce amplitude modulation in the pulse train at the SGI output. The error modulation sidebands of the pulse train are directly detected, filtered at 108.33 MHz and down-converted in-phase with the reference signal to generate the output phase error signal at baseband. The detected phase error is fed back to the frequency tuning port of the VCO via a PI controller to lock the microwave frequency to the repetition rate of the master laser. The timing precision of the local synchronization is determined

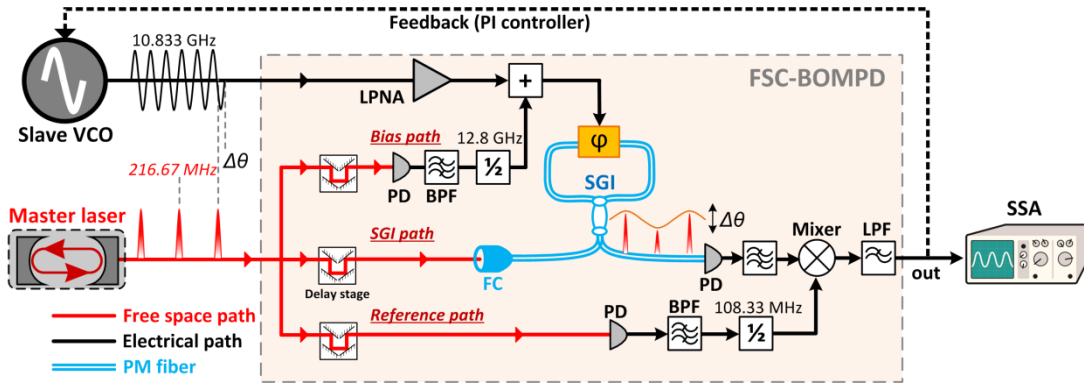


**Figure 5.23: Experimental setup for local laser-microwave synchronization.**

VCO: Voltage-controlled oscillator;  $\Delta\theta$ : phase error between the master laser and the VCO; LPNA: low-phase-noise electronic amplifier; PD: photodetector; BPF: bandpass filter;  $\frac{1}{2}$ : frequency divider; +: microwave diplexer; LPF: lowpass filter;  $\phi$ : phase modulator; SGI: Sagnac-interferometer; FC: fiber collimator; SSA: signal source analyzer.

with a signal source analyzer which measures the electronic spectrum of the FSC-BOMPD output. Figure 5.24 compares the local synchronization results (gray curve) with the free-running timing jitter of the master laser (red curve, taken from Figure 3.4(b)) and the slave VCO (black curve, provided by the manufacturer). The FSC-BOMPD lock has a residual in-loop jitter of only 0.46 fs RMS between the master laser and slave VCO integrated from 100 Hz to 1 MHz and the SSB phase noise of the local synchronization remains lower than -145 dBc/Hz (scaled at 10-GHz carrier) except for several sharp spikes. Another striking result is that the sapphire-loaded VCO surpasses

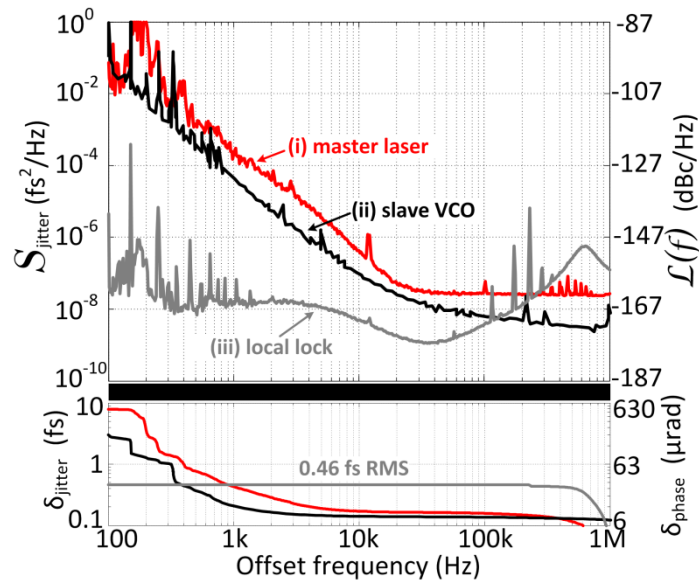


**Figure 5.24: Experimental results of the local laser-microwave synchronization.**

Left axes: timing jitter spectral density  $S_{\text{jitter}}$  and its integrated jitter  $\delta_{\text{jitter}}$  for different feedback gains; right axes: equivalent SSB phase noise  $\mathcal{L}(f)$  and its integrated phase error  $\delta_{\text{phase}}$  scaled to 10-GHz carrier frequency. Free-running jitter of (i) the master laser and (ii) the slave VCO. (iii) Residual in-loop jitter of the laser-microwave synchronization.  $\delta_{\text{jitter}}$  and  $\delta_{\text{phase}}$  are shown in logarithmic scale.



The link power is adjusted to minimize the nonlinearity-induced jitter (see Figure 4.12(b)) as well as to maximize the SNR for BOC locking. The time of flight fluctuations of the timing links are detected by PNS-BOCs whose error outputs are fed back to the fiber stretchers and the motorized delays to compensate fast timing jitter and slow timing drift of the fluctuating link delays. To eliminate power-fluctuation-induced drift (see Figure 4.11), a third feedback signal is sent to the EDFA to control its pump current as shown in Figure 4.15(c).

The link outputs are used for the synchronization of a remote laser (e.g., serving as the seed oscillator of a pump laser at the FEL end station) and a remote VCO (e.g., serving as a microwave reference of the FEL Linacs) simultaneously. The slave laser is identical to the master laser, whereas the slave VCO is a sapphire-loaded crystal oscillator whose noise characteristics are presented in the previous section. A PNS-BOC is built to synchronize the slave laser to timing link 1 output, whereas the slave VCO is locked to timing link 2 output with a FSC-BOMPD (i.e., FSC-BOMPD1 in Figure 5.25). Finally, the performance of the complete laser-microwave network is evaluated with an out-of-loop FSC-BOMPD measuring the relative timing jitter between the slave laser and the slave VCO.

In the phase-sensitive parts of the FSC-BOMPDs (e.g., electronic amplifiers in the bias and reference paths), a voltage change of only several microvolts can cause a timing error of 1 fs. Therefore, all digital circuits are galvanically isolated from the FSC-BOMPDs, while the analog power lines are connected in a single point configuration through electromagnetic interference filters to prevent electrostatic discharge and to eliminate undesirable ground loops and noise pick-ups. Thus, robust operation of the FSC-BOMPD has been ensured without dropping out of lock during several days of operation.

Figure 5.26(a)–(e) show the measured timing response curves of all timing detectors used in the experiment. In general, the timing sensitivities of the detectors are scaled with their input power provided by the oscillators to be synchronized. Laser-locking PNS-BOC3 has the largest timing sensitivity with 7.9 mV/fs (see Figure 5.26(c)) among all detectors due to the high power available from the slave laser ( $\sim 13$  dBm). In the case of link-locking PNS-BOC1 and PNS-BOC2, the average power in their reference arms is around 10 dBm. However, the average powers provided by their roundtrip-traveled link pulses differ by  $\sim 2$  dB because the overall attenuation of the 3.5-km link is  $\sim 7$  dB, whereas the attenuation of the 1.2-km link is  $\sim 5$  dB. Therefore, the timing sensitivity of PNS-BOC2 (2 mV/fs, Figure 5.26(b)) is slightly higher than the one of PNS-BOC1 (1 mV/fs, Figure 5.26(a)).

In the case of FSC-BOMPD1 locking the slave VCO to the timing link 2, the link output power is limited to +10 dBm to minimize fiber nonlinearities in the reverse link propagation. Therefore, the bias and reference arms of the FSC-BOMPD1 receive 0 dBm each while the SGI receives +5 dBm

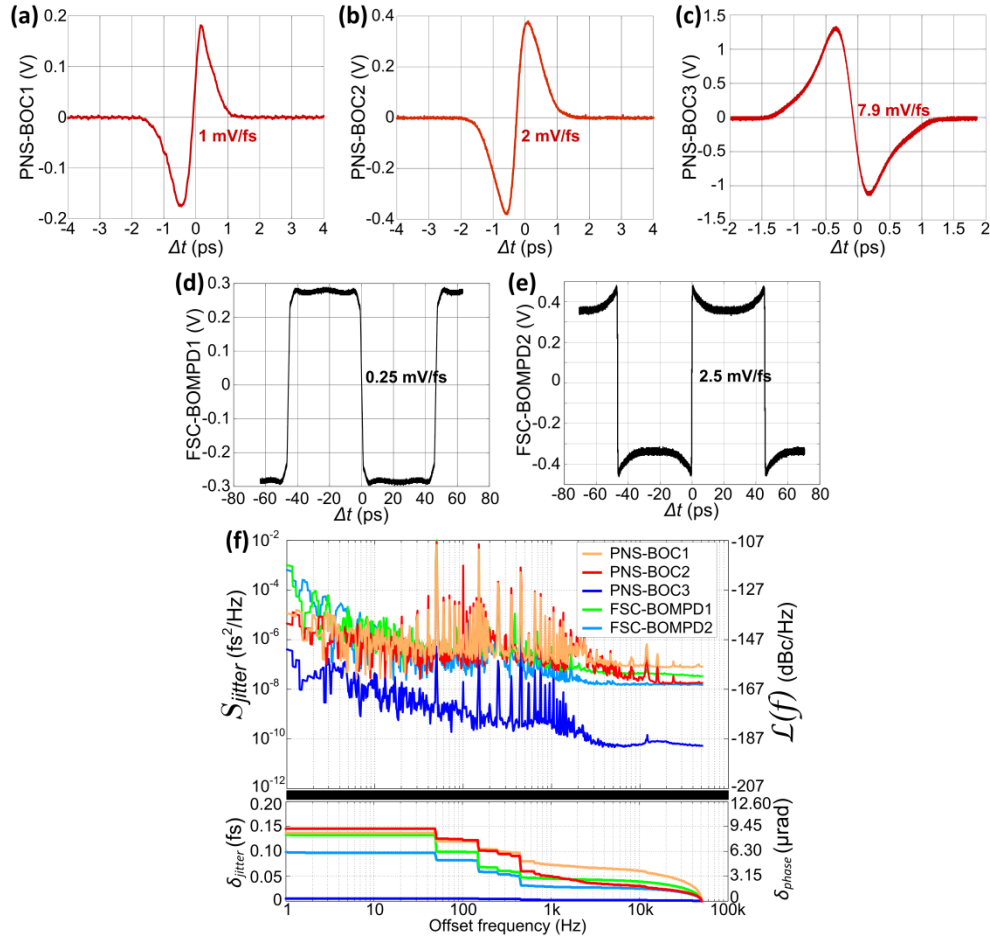


**Figure 5.26: Timing sensitivities and noise floors of the detectors.**

Voltage responses of (a) PNS-BOC1, (b) PNS-BOC2, (c) PNS-BOC3, (d) FSC-BOMPD1, (e) out-of-loop FSC-BOMPD2.  $\Delta t$ : time delay between the input signals. (f) Detector noise-floors; Left axes: timing jitter spectral density  $S_{\text{jitter}}$  and its integrated jitter  $\delta_{\text{jitter}}$  for different feedback gains; right axes: equivalent SSB phase noise  $\mathcal{L}(f)$  and its integrated phase error  $\delta_{\text{phase}}$  scaled to 10-GHz carrier frequency.

after the fiber collimator loss. Due to the free-space optics in the remote laser part, there is no nonlinearity onset and a total optical power of +14 dBm is provided for the out-of-loop FSC-BOMPD2, where the bias and reference paths receive 0 dBm each and the SGI obtains +10 dBm after fiber coupling loss. The microwave input power for each FSC-BOMPD is about +21 dBm. With this signal configuration, the FSC-BOMPD1 has a timing sensitivity of 0.25 mV/fs (Figure 5.26(d)), whereas the out-of-loop detector FSC-BOMPD2 has 2.5 mV/fs (Figure 5.26(e)).

Figure 5.26(f) shows the measured detector noise floors and their integrated timing jitter. Thanks to its high timing sensitivity, PNS-BOC3 exhibits a timing noise floor of only 5 as RMS integrated from 50 kHz down to 1 Hz. Even though the timing sensitivities of the other detectors are relatively lower when compared to PNS-BOC3, they all possess noise floors better than -145 dBc/Hz for [1 kHz – 50 kHz]. Furthermore, their integrated timing noise floors are lower than 0.15 fs RMS for the complete offset frequency range, which can support tight locking with attosecond precision.

When the in-loop detectors (PNS-BOC1-3 and FSC-BOMPD1 symbolized with “closed lock symbols” in Figure 5.25) and their feedback loops are activated, synchronous operation of the laser-microwave network is ensured and the timing precision of the system is monitored with the free-running FSC-BOMPD2. This experiment is of great significance, because it directly measures the relative timing jitter between a remotely synchronized mode-locked laser and a microwave source which has never been shown before. The synchronous laser-microwave network shows an unprecedented long-term precision of 670 as RMS over 18 h as shown in Figure 5.27(a). Compared with previous mode-locked laser based timing transfer results [33], this setup includes ten-times longer fiber links and additional remote laser synchronization system, yet it still achieves more than an order-of-magnitude improvement.

The FSC-BOMPDs have no active temperature control system; however, they are placed within a thermally insulated enclosure to damp temperature and humidity changes of the environment.

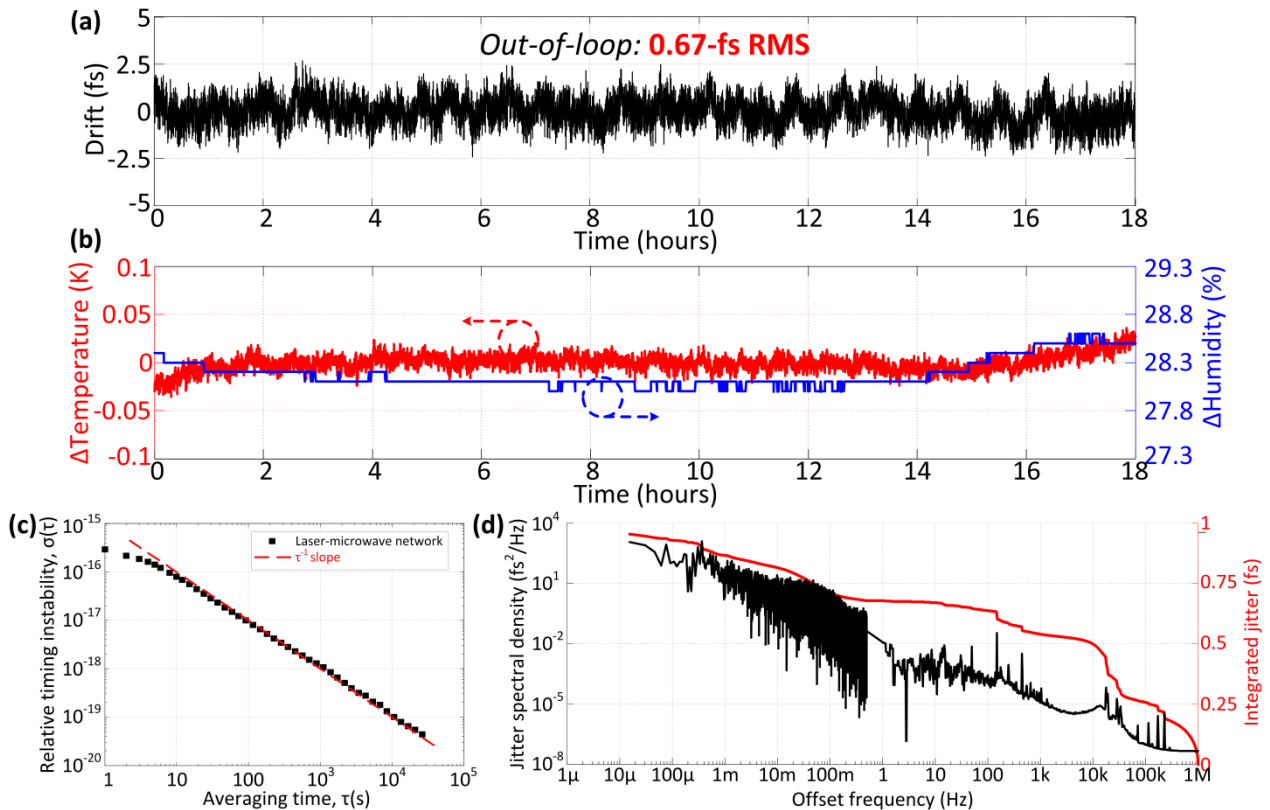


**Figure 5.27: Experimental results of the synchronous laser-microwave network.**

(a) Long-term timing drift below 1 Hz measured by the free-running FSC-BOMPD2 (sampling rate = 2 Hz). (b) Environmental temperature ( $\Delta$ Temperature, red curve) and humidity change ( $\Delta$ Humidity, blue curve) of the FSC-BOMPDs during the timing drift measurement. (c) Relative timing instability of the network in terms of overlapping Allan deviation. (d) Timing jitter spectral density (black curve) and its integrated timing jitter (red curve) for the complete range of measurements.

After a necessary warm-up time of several hours, the FSC-BOMPDs experience a temperature stability of 0.08 K and a relative humidity fluctuation of 0.6% during the measurement period as shown in Figure 5.27(b).

The relative timing instability of the laser-microwave network is  $2.9 \times 10^{-16}$  at 1-s averaging time ( $\tau$ ) and decreases to  $4.3 \times 10^{-20}$  after 26 000 s following a slope very close  $\tau^{-1}$  (see Figure 5.27(c)). The integrated timing jitter between the two remotely synchronized devices within the full frequency range from 15  $\mu$ Hz to 1 MHz is only 950 as RMS (Figure 5.27(d), red curve). To the best of our knowledge, this is the first demonstration of remote optical-to-microwave synchronization delivering attosecond-precision, as well as the first demonstration of a synchronous laser-microwave network.

Based on the feedback model presented in Sections 4.3.4 and 5.4.2 (see Equations (4.41) and (5.25)), the out-of-loop timing jitter contains the environmental noise imposed on the timing links, the link-induced jitter, the electronic noise of the system, and the inherent jitter of the master laser and slave oscillators. In our system, most of the environmental noise below 1 kHz is well suppressed by the feedback loop. The link-induced jitter is also minimized by choosing the minimum link operating power required for tight link/laser/microwave locking. Therefore, the excess timing jitter accumulated above 1 kHz in Figure 5.27(d) is mainly attributed to the uncompensated inherent jitter of the master and slave oscillators which may even be amplified at the resonant frequencies of the feedback loops if not paid attention. Lastly, the residual drift of the laser-microwave network below 100 mHz is limited by the length fluctuations of the conventional coaxial cables in the RF paths of the FSC-BOMPDs which can be improved by reducing the electronics into an integrated board or using special phase-stable cables with a much lower thermal-expansion ratio.

## 6 CONCLUSION AND OUTLOOK

This work demonstrates the first timing distribution system that is able to synchronize distant mode-locked lasers and microwave oscillators with attosecond precision for an extended period of time (i.e., from 1  $\mu$ s up to >18 h). Prior to this thesis, the highest timing precision was provided by the pulsed-optical timing distribution system which is demonstrated by our former group members [30,55] and implemented in operational FELs such as FLASH [44] and FERMI [104]. This scheme had breached the 100-fs barrier set by the conventional microwave distribution [31,54] and achieved a timing precision of  $\sim$ 10 fs for several hundred meters of fiber links. The pulsed-optical approach is further pursued within this thesis and attosecond timing precision is realized by thoroughly investigating and eliminating the remaining noise sources in the system.

First of all, optical and microwave timing detection schemes are further developed to support long-term attosecond precision. Type II second-harmonic BOC operating at 1550 nm is the most widely used timing detector in the system stabilizing the transmission delays of the fiber based timing links. It is found that this BOC scheme is prone to finite polarization extinction ratios of the input pulses projecting some portion of the optical power along the undesired polarization axes of the nonlinear crystal. These projected pulses cause a background noise and make it impossible to lock the system at the zero crossing, i.e., zero AM-to-PM conversion point. This noise source is completely removed by placing a highly birefringent material before the nonlinear crystal. To avoid the disadvantages of direct photodetection, BOMPDs are employed as optical-to-microwave timing detectors of the system which convert the phase error between an optical pulse train and a microwave into an intensity modulation of the optical signal. To improve the long-term stability of the BOMPD, free-space optical components are used for the optical beam distribution to the bias, reference and signal paths. Furthermore, the phase modulator in the SGI is biased with a high microwave frequency (6.377 GHz) to ensure a unidirectional operation and the down-mixing of the detected SGI output is performed at the lowest frequency possible (108.33 MHz) to maximize SNR at photodetection and to minimize thermally induced phase changes in the reference path.

Being the heart of the timing distribution system, low-noise operation of the master laser holds a great importance to achieve the desired precision. Noise characterization of the chosen mode-locked laser shows a free-running timing jitter of only  $\sim$ 0.17 fs RMS above 10-kHz offset frequency proving its viability as the master oscillator to support a kilometer-scale timing network with attosecond precision. Long-term frequency stability is ensured by locking the laser repetition rate to a microwave oscillator with low locking bandwidth around 100 Hz and by building an optical enclosure which provides an environmental stability of <0.1 K temperature variation and <1%

relative humidity change. With these improvements, the repetition rate stability of the master laser is measured to be  $\sim 15$  Hz at the 6<sup>th</sup> harmonic (1.3 GHz) for 5 consecutive days.

Timing-stabilized fiber links constitute the backbone network of the synchronization system serving the timing signal of the master laser to distant slave oscillators without adding excess noise. When the motorized delays are actuated to compensate for long-range delay fluctuations in the timing links, they introduce inevitable beam misalignments causing the link output to fluctuate. Since the pulses propagate in a nonlinear medium such as the optical fiber, these power fluctuations induce temporal shifts in the COG of the traveling pulses which is a combined effect of residual link dispersion and nonlinearities (see Equation (4.35)). Such temporal profile distortions shift the zero-crossing time of the BOC which causes timing errors in the order of few femtoseconds if the COG shifts accumulated during forward- and backward-propagation in the link are not equal to each other. The experiments verify that COG-dependent timing fluctuations determine the long-term precision of the system and prohibit sub-fs operation if not taken care of. This noise source is removed from the timing distribution system by activating a third feedback control on the pump current of the EDFA to stabilize the link power fluctuations. Furthermore, the theoretical analysis shows that residual link dispersion and nonlinearities add considerable excess jitter through the link transmission and feedback loops even in the absence of environmental noise and determine the high frequency jitter limit for the whole system. Therefore, residual second- and third-order dispersion of the links is carefully compensated with additional dispersion-compensating fiber to suppress the link-induced Gordon-Haus jitter and to minimize the output pulse durations for high SNR in the BOCs. The link power is adjusted to minimize the nonlinearity-induced jitter as well as to maximize the SNR for BOC locking. With these key developments in the link stabilization, a fiber link network with 4.7-km length is realized with a total timing jitter of 580 as RMS measured from 1  $\mu$ s to 52 h.

Several experiments are performed for the remote synchronization of slave mode-locked lasers via the timing stabilized fiber links. The results show that the main contribution to the integrated timing jitter originates from the noise above 10-kHz offset frequency. In order to investigate the high frequency noise sources of the timing distribution system, a novel jitter analysis method is developed that is based on feedback flow between the setup elements. The feedback loop analysis yields an excellent agreement with the experimental results and identifies the noise sources in the system with their estimated timing jitter contributions. Furthermore, it points out that it is imperative to pay considerable attention to the low noise properties of the slave lasers since they may limit the high-frequency performance of the complete system. This analysis method will prove invaluable in large-scale scientific facilities where synchronization of many lasers over large

distances is required. Moreover, it can easily be extended to cover different synchronization experiments and is extremely useful in not only identifying sources of timing jitter but also in understanding how they depend on the parameters of the network (e.g., feedback gain of the various stabilization loops). With help of the feedback model, a synchronous mode-locked laser network is realized and its high-frequency precision is improved from 8.55 fs RMS down 1.3 fs RMS which is limited by the unsuppressed jitter of the slave lasers beyond the locking bandwidth. By bringing all the knowledge and experience accumulated throughout the thesis, a synchronous laser-microwave network is demonstrated which overcomes the femtosecond barrier in multi-kilometer timing synchronization systems and provides a precision in the attosecond regime from 1  $\mu$ s to 18 h.

The demonstrated system has the potential of enabling new generation hard X-ray photon science facilities such as X-ray FELs and laser-based attoscience centers that demand the most challenging synchronization requirements to generate ultrashort X-ray pulses for the benefit of creating super microscopes with subatomic spatiotemporal resolution. In turn, this may drive new scientific endeavors towards the much-coveted realization of molecular movies on attosecond time scales, thereby opening up many new research areas in biology, chemistry, fundamental physics and material science. Besides, the demonstrated system can also be implemented in other ambitious large-scale scientific explorations, such as comparison of distant optical clocks [15], sensitive imaging of low temperature black bodies using multi telescope arrays [24], gravitational deflection measurements of radio waves using very-long-baseline interferometers [25], and synchronization of synchrotron light sources [105].

Figure 6.1(a) shows the integrated timing jitter of the various experiments presented in the thesis within the locking bandwidths of all feedback loops (i.e., below 1 kHz). While all the systems operate with attosecond timing over days of measurement, there is an apparent inverse correlation between the physical size of the system and the long-term precision. Remote-laser synchronization system involving only one slave laser and one timing-stabilized fiber link has the lowest timing jitter measured with  $\sim 200$  as RMS, whereas the most sophisticated system synchronizing a slave laser and a slave VCO over two timing stabilized fiber links exhibit  $\sim 800$  as RMS. The photo in Figure 6.1(b) shows the remote side of the laser-microwave network setup given in Figure 5.25 where the synchronization of the slave laser and the slave VCO is performed. Even though the environmental isolation of the BOMPDs is highly improved with the free-space optics, bulky microwave electronics and their power management (see FSC-BOMPDs in Figure 6.1(b)) still create long-term timing fluctuations for the laser-microwave network as can be observed from the red curve below 100 mHz in Figure 6.1(a). Therefore, the next step will be to reduce the complete electronics of the BOMPD into a single integrated board by preserving their high phase sensitivity.

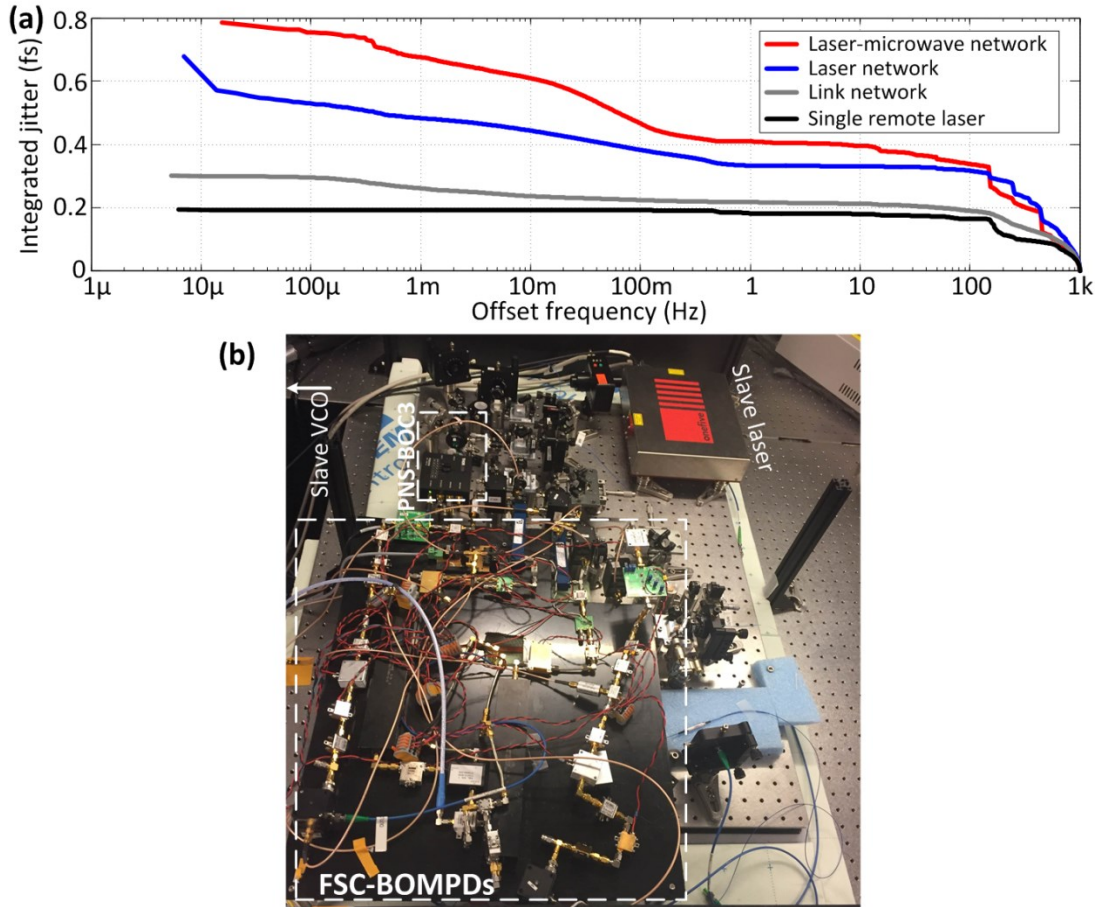


**Figure 6.1: Timing jitter within the locking bandwidth.**

(a) Integrated timing jitters of the various experiments presented in the thesis. (b) The photo of the remote side of the experimental setup in Figure 5.25 where the synchronization of the slave laser and slave VCO is performed.

To shrink the volume of optics and decrease the power budget of the fiber links, FC-BOCs with integrated PPKTP waveguides are developed and implemented into the timing distribution system. Current efficiency of the FC-BOCs is limited by the excess second-harmonic coupling loss but still delivers a sensitivity comparable to the bulk-optic BOCs. The next generation device will include an integrated WDM to eliminate the coupling problem, thereby increasing the performance by an order of magnitude and providing an easy-to-implement and alignment-free solution to the fiber link stabilization problem.

Figure 6.2 shows the integrated timing jitter values above 1 kHz which are mainly dominated by the uncompensated noise sources beyond the locking bandwidths of the feedback loops. The excess timing jitter observed in the mode-locked laser network (blue curve) emphasizes one more time that the oscillators employed in timing or frequency transfer applications must have lower noise than the targeted precision of the system. Therefore, development of stable mode-locked lasers and

microwave oscillators will relieve the high frequency jitter requirements of the timing distribution systems.

The final systems to be synchronized with X-ray FELs and attoscience facilities will be laser amplifier chains with millijoule-level pulse energy and kilohertz-level repetition rate. The experimental methods and results demonstrated in this thesis offer a proven way to synchronize the seed oscillators of such laser systems with unprecedented precision. Therefore, the next task here will be to integrate these laser systems together with the developed timing tools and develop a complete facility synchronization without degrading the low-noise properties of the seed laser pulses along their way with numerous regenerative and multi-pass amplifiers.

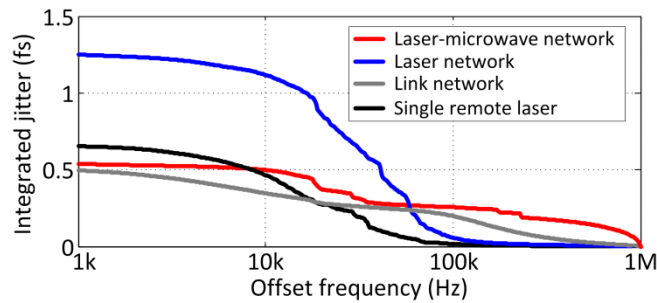


**Figure 6.2: Timing jitter above 1 kHz.**

Integrated timing jitters above 1 kHz of the various experiments presented in the thesis.

## A APPENDIX

### A.1 TOTAL TRANSFER FUNCTION AND ELECTRONIC NOISE JITTER

In the feedback models developed in the thesis, each BOC lock has two electronic noise sources  $E_{BOC}$  and  $E_{PI}$  (in units of  $V/\sqrt{\text{Hz}}$ ) and four transfer functions  $H_{BOC}$ ,  $H_{BPD}$ ,  $H_{PI}$  and  $H_{PZT}$ .  $H_{BOC}$  is simply the timing sensitivity of the BOC converting the timing error to a voltage error signal. This error voltage is amplified by the transimpedance amplifier of the BPD with its 3-dB bandwidth (i.e.,  $H_{BPD}$ ) and processed by the PI controller (i.e.,  $H_{PI}$ ). Finally, the PI output is applied to the PZT actuator with a resonance frequency at  $f_{res}$  and a transfer function  $H_{PZT}$ , which converts it to a corrective time delay and closes the feedback-loop. To simplify the mathematical derivation of the jitter sources, we define a total transfer function,  $H$  and an electronic jitter term,  $J_N$  for each BOC lock:

$$H = H_{BOC}H_{BPD}H_{PI}H_{PZT} \quad (\text{A.1})$$

$$J_N = -\frac{E_{BOC}}{H_{BOC}} + \frac{E_{PI}}{H_{BOC}H_{BPD}H_{PI}} \quad (\text{A.2})$$

As can be inferred from Equation (A.2),  $J_N$  refers to the timing jitter (in units of  $s/\sqrt{\text{Hz}}$ ) generated by the electronic noise sources (i.e.,  $E_{BOC}$  and  $E_{PI}$ ) and transferred to the input of the BOC by the feedback loop. Therefore,  $E_{BOC}$  is divided by  $H_{BOC}$  and  $E_{PI}$  is divided by  $H_{BOC}H_{BPD}H_{PI}$ . Finally, the following transfer functions for our experimental devices are used in calculation of  $H$ :

$$H_{BOC} = k_{BOC} \quad (\text{A.3})$$

$$H_{PI} = k_{PI} \left( \frac{s + 2\pi f_{PI}}{s} \right) \quad (\text{A.4})$$

$$H_{BPD} = \left( 1 + \frac{s}{2\pi f_{BW}} \right)^{-1} \quad (\text{A.5})$$

$$H_{PZT} = \frac{k_{PZT}}{s f_R} \left( \frac{(2\pi f_{res})^2}{s^2 + \zeta s + (2\pi f_{res})^2} \right) \quad (\text{A.6})$$

where  $s=j\omega$  is the complex frequency,  $k_{BOC}$  is the timing sensitivity of the BOC,  $k_{PI}$  and  $f_{PI}$  are the gain and corner frequency of the PI controller. Furthermore,  $f_{BW}$  is the 3-dB bandwidth of the BPD,  $k_{PZT}$  is the slave laser's PZT sensitivity,  $f_R$  is the repetition rate of the slave laser,  $f_{res}$  is the slave laser's PZT resonance and  $\zeta$  is the PZT response parameter. Please note that these individual transfer functions are complex functions acting as commutative linear operators in the frequency domain. For the PZT transfer functions of the fiber stretchers in the timing links, we use voltage-response data provided by the manufacturer.

Next, the electronic noise of the BOC and the PI controller must be determined to calculate  $J_N$ . The electronic noise of a BOC is measured (in units of  $V/\sqrt{\text{Hz}}$ ) when there is no input light on the device,

and then converted to timing jitter ( $s/\sqrt{\text{Hz}}$ ) by multiplying with the timing sensitivity. The shot noise limit of a BOC is obtained when the BOC-based feedback loop is engaged. In this case, the photocurrent detected by each photodetector is measured from the individual ports of the BPD. The corresponding shot noise is calculated from the measured photocurrent in 1-Hz bandwidth ( $A/\sqrt{\text{Hz}}$ ). Then, the shot noise floor is converted to voltage noise ( $V/\sqrt{\text{Hz}}$ ) by the transimpedance gain of the BPD and finally to timing jitter ( $s/\sqrt{\text{Hz}}$ ) by multiplying with the timing sensitivity. The larger noise among these two contributions is used as  $E_{BOC}$  in the calculation. Finally, the electronic noise of the PI controller  $E_{PI}$  is estimated by using a noise model based on an integrating-operational-amplifier as shown in Figure A.1:

$$E_{PI}^2 = \frac{Z_f^2 4k_B T}{R_{in}} + 4k_B T R_f + \left(1 + \frac{Z_f}{R_{in}}\right)^2 V_n^2 \quad (\text{A.7})$$

together with the transimpedance gain of the operational-amplifier:

$$Z_f = \frac{1/R_f + sC}{1/R_f - s^2 C^2} \quad (\text{A.8})$$

where  $k_B$  is the Boltzmann constant, and  $T$  is the resistor's absolute temperature.

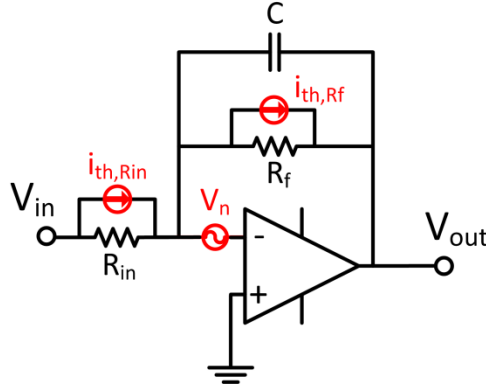


**Figure A.1: Noise model of a PI controller.**

$V_{in}$  and  $V_{out}$ : input and output voltage;  $V_n$ : input voltage noise of the PI controller;  $R_{in}$  and  $i_{th,Rin}$ : input impedance and its thermal noise current;  $R_f$  and  $i_{th,Rf}$ : feedback gain resistance and its thermal noise current;  $C$ : integrating capacitance.

## A.2 EXPERIMENTAL PARAMETERS USED IN THE CALCULATIONS

**Table A.1: Experimental parameters used for the feedback model in Figure 3.2.**

Symbol	Parameter	Value	Unit
$k_{SH-BOC}$	SH-BOC timing sensitivity	0.3	mV/fs
$k_{PI,SH-BOC}$	PI gain of the SH-BOC lock	<i>varied</i>	-
$f_{PI,SH-BOC}$	PI corner freq. of the SH-BOC lock	<i>varied</i>	-
$f_{BW,SH-BOC}$	BPD bandwidth of the SH-BOC lock	1	MHz
$k_{PZT}$	PZT sensitivity of the slave laser	17.4	Hz/V
$f_{res}$	PZT resonance of the slave laser	30	kHz
$\zeta$	PZT resonance parameter	$2 \times 10^5$	-
$f_R$	Repetition rate of the slave laser	216.67	MHz

**Table A.2: Experimental parameters used for the feedback model in Figure 4.13.**

Symbol	Parameter	Value	Unit
$k_{BOC}$	Timing sensitivity of the link-locking BOC	1	mV/fs
$k_{PI,BOC}$	PI gain of the BOC lock	<i>varied</i>	-
$f_{PI,BOC}$	PI corner freq. of the BOC lock	10	kHz
$f_{BW,BOC}$	BPD bandwidth of the BOC lock	100	MHz
$\tau_L$	One-way time delay of the 3.5-km link	17.2	$\mu$ s

**Table A.3: Experimental parameters used for the calculations in Figure 5.7.**

Symbol	Parameter	Value	Unit
$k_{SF-BOC}$	SF-BOC timing sensitivity	1.96	mV/fs
$k_{PI,SF-BOC}$	PI gain of the SF-BOC lock	<i>varied</i>	-
$f_{PI,SF-BOC}$	PI corner freq. of the SF-BOC lock	10	kHz
$f_{BW,SF-BOC}$	BPD bandwidth of the SF-BOC lock	45	MHz
$k_{PZT,Ti:sa}$	PZT sensitivity of the Ti:sa laser	70.3	Hz/V
$f_{res,Ti:sa}$	PZT resonance of the Ti:sa laser	23	kHz
$\zeta_{Ti:sa}$	PZT resonance parameter of the Ti:sa laser	$3 \times 10^5$	-
$f_{R,Ti:sa}$	Repetition rate of the Ti:sa laser	1.083	GHz
$R_{in}$	Input resistance of the PI controller	1	M $\Omega$
$R_f$	Gain resistance of the PI controller	$k_{PI} \times R_{in}$	$\Omega$
$C$	Integrating capacitance of the PI controller	10	nF
$V_n$	Input voltage noise of the PI controller	$10^{-9}$	V/Hz <sup>1/2</sup>

**Table A.4: Experimental parameters used for the feedback model in Figure 5.10.**

Symbol	Parameter	Value	Unit
$k_{PNS-BOC1}$	PNS-BOC1 timing sensitivity	1	mV/fs
$k_{PNS-BOC2}$	PNS-BOC2 timing sensitivity	2	mV/fs
$k_{SF-BOC1}$	SF-BOC1 timing sensitivity	1	mV/fs
$k_{PI,PNS-BOC1}$	PI gain of the PNS-BOC1 lock	0	dB
$k_{PI,PNS-BOC2}$	PI gain of the PNS-BOC2 lock	0	dB
$k_{PI,SF-BOC1}$	PI gain of the SF-BOC1 lock	-2	dB
$f_{PI,PNS-BOC1}$	PI corner freq. of the PNS-BOC1 lock	3	kHz
$f_{PI,PNS-BOC2}$	PI corner freq. of the PNS-BOC2 lock	10	kHz
$f_{PI,SF-BOC1}$	PI corner freq. of the SF-BOC1 lock	3	kHz
$f_{BW,PNS-BOC1}$	BPD bandwidth of the PNS-BOC1 lock	100	MHz
$f_{BW,PNS-BOC2}$	BPD bandwidth of the PNS-BOC2 lock	100	MHz
$f_{BW,SF-BOC1}$	BPD bandwidth of the SF-BOC1 lock	0.1	MHz
$\tau_{L1}$	One-way time delay of timing link 1	17.2	$\mu$ s
$\tau_{L2}$	One-way time delay of timing link 2	5.8	$\mu$ s
$k_{PZT,Ti:sa}$	PZT sensitivity of the Ti:sa laser	70.3	Hz/V
$f_{res,Ti:sa}$	PZT resonance of the Ti:sa laser	23	kHz
$\zeta_{Ti:sa}$	PZT resonance parameter of the Ti:sa laser	$3 \times 10^5$	-
$f_{R,Ti:sa}$	Repetition rate of the Ti:sa laser	1.083	GHz
$R_{in}$	Input resistance of the PI controllers	1	M $\Omega$
$R_f$	Gain resistance of the PI controllers	$k_{PI} \times R_{in}$	$\Omega$
$C$	Integrating capacitance of the PI controllers	10	nF
$V_n$	Input voltage noise of the PI controllers	$10^{-9}$	V/Hz <sup>1/2</sup>

**Table A.5: Experimental parameters used for the feedback model in Figure 5.18.**

Symbol	Parameter	Value	Unit
$k_{PNS-BOC1}$	PNS-BOC1 timing sensitivity	0.93	mV/fs
$k_{PNS-BOC2}$	PNS-BOC2 timing sensitivity	1.41	mV/fs
$k_{PNS-BOC3}$	PNS-BOC3 timing sensitivity	5	mV/fs
$k_{SF-BOC1}$	SF-BOC1 timing sensitivity	10	mV/fs
$k_{SF-BOC2}$	SF-BOC2 timing sensitivity	14.95	mV/fs
$k_{PI,PNS-BOC1}$	PI gain of the PNS-BOC1 lock	0	dB
$k_{PI,PNS-BOC2}$	PI gain of the PNS-BOC2 lock	0	dB
$k_{PI,PNS-BOC3}$	PI gain of the PNS-BOC3 lock	15	dB
$k_{PI,SF-BOC1}$	PI gain of the SF-BOC1 lock	22	dB
$f_{PI,PNS-BOC1}$	PI corner freq. of the PNS-BOC1 lock	3	kHz
$f_{PI,PNS-BOC2}$	PI corner freq. of the PNS-BOC2 lock	10	kHz
$f_{PI,PNS-BOC3}$	PI corner freq. of the PNS-BOC3 lock	13	kHz
$f_{PI,SF-BOC1}$	PI corner freq. of the SF-BOC1 lock	1	kHz
$f_{BW,PNS-BOC1}$	BPD bandwidth of the PNS-BOC1 lock	100	MHz
$f_{BW,PNS-BOC2}$	BPD bandwidth of the PNS-BOC2 lock	100	MHz
$f_{BW,PNS-BOC3}$	BPD bandwidth of the PNS-BOC3 lock	4	MHz
$f_{BW,SF-BOC1}$	BPD bandwidth of the SF-BOC1 lock	4	MHz
$\tau_{L1}$	One-way time delay of timing link 1	17.2	$\mu$ s
$\tau_{L2}$	One-way time delay of timing link 2	5.8	$\mu$ s
$k_{PZT,S1}$	PZT sensitivity of slave laser 1	14.24	Hz/V
$k_{PZT,S2}$	PZT sensitivity of slave laser 2	1.2	Hz/V
$f_{res,S1}$	PZT resonance of slave laser 1	40	kHz
$f_{res,S2}$	PZT resonance of slave laser 2	50	kHz
$\zeta_{S1}$	PZT resonance parameter of slave laser 1	$10^6$	-
$\zeta_{S2}$	PZT resonance parameter of slave laser 2	$10^5$	-
$f_{R,S1}$	Repetition rate of slave laser 1	216.67	MHz
$f_{R,S2}$	Repetition rate of slave laser 2	54.17	MHz
$R_{in}$	Input resistance of the PI controllers	1	M $\Omega$
$R_f$	Gain resistance of the PI controllers	$k_{PI} \times R_{in}$	$\Omega$
$C$	Integrating capacitance of the PI controllers	10	nF
$V_n$	Input voltage noise of the PI controllers	$10^{-9}$	V/Hz <sup>1/2</sup>

## BIBLIOGRAPHY

- [1] National Academy of Sciences, Engineering, and Medicine. (2016) Evolution Resources. [Online]. <http://www.nas.edu/evolution/index.html>
- [2] C. Kidd and B. Y. Hayden, "The psychology and neuroscience of curiosity," *Neuron*, vol. 88, pp. 449-460, 2015.
- [3] P. Khanna. (2016) TED Ideas worth spreading. [Online]. <https://www.ted.com/talks>
- [4] T. W. Hänsch, "Nobel lecture: passion for precision," *Reviews of Modern Physics*, vol. 78, no. 4, pp. 1297-1309, 2006.
- [5] International Bureau of Weights and Measures. (2016) SI Base Units. [Online]. [http://www.bipm.org/en/si/base\\_units/](http://www.bipm.org/en/si/base_units/)
- [6] C. O. Weiss, "Frequency measurement chain to 30 THz using FIR Schottky diodes and a submillimeter backward wave oscillator," *Appl. Phys. B*, vol. 34, pp. 63-67, 1984.
- [7] H. Schnatz et al., "First phase-coherent frequency measurement of visible radiation," *Phys. Rev. Lett.*, vol. 76, no. 1, pp. 18-21, 1996.
- [8] M. Bellini and T. W. Hänsch, "Phase-locked white-light continuum pulses: toward a universal optical frequency-comb synthesizer," *Opt. Lett.*, vol. 25, no. 14, pp. 1049-1051, 2000.
- [9] D. J. Jones et al., "Carrier-envelope phase control of femtosecond mode-locked lasers and direct optical frequency synthesis," *Science*, vol. 288, no. 5466, pp. 635-639, 2000.
- [10] O. D. Mücke et al., "Self-referenced 200 MHz octave-spanning Ti:Sapphire laser with 50 attosecond carrier-envelope phase jitter," *Opt. Express*, vol. 13, no. 13, pp. 5163-5169, 2005.
- [11] T. Udem, R. Holzwarth, and T. W. Hänsch, "Optical frequency metrology," *Nature*, vol. 416, no. 6877, pp. 233-237, 2002.
- [12] S. T. Cundiff and J. Ye, "Colloquium: Femtosecond optical frequency combs," *Rev. Mod. Phys.*, vol. 75, no. 1, pp. 325-342, 2003.
- [13] S. A. Diddams et al., "An optical clock based on a single trapped  $199\text{ Hg}^+$  ion," *Science*, vol. 293, pp. 825-828, 2001.
- [14] N. Huntemann, C. Sanner, B. Lipphardt, C. Tamm, and E. Peik, "Single-ion atomic clock with  $3 \times 10^{-18}$  systematic uncertainty," *Phys. Rev. Lett.*, vol. 116, no. 063001, 2016.
- [15] C. Lisdat et al., "A clock network for geodesy and fundamental science," *Nat. Commun.*, vol. 7, no. 12443, 2016.
- [16] B. Altschul et al., "Quantum tests of the Einstein Equivalence Principle with the STE-QUEST space mission," *Advances in Space Research*, vol. 55, no. 1, pp. 501-524, 2015.
- [17] P. Delva and J. Lodewyck, "Atomic clocks: new prospects in metrology and geodesy," *Acta Futura*, vol. 7, pp. 67-78, 2013.
- [18] P. Kómár et al., "A quantum network of clocks," *Nat. Phys.*, vol. 10, pp. 582 - 587, 2014.
- [19] T. Kessler et al., "A sub-40-mHz-linewidth laser based on a silicon single-crystal optical cavity," *Nat. Photonics*, vol. 6, pp. 687-692, 2012.
- [20] T. M. Fortier et al., "Generation of ultrastable microwaves via optical frequency division," *Nat. Photonics*, vol. 5, pp. 425-429, 2011.
- [21] A. J. Benedick, J. G. Fujimoto, and F. X. Kärtner, "Optical flywheels with attosecond jitter," *Nat. Photonics*, vol. 6, pp. 97-100, 2012.
- [22] E. Portuondo-Campa, R. Paschotta, and S. Lecomte, "Sub-100 attosecond timing jitter from low-noise

- passively mode-locked solid-state laser at telecom wavelength," *Opt. Lett.*, vol. 38, no. 15, pp. 2650–2653, 2013.
- [23] H. Kim et al., "Sub-20-attosecond timing jitter mode-locked fiber lasers," *IEEE J. Sel. Top. Quantum Electron.*, vol. 20, no. 5, pp. 260-267, 2014.
- [24] A. Wootten and A. R. Thompson, "The Atacama large millimeter/submillimeter array," *Proceedings of the IEEE*, vol. 97, no. 8, pp. 1463-1471, 2009.
- [25] H. Schuha and D. Behrend, "VLBI: A fascinating technique for geodesy and astrometry," *Journal of Geodynamics*, vol. 61, pp. 68-80, 2012.
- [26] B. P. Abbott et al., "LIGO: the Laser Interferometer Gravitational-Wave Observatory," *Rep. Prog. Phys.*, vol. 72, no. 076901, pp. 1-25, 2009.
- [27] B. Willke et al., "The GEO 600 gravitational wave detector," *Class. Quantum Grav.*, vol. 19, no. 7, pp. 1377–1387, 2002.
- [28] J.-F. Cliche and B. Shillue, "Precision timing control for radioastronomy: maintaining femtosecond synchronization in the Atacama large millimeter array," *IEEE Control Systems*, vol. 26, no. 1, pp. 19-26, 2006.
- [29] I. Bartos et al., "The advanced LIGO timing system," *Class. Quantum Grav.*, vol. 27, no. 084025, pp. 1-9, 2010.
- [30] J. Kim, J. A. Cox, J. Chen, and F. X. Kärtner, "Drift-free femtosecond timing synchronization of remote optical and microwave sources," *Nature Photon.*, vol. 2, no. 12, pp. 733-736, 2008.
- [31] R. Wilcox, J. M. Byrd, L. Doolittle, G. Huang, and J. W. Staples, "Stable transmission of radio frequency signals on fiber links using interferometric delay sensing," *Opt. Lett.*, vol. 34, no. 20, pp. 3050-3052, 2009.
- [32] P. A. Williams, W. C. Swann, and N. R. Newbury, "High-stability transfer of an optical frequency over long fiber-optic links," *J. Opt. Soc. Am. B.*, vol. 25, no. 8, pp. 1284-1293, 2008.
- [33] K. Jung et al., "Frequency comb-based microwave transfer over fiber with  $7 \times 10^{-19}$  instability using fiber-loop optical-microwave phase detectors," *Opt. Lett.*, vol. 39, no. 6, pp. 1577-1580, 2014.
- [34] X. Chen et al., "Simultaneously precise frequency transfer and time synchronization using feed-forward compensation technique via 120 km fiber link," *Sci. Rep.*, vol. 5, no. 18343, pp. 1-7, 2015.
- [35] B. P. Abbott et al., "Observation of gravitational waves from a binary black hole merger," *Phys. Rev. Lett.*, vol. 116, no. 061102, pp. 1-16, 2016.
- [36] F. Calegari et al., "Ultrafast electron dynamics in phenylalanine initiated by attosecond pulses," *Science*, vol. 346, pp. 336-339, 2014.
- [37] S. P. Hau-Riege, "Photoelectron dynamics in X-ray free-electron-laser diffractive imaging of biological samples," *Phys. Rev. Lett.*, vol. 108, no. 238101, 2012.
- [38] M. Altarelli et al., "The European x-ray free-electron laser," *Technical Design Report*, vol. DESY 97, pp. 1-26, 2006.
- [39] E. Allaria et al., "Highly coherent and stable pulses from the FERMI seeded free-electron laser in the extreme ultraviolet," *Nat. Photonics*, vol. 6, pp. 699-704, 2012.
- [40] P. Emma et al., "First lasing and operation of an angstrom-wavelength free-electron laser," *Nat. Photonics*, vol. 4, pp. 641-647, 2010.
- [41] J. Stohr, "Linac coherent light source II (LCLS-II) conceptual design report," *SLAC*, vol. SLAC-R-978, 2011.
- [42] R. Ganter, "SwissFEL-conceptual design report," *Paul Scherrer Institute (PSI)*, vol. PSI--10-04, 2010.
- [43] G. Mourou and T. Tajima, "The extreme light infrastructure: optics' next horizon," *Optics & Photonics*

- News*, vol. 22, pp. 47-51, 2011.
- [44] S. Schulz et al., "Femtosecond all-optical synchronization of an X-ray free-electron laser," *Nat. Commun.*, vol. 6, no. 5938, 2015.
- [45] E. Prat and S. Reiche, "Simple method to generate terawatt-attosecond X-ray free-electron-laser pulses," *Phys. Rev. Lett.*, vol. 114, no. 244801, 2015.
- [46] J. D. Sadler et al., "Compression of X-ray free electron laser pulses to attosecond duration," *Sci. Rep.*, vol. 5, no. 16755, pp. 1-7, 2015.
- [47] T. Ishikawa et al., "A compact X-ray free-electron laser emitting in the sub-angstrom region," *Nat. Photonics*, vol. 6, no. 8, pp. 540-544, 2012.
- [48] I. Grguraš et al., "Ultrafast X-ray pulse characterization at free-electron lasers," *Nat. Photonics*, vol. 6, no. 12, pp. 852-857, 2012.
- [49] A. M. Kondratenko and E. L. Saldin, "Generation of coherent radiation by a relativistic electron beam in an undulator," *Particle Accelerators*, vol. 10, no. 3-4, pp. 207-216, 1980.
- [50] J. Andruszkow et al., "First observation of self-amplified spontaneous emission in a free-electron laser at 109 nm wavelength," *Phys. Rev. Lett.*, vol. 85, no. 18, pp. 3825-3829, 2000.
- [51] R. Bonifacio, L. D. Salvo, P. Pierini, N. Piovella, and C. Pellegrini, "Spectrum, temporal structure, and fluctuations in a high-gain free-electron laser starting from noise," *Phys. Rev. Lett.*, vol. 73, pp. 70-73, 1994.
- [52] M. Lewenstein, P. Balcou, M. Y. Ivanov, A. L'huillier, and P. B. Corkum, "Theory of high-harmonic generation by low-frequency laser fields," *Phys. Rev. A*, vol. 49, no. 3, pp. 2117-2132, 1994.
- [53] J. Amann et al., "Demonstration of self-seeding in a hard-X-ray free-electron laser," *Nat. Photonics*, vol. 6, no. 10, pp. 693-698, 2012.
- [54] J. M. Glowina et al., "Time-resolved pump-probe experiments at the LCLS," *Opt. Express*, vol. 18, pp. 17620-17630, 2010.
- [55] J. Kim et al., "Large scale timing distribution and RF-synchronization for FEL facilities," *Proceedings of FEL Conference*, vol. 339-342, 2004.
- [56] T. R. Schibli et al., "Attosecond active synchronization of passively mode-locked lasers by balanced cross correlation," *Opt. Lett.*, vol. 28, no. 11, pp. 947-949, 2003.
- [57] J. Kim et al., "Long-term femtosecond timing link stabilization using a single-crystal balanced cross correlator," *Opt. Lett.*, vol. 32, no. 9, pp. 1044-1046, 2007.
- [58] F. Löhler et al., "Electron bunch timing with femtosecond precision in a superconducting free-electron laser," *Phys. Rev. Lett.*, vol. 104, no. 144801, 2010.
- [59] J. Kim, F. X. Kärtner, and F. Ludwig, "Balanced optical-microwave phase detectors for optoelectronic phase-locked loops," *Opt. Lett.*, vol. 31, no. 24, pp. 3659-3661, 2006.
- [60] M. Y. Peng, A. Kalaydzhyan, and F. X. Kärtner, "Balanced optical-microwave phase detector for sub-femtosecond optical-RF synchronization," *Opt. Express*, vol. 22, pp. 27102-27111, 2014.
- [61] Extreme Light Infrastructure delivery consortium. (2016, July) ELI. [Online]. <https://eli-laser.eu/>
- [62] G. Mourou and T. Tajima, "More intense, shorter pulses," *Science*, vol. 331, pp. 41-42, 2011.
- [63] ELI-ALPS. (2016, July) ELI-ALPS Research Facilities. [Online]. [http://www.eli-hu.hu/?q=en/02\\_Parameters](http://www.eli-hu.hu/?q=en/02_Parameters)
- [64] P. B. Corkum and F. Krausz, "Attosecond science," *Nat. Phys.*, vol. 3, no. 6, pp. 381-387, 2007.
- [65] S. Ghimire et al., "Observation of high-order harmonic generation in a bulk crystal," *Nat. Phys.*, vol. 7, no. 2, pp. 138-141, 2011.

- [66] J. Hebling, K.-L. Yeh, M. C. Hoffmann, B. Bartal, and K. A. Nelson, "Generation of high-power terahertz pulses by tilted-pulse-front excitation and their application possibilities," *J. Opt. Soc. Am. B*, vol. 25, no. 7, 2008.
- [67] A. Baltuška et al., "Attosecond control of electronic processes by intense light fields," *Nature*, vol. 421, no. 6923, pp. 611-615, 2003.
- [68] G. A. Mourou, G. Sandner, W. Korn, and J. L. Collier, *ELI whitebook: science and technology with ultra-intense lasers*. Berlin, Germany: Thoss Media GmbH, 2011.
- [69] C. Manzoni et al., "Coherent pulse synthesis: towards sub-cycle optical waveforms," *Laser Photonics Rev.*, vol. 9, no. 2, pp. 129-171, 2015.
- [70] O. D. Mücke et al., "Toward waveform nonlinear optics using multimillijoule sub-cycle waveform synthesizers," *IEEE J. Sel. Top. Quantum Electron.*, vol. 21, no. 5, p. 8700712, 2015.
- [71] H. Fattahi et al., "Third-generation femtosecond technology," *Optica*, vol. 1, no. 1, pp. 45-63, 2014.
- [72] W. Zhang et al., "Amplitude to phase conversion of InGaAs pin photo-diodes for femtosecond lasers microwave signal generation," *Appl. Phys. B*, vol. 106, pp. 301-308, 2012.
- [73] J. M. Byrd et al., "Femtosecond synchronization of laser systems for the LCLS," *Proceedings of IPAC 2010*, 2010.
- [74] J. Kodet and I. Prochazka, "Note: Optical trigger device with sub-picosecond timing jitter and stability," *Rev. Sci. Instrum.*, vol. 83, no. 036101, 2012.
- [75] W. A. Ackermann et al., "Operation of a free-electron laser from the extreme ultraviolet to the water window," *Nat. Photonics*, vol. 1, no. 6, pp. 336-342, 2007.
- [76] C. Sydlo et al., "Development status of optical synchronization for the European xfel," *Proceedings of IBIC 2013*, 2013.
- [77] P. T. Callahan, K. Safak, P. Battle, T. Roberts, and F. X. Kärtner, "Fiber-coupled balanced optical cross-correlator using PPKTP waveguides," *Opt. Express*, vol. 22, pp. 9749-9758, 2014.
- [78] J. Kim, F. X. Kärtner, and M. H. Perrot, "Femtosecond synchronization of radio frequency signals with optical pulse trains," *Opt. Lett.*, vol. 29, no. 17, pp. 2076-2078, 2004.
- [79] J. Kim and F. X. Kärtner, "Attosecond-precision ultrafast photonics," *Laser & Photon. Rev.*, vol. 4, no. 3, pp. 432-456, 2010.
- [80] I. Coddington et al., "Coherent optical link over hundreds of metres and hundreds of terahertz with subfemtosecond timing jitter," *Nat. Photonics*, vol. 1, no. 5, pp. 283-287, 2007.
- [81] L. Grüner-Nielsen et al., "Polarization maintaining dispersion compensating fiber," in *The European Conference on Optical Communication (ECOC)*, Cannes, 2014, pp. 1-3.
- [82] D. Von der Linde, "Characterization of the noise in continuously operating mode-locked lasers," *Appl. Phys. B*, vol. 39, no. 4, pp. 201-217, 1986.
- [83] R. P. Scott, C. Langrock, and B. H. Kolner, "High-dynamic-range laser amplitude and phase noise measurement techniques," *IEEE J. Sel. Top. Quantum Electron.*, vol. 7, no. 4, pp. 641-655, 2001.
- [84] W. Sun et al., "Broadband noise limit in the photodetection of ultralow jitter optical pulses," *Phys. Rev. Lett.*, vol. 113, no. 203901, pp. 1-5, 2014.
- [85] J. Kim, J. Chen, J. Cox, and F. X. Kärtner, "Attosecond-resolution timing jitter characterization of free-running mode-locked lasers," *Opt. Lett.*, vol. 32, pp. 3519-3521, 2007.
- [86] R. Paschotta, "Noise of mode-locked lasers (Part I): numerical model," *Appl. Phys. B*, vol. 79, pp. 153-162, 2004.
- [87] M. Xin et al., "Breaking the femtosecond barrier in multi-km timing synchronization systems," *IEEE J. Sel. Top. Quantum Electron.*, vol. 23, no. 3, 2017.

- [88] J. B. Johnson, "The Schottky effect in low frequency circuits," *Physical Review*, vol. 26, pp. 71-85, 1925.
- [89] K. Şafak, M. Xin, P. T. Callahan, M. Y. Peng, and F. X. Kärtner, "All fiber-coupled, long-term stable timing distribution for free-electron lasers with few- femtosecond jitter," *Struct. Dyn.*, vol. 2, no. 041715, pp. 1-10, 2015.
- [90] K. Jung and J. Kim, "Characterization of timing jitter spectra in free-running mode-locked lasers with 340 dB dynamic range over 10 decades of Fourier frequency," *Opt. Lett.*, vol. 40, no. 3, pp. 316-319, 2015.
- [91] J. A. Cox, "Sub-femtosecond precision timing distribution, synchronization and coherent synthesis of ultrafast lasers," Massachusetts Institute of Technology, Cambridge, PhD Thesis 2012.
- [92] OFS a Furukawa Company. (2016, August) OFS: Optical Fiber Cable and Connectivity Solutions. [Online]. [www.ofsoptics.com](http://www.ofsoptics.com)
- [93] M. Y. Peng et al., "Long-term stable, sub-femtosecond timing distribution via a 1.2-km polarization-maintaining fiber link: approaching 10<sup>-21</sup> link stability," *Opt. Express*, vol. 21, no. 17, pp. 19982-19989, 2013.
- [94] W. Decking and T. Limberg, "European XFEL post-TDR description," European XFEL, Hamburg, Technical Report TN-2013-004- 01, 2013.
- [95] M. Y. Peng, "Sub-femtosecond optical timing distribution for next-generation light sources," Massachusetts Institute of Technology, Cambridge, PhD Thesis 2015.
- [96] J. C. Diels and W. Rudolph, *Ultrashort Laser Pulse Phenomena*. San Diego: Academic Press, 2006.
- [97] G. P. Agrawal, *Nonlinear Fiber Optics*. San Diego: Academic Press, 2012.
- [98] M. Xin et al., "Attosecond precision multi-km laser-microwave network," *Light Sci. Appl.*, vol. 6, no. e16187, 2017.
- [99] J. Hult, "A fourth-order Runge–Kutta in the interaction picture method for simulating," *J. Lightwave Technol.*, vol. 25, pp. 3770-3775, 2007.
- [100] J. P. Gordon and H. A. Haus, "Random walk of coherently amplified solitons in optical fiber transmission," *Opt. Lett.*, vol. 11, no. 10, pp. 665-667, 1986.
- [101] D. W. Allan, "Time and frequency (time-domain) characterization, estimation, and prediction of precision clocks and oscillators," *IEEE Trans. Ultrason. Ferroelectr. Freq. Control*, vol. 34, no. 6, 1987.
- [102] L. J. Chen, A. J. Benedick, J. R. Birge, M. Y. Sander, and F. X. Kärtner, "Octave-spanning, dual-output 2.166 GHz Ti:sapphire laser," *Opt. Express*, vol. 16, pp. 20699-20705, 2008.
- [103] K. Şafak et al., "Jitter analysis of timing-distribution and remote-laser synchronization systems," *Opt. Express*, vol. 24, no. 19, 2016.
- [104] M. Ferianis et al., "All optical femtosecond timing system for the FERMI@Elettra FEL," in *International Free Electron Laser Conference*, Shanghai, 2011, pp. 641-647.
- [105] D. H. Bilderback, P. Elleaume, and E. Weckert, "Review of third and next generation synchrotron light sources," *J. Phys. B: At. Mol. Opt. Phys.*, vol. 38, pp. S773-S797, 2005.